DEVELOPMENT OF A NEW SOLUTION FOR VISCOELASTIC WAVE PROPAGATION OF PAVEMENT STRUCTURES AND ITS USE IN DYNAMIC BACKCALCULATION

Ву

Hyung Suk Lee

A DISSERTATION

Submitted to
Michigan State University
in partial fulfillment of the requirements
for the degree of

Civil Engineering – Doctor of Philosophy

2013

ABSTRACT

DEVELOPMENT OF A NEW SOLUTION FOR VISCOELASTIC WAVE PROPAGATION OF PAVEMENT STRUCTURES AND ITS USE IN DYNAMIC BACKCALCULATION

By

Hyung Suk Lee

Due to the viscoelastic nature of asphalt materials and the dynamic nature of pavement structures, it is important to consider both effects simultaneously in modeling of asphalt pavements. In this study, a new computational algorithm, namely ViscoWave, has been developed and implemented for modeling the pavement dynamics and viscoelasticity under an impact load generated by a Falling Weight Deflectometer (FWD). The primary advantage of the proposed solution over some of the existing solutions is that it uses continuous integral transforms (Laplace and Hankel transforms) that are more appropriate for the FWD time histories whose signal characteristics are transient, nonperiodic, and truncated.

Prior to the mathematical formulation of the developed algorithm, the fundamental properties of a viscoelastic material and the theory of uniaxial viscoelasticity are reviewed. Then, the theory of linear, uniaxial viscoelasticity is extended to multi-axial viscoelasticity. The multi-axial theory of viscoelasticity is, in turn, applied to develop a methodology for analyzing the laboratory Indirect Tensile (IDT) test data.

The theoretical development of ViscoWave follows similar steps to those used for the development of the spectral element method. However, in place of the discrete transforms adopted in the spectral element method, ViscoWave utilizes the continuous integral transforms

(namely Laplace and Hankel transforms) that are more appropriate for transient, nonperiodic signals. The theory behind ViscoWave was verified by comparing the ViscoWave simulation results to other existing solutions such as the Finite Element Analysis (FEA) and spectral element method.

To backcalculate the pavement layer parameters, two of the well known unconstrained optimization algorithms (Gauss-Newton and Levenberg-Marquardt methods) were adopted for use with ViscoWave. The backcalculation was conducted using both theoretically-generated and field-obtained FWD time histories. The results indicate that ViscoWave has great potential for modeling the viscoelastic and dynamic effects of a pavement structure under an impact load.

To my beloved daughter Lena Dah-Ye Lee, my mother Ok Hee Seo, my father Doo Seon Lee, and my sister Seung Eun Lee

TABLE OF CONTENTS

LIST OF TABLES	vii
LIST OF FIGURES	viii
CHAPTER 1 - INTRODUCTION	1
1.1. General	1
1.2. Problem Statement	2
1.3. Research Objective	3
1.4. Report Layout	3
CHAPTER 2 - LITERATURE REVIEW	6
CHAPTER 3 - REVIEW OF UNIAXIAL THEORY OF LINEAR VISCOELASTIC	CITY 10
3.1. Fundamental Properties of a Viscoelastic Material in Time Domain	10
3.2. Fundamental Properties of a Viscoelastic Material in Frequency Domain	
3.3. Relationship between Viscoelastic Properties	13
3.4. Time-Temperature Superposition Principle	15
3.5. Analytical Models for Viscoelastic Properties	19
3.6. Prony Series	
3.7. Elastic-Viscoelastic Correspondence Principle	26
CHAPTER 4 - EXTENSION TO MULTI-AXIAL VISCOELASTICITY AND ANA	LYSIS
OF INDIRECT TENSILE TEST DATA	
4.1. Viscoelastic Poisson's Ratio	
4.1.1. Viscoelastic Poisson's Ratio in Time Domain	
4.1.2. Viscoelastic Poisson's Ratio in Frequency Domain	
4.1.3. Relationship Between Time and Frequency Dependent Poisson's Ratios	
4.2. Extension of the Elastic-Viscoelastic Correspondence Principle	
4.3. Determining the Viscoelastic Property from the Indirect Tensile (IDT) Test	
4.3.1. Stress Distribution within an Indirect Tensile (IDT) Specimen	
4.3.2. Indirect Tensile Creep Test	
4.3.3. Indirect Tensile Complex Modulus Test	43
CHAPTER 5 - THEORETICAL DEVELOPMENT OF A tIME DOMAIN FORWA	
SOLUTION	
5.1. Governing Equations For Viscoelastic Wave Propagation	
5.2. Solutions For The Wave Equations In The Laplace-Hankel Domain	
5.3. Formulation of the Stiffness Matrices for the Layer Elements	
5.3.1. Two Noded Element for a Layer with a Finite Thickness	
5.3.2. One Noded Semi-Infinite Element	
5.4. Incorporating Elastic And Viscoelastic Layer Properties	
5.5. Construction Of The Global Stiffness Matrix	
5.6. Boundary Conditions for a Circular Unit Impulse Loading at the Ground Surface.	67

5.7. Inversion Of Laplace And Hankel Transforms	68
5.8. Numerical Inversion of the Hankel Transform	
5.9. Numerical Inversion of the Laplace Transform	71
5.10. System Response To Arbitrary Loading	
CHAPTER 6 - IMPLEMENTATION AND VALIDATION OF ALGORITHM -	
VISCOWAVE	
6.1. Simulation of an Elastic Structure using ViscoWave and LAMDA	
6.2. Simulation of Viscoelastic Structures using ViscoWave	/3
CHAPTER 7 - THEORETICAL BACKCALCULATION USING VISCOWAVE	81
7.1. Review of Selected Optimization Algorithms	
7.1.1. Objective Function for Optimization and its Derivatives	
7.1.2. Basics of Iteration	
7.1.3. Gauss-Newton Method	85
7.1.4. Levenberg-Marquardt Method	86
7.1.5. Remarks on the Optimization Routine	
7.2. Theoretical Backcalculation Using ViscoWave	
7.2.1. Single Temperature Backcalculation	
7.2.1.1. Reference Pavement Structures and Seed Values for Backcalculation	87
7.2.1.2. Backcalculation Results for Pavement Structure With a Halfspace	89
7.2.1.3. Backcalculation Results for Pavement Structure on a Bedrock	
7.2.2. Multi-Temperature Backcalculation	. 109
7.2.2.1. Theoretical Development of Generalized Power Function Relationshi	p at
Multiple Temperatures	
7.2.2.2. Reference Pavement Structures and Seed Values for Backcalculation	. 110
7.2.2.3. Backcalculation Results for Pavement Structure With a Halfspace	. 112
7.2.2.4. Backcalculation Results for Pavement Structure on a Bedrock	. 117
CHAPTER 8 - FIELD BACKCALCULATION USING VISCOWAVE	123
8.1. Test Site and Protocol	
8.2. Laboratory Dynamic Modulus Test	
8.3. FWD Backcalculation Using ViscoWave	
8.3.1. Backcalculation Results from the 3 Layer System	
8.3.2. Backcalculation Results from the 5 Layer System	
CHAPTER 9 - CONCLUSIONS AND RECOMMENDATIONS	
CHAITER / - CONCLUSIONS AND RECOMMENDATIONS	, 1 1 0
RIRLIOGRAPHY	142

LIST OF TABLES

Table 2-1 Existing Dynamic Forward Solution and Backcalculation Pairs	8
Table 6-1 Layer Properties for Elastic Simulation of LAMDA and ViscoWave	74
Table 7-1 Reference Pavement Structures	88
Table 7-2 Seed Values Used for Backcalculation	88
Table 7-3 Backcalculated Values and Percent Error – Pavement on a Halfspace	93
Table 7-4 Backcalculated Values and Percent Error – Pavement on a Bedrock	103
Table 7-5 Asphalt Properties Used for Reference Pavement Structures	111
Table 7-6 Base and Subgrade Properties Used for Reference Pavement Structures	112
Table 7-7 Seed Values Used for Backcalculation.	112
Table 7-8 Backcalculated Values and Percent Error – Pavement on a Halfspace	115
Table 7-9 Backcalculated Values and Percent Error – Pavement on a Halfspace	120
Table 8-1 Assumed Pavement Properties for Backcalculation	127
Table 8-2 Seed Values Used for Backcalculation	127
Table 8-3 Backcalculated Values from 3 Layer System	128
Table 8-4 Backcalculated Values from 5 Layer System	134

LIST OF FIGURES

Figure 3-1	. Concept of Time-Temperature Superposition Principle and Mastercurve 1	8
Figure 4-1	. (a) Indirect tensile test setup and (b) specimen dimensions	57
Figure 4-2	(a) Schematic illustration of the IDT test and (b) plane stress distributions	9
Figure 5-1	Coordinate System for Axisymmetric Layers on a Halfspace	8
Figure 5-2	Bessel Functions of the First Kind	;3
Figure 5-3	Construction of the Global Stiffness Matrix for Structures (a) with and (b) without a halfspace	
Figure 6-1	Surface Deflections of a Layered Elastic Structure from (a) ViscoWave and (b) LAMDA	15
Figure 6-2	(a) Low Temperature and (b) High Temperature Asphalt Creep Compliance Curves Used for ViscoWave Simulation	'6
Figure 6-3	(a) Axisymmetric Finite Element Geometry and (b) Finite Element Mesh Used for Simulation of Pavement Response Under FWD Loading	7
Figure 6-4	Surface Deflections of a Layered Viscoelastic Structure with a Halfspace at Low Temperature Simulated Using (a) ViscoWave and (b) ADINA	18
Figure 6-5	Surface Deflections of a Layered Viscoelastic Structure with a Bedrock at 3 m below Surface at Low Temperature Simulated Using (a) ViscoWave and (b) ADINA 7	
Figure 6-6	Surface Deflections of a Layered Viscoelastic Structure with a Halfspace at High Temperature Simulated Using (a) ViscoWave and (b) ADINA	30
Figure 6-7	Surface Deflections of a Layered Viscoelastic Structure with a Bedrock at 3 m below Surface at High Temperature Simulated Using (a) ViscoWave and (b) ADINA 8	
Figure 7-1	Deflection Time Histories from Pavement Structure on a Halfspace; (a) Reference Pavement, (b) Seed Set 1, (c) Seed Set 2, and (d) Seed Set 3	90
Figure 7-2	History of Root Mean Square Error for (a) Seed Set 1, (b) Seed Set 2, and (c) Seed Set 3)1
Figure 7-3	Backcalculated Deflection Time Histories from Pavement Structure on a Halfspace; (a) Reference Pavement, (b) Seed Set 1, (c) Seed Set 2, and (d) Seed Set 39	92

Figure 7	7-4 Convergence of Power Function Parameters D_0 ; (a) Seed Set 1, (b) Seed Set 2, and (c) Seed Set 3 – Pavement Structure on a Halfspace	
Figure 7	7-5 Convergence of Power Function Parameters D_1 ; (a) Seed Set 1, (b) Seed Set 2, and (c) Seed Set 3 – Pavement Structure on a Halfspace	
Figure 7	7-6 Convergence of Power Function Parameters <i>m</i> ; (a) Seed Set 1, (b) Seed Set 2, and (Seed Set 3 – Pavement Structure on a Halfspace	
Figure 7	7-7 Convergence of Base Modulus; (a) Seed Set 1, (b) Seed Set 2, and (c) Seed Set 3 – Pavement Structure on a Halfspace	
Figure 7	7-8 Convergence of Subgrade Modulus; (a) Seed Set 1, (b) Seed Set 2, and (c) Seed Set – Pavement Structure on a Halfspace	
Figure 7	7-9 Deflection Time Histories from Pavement Structure on a Bedrock; (a) Reference Pavement, (b) Seed Set 1, (c) Seed Set 2, and (d) Seed Set 3	100
Figure 7	7-10 History of Root Mean Square Error for (a) Seed Set 1, (b) Seed Set 2, and (c) Seed Set 3	
Figure 7	7-11 Backcalculated Deflection Time Histories from Pavement Structure on a Bedrock (a) Reference Pavement, (b) Seed Set 1, (c) Seed Set 2, and (d) Seed Set 3	_
Figure 7	7-12 Convergence of Power Function Parameters D_0 ; (a) Seed Set 1, (b) Seed Set 2, and (c) Seed Set 3 – Pavement Structure on a Bedrock	
Figure 7	7-13 Convergence of Power Function Parameters D_1 ; (a) Seed Set 1, (b) Seed Set 2, and (c) Seed Set 3 – Pavement Structure on a Bedrock	
Figure 7	7-14 Convergence of Power Function Parameters <i>m</i> ; (a) Seed Set 1, (b) Seed Set 2, and (c) Seed Set 3 – Pavement Structure on a Bedrock	
Figure 7	7-15 Convergence of Base Modulus; (a) Seed Set 1, (b) Seed Set 2, and (c) Seed Set 3 - Pavement Structure on a Bedrock	
Figure 7	7-16 Convergence of Subgrade Modulus; (a) Seed Set 1, (b) Seed Set 2, and (c) Seed S 3 – Pavement Structure on a Bedrock	
Figure 7	7-17 Time-Temperature Shift Factors	111
Figure 7	7-18 Creep Compliance Curves at Multiple Temperatures	111
Figure 7	7-19 Simulated FWD Deflection Time Histories for (a) 0°C, (b) 10°C, (c) 20°C, and (d 40°C	
Figure 7	7-20 Seed FWD Deflection Time History for All Temperatures	114

Figure 7-21 History of Root Mean Square Error	115
Figure 7-22 Convergence of Power Function Parameters (a) D_0 , (b) D_1 , and (c) m – Structure on a Halfspace	
Figure 7-23 Convergence of (a) Base and (b) Subgrade Layer Moduli – Pavement S Halfspace	
Figure 7-24 Simulated FWD Deflection Time Histories for (a) 0°C, (b) 10°C, (c) 20 40°C	
Figure 7-25 Seed FWD Deflection Time History for All Temperatures	119
Figure 7-26 History of Root Mean Square Error	120
Figure 7-27 Convergence of Power Function Parameters (a) D_0 , (b) D_1 , and (c) m – Structure on a Bedrock	
Figure 7-28 Convergence of (a) Base and (b) Subgrade Layer Moduli – Pavement S Bedrock	
Figure 8-1 Laboratory Dynamic Modulus Mastercurves	125
Figure 8-2 Laboratory Time-Temperature Shift Factors	125
Figure 8-3 Measured FWD (a) Load and (b) Deflection Time Histories	126
Figure 8-4 History of Root Mean Square Error for the 3 Layer System	128
Figure 8-5 Simulated Time Histories for the 3 layer System with (a) Seed and (b) Ba Values	
Figure 8-6 Convergence of Power Function Parameters (a) D_0 , (b) D_1 , and (c) $m-3$ System	
Figure 8-7 Convergence of Unbound Pavement Layer Moduli for the 3 Layer System and (b) Subgrade	` /
Figure 8-8 (a) Seed and (b) Backcalculated Creep Compliance Functions from 3 Lag	
Figure 8-9 Backcalculated Dynamic Modulus Mastercurves at Reference Temperatu and (b) 10°C – 3 Layer System	` /
Figure 8-10 History of Root Mean Square Error for the 5 Layer System	133

Figure 8-11 Simulated Time Histories for the 5 layer System with (a) Seed and (b) Backcalculated Values	135
Figure 8-12 Convergence of Power Function Parameters (a) D_0 , (b) D_1 , and (c) $m-5$ Layer System	136
Figure 8-13 Convergence of Unbound Pavement Layer Moduli for the 3 Layer System (a) Ba (b) Subgrade, (c) Embankment 1, and (d) Embankment 2	
Figure 8-14 (a) Seed and (b) Backcalculated Creep Compliance Functions from 5 Layer Systems	
Figure 8-15 Backcalculated Dynamic Modulus Mastercurves at Reference Temperatures (a) 58°C and (b) 10°C – 5 Layer System	139

CHAPTER 1 - INTRODUCTION

1.1. General

The use of a Falling Weight Deflectometer (FWD) is one of the most frequently employed nondestructive testing (NDT) methods for evaluating the structural integrity of an existing pavement. As its full name implies, the FWD is equipped with a falling mass mechanism capable of inducing an impact load on the pavement surface. Due to the nature of the impact load generated by a falling mass, the load typically has a short duration (usually 20 ms to 40 ms) and gives rise to a stress wave that propagates through the pavement structure. The resulting time dependent response of the pavement structure or more specifically, the vertical deflection at the pavement surface resulting from the stress wave is measured at various radial distances from the load and is recorded for the structural analysis of the pavement system.

The process of estimating material parameters from the FWD data can be categorized as an inverse problem whose objective is to determine the system characteristics (e.g., layer modulus) from the known input (e.g., applied load) and output (e.g., measured deflection). In the pavement engineering community, such inverse problems have typically been solved using a procedure commonly referred to as backcalculation.

In general, backcalculation of layer parameters is carried out by matching the FWD load and deflection to those from a theoretical model. Therefore, as is the case for most inverse problems, the two crucial components of a backcalculation methodology are (1) a forward solution or a theoretical model capable of simulating the FWD load and deflection, and (2) an iterative or

statistical routine capable of determining the optimum layer parameters that minimize the error between the measured and simulated results.

1.2. Problem Statement

The forward models adopted for use in the dynamic backcalculation methodologies are typically based on the solutions that stem from the theory of elastic wave propagation. One of the common characteristics of these available solutions is that the analytical developments for solving the wave equations were made in the frequency domain. As a result, these solutions commonly utilized the Discrete Fourier Transform (DFT) algorithm for converting the load and deflection signals from the time domain to the frequency domain.

However, there has been varying levels of success in dynamic backcalculation using the theoretical time histories generated by the forward solution. Furthermore, dynamic backcalculation using the field FWD data has generally shown fair to poor level of success and still remains a challenge in the field of pavement engineering. Since it is recognized that the difficulties in dynamic backcalculation arose from the forward solutions derived in the frequency domain and from the use of the discrete transforms, it is emphasized that there is a need for a more suitable forward solution for dynamic backcalculation in time domain. It is believed that such a solution should not only eliminate the difficulties inherent to the solutions derived in the frequency domain but also allow for modeling the wave propagation phenomenon while accounting for the fundamental viscoelastic properties in a more appropriate manner.

1.3. Research Objective

The primary objective of this research is to develop a new forward solution that could be used for dynamic backcalculation in time domain. In order to overcome some of the drawbacks related to the discrete transforms, the new solution will utilize continuous integral transforms that are more appropriate for transient, nonperiodic time domain signals such as the FWD time histories.

Then, the resulting algorithm is to be verified against some of the existing solutions that are capable of modeling the FWD time histories. In addition, sensitivity analyses will be conducted in order to understand the behavior of various pavement structures subjected to FWD loading.

The research will also look into using the developed algorithm as a forward engine for dynamic backcalculation. A feasible backcalculation algorithm will be recommended based on the lessons learned from the sensitivity analyses.

1.4. Report Layout

The remainder of the dissertation is organized as follows:

Chapter 2 provides a brief review of the existing dynamic solutions typically used for backcalculation. It also addresses some of the difficulties that are present in the backcalculation procedures frequently being used currently.

Chapter 3 provides a brief review of the uniaxial theory of linear viscoelasticity. The fundamental properties of a viscoelastic material will be described in both the time and the frequency domains. Then, the time-temperature superposition of a thermo-rheologically simple (viscoelastic) material will be reviewed. In addition, a review of the analytical models frequently used for modeling the viscoelastic constitutive relations is provided with a discussion on the interconversion of various viscoelastic properties. Finally, the chapter concludes with a brief discussion on the elastic-viscoelastic correspondence principle in the uniaxial mode.

Chapter 4 builds upon the uniaxial theory of viscoelasticity in Chapter 3 and provides a brief review of the multi-axial theory of viscoelasticity. The chapter begins with an introduction to the viscoelastic Poisson's ratio which is critical in the development of the multi-axial viscoelasticity and the extended elastic-viscoelastic correspondence principle. Then, a methodology for applying the multi-axial viscoelasticity in the analysis of the laboratory Indirect Tensile (IDT) test is presented. This chapter is critical since the viscoelastic properties backcalculated from the FWD data are compared to those obtained from the IDT tests.

Chapter 5 describes in detail, the mathematical development of the new algorithm. The theoretical development for the proposed methodology follows similar steps to those used for the development of LAMDA, the spectral element method which utilized the discrete transforms for solving the wave equations. However, the proposed solution utilizes the continuous integral transforms (namely Laplace and Hankel transforms) that are more appropriate for transient, nonperiodic signals.

Chapter 6 presents the verification results for the developed algorithm which is done through comparing the simulation results from the developed algorithm to some of the other existing solutions.

Chapter 7 provides a brief mathematical background on the iteration schemes selected for use with the new forward solution developed in this research. Then the iteration algorithms are tested using theoretically generated deflection time histories. The results of the theoretical backcalculation provided in this chapter for both the single and multiple temperature backcalculation.

Chapter 8 presents the results of the preliminary backcalculation exercise using the field-measured FWD data. Then the backcalculated results are compared to those obtained from the laboratory.

Chapter 9 summarizes the findings of the current research and some recommendations for future research.

CHAPTER 2 - LITERATURE REVIEW

Evidently, the forward solutions used for the static backcalculation procedures assume that the pavement structure under the applied load is in static equilibrium. In other words, these solutions do not allow for simulating the FWD load and deflection as functions of time. Correspondingly, the material properties adopted for use in these solutions have been acquired from the constitutive models that do not depend on time – e.g., linear elastic (Uzan et. al., 1988) and nonlinear elastic (Irwin, 1977) models. Because the time dependent solution cannot be achieved, only the peak magnitude of the impact load and the peak deflection measured at different sensor locations (also known as the deflection basin or deflection bowl) are taken into account in the backcalculation process. Although the static backcalculation methods are extremely efficient, these solutions do not properly account for the dynamic (time dependent) nature of the FWD load and deflection.

As it has been proven by numerous researchers in the past, asphalt mixtures that comprise the top layer of flexible pavements are viscoelastic in nature. Unlike an elastic material, because their fundamental properties are time or frequency dependent, viscoelastic materials such as an asphalt mixture show time dependent response even under a static (or constant) load (A review of the theory of linear viscoelasticity will be provided in the next chapter and hence it will not be discussed extensively as part of this chapter). The forward solution such as the ones recently developed by Kim (2011) and Kutay et. al. (2011) accounts for such material time dependency through the use of viscoelastic constitutive relations. The primary advantage of such forward models is that they allow for simulating the FWD time histories without a significant loss of

computational efficiency. However, as it was pointed out by Kutay et. al. (2011), because the viscoelastic solutions do not consider the effect of wave propagation attributed to the impact load, they are not capable of modeling the different time delays measured at different sensors as well as the free vibration of the pavement structure which may be significant in the presence of a stiff layer (e.g., a bedrock) at shallow depth.

Some of the existing dynamic forward and inverse solution pairs are summarized in Table 2-1. The forward models adopted for use in the dynamic backcalculation methodologies are typically based on the solutions that stem from the theory of elastic wave propagation. Therefore, the stress wave propagation is naturally modeled in these solutions. The viscoelasticity of the material typically has been taken into consideration through the use of a damping ratio which is a concept derived from the theory of vibrations (Chatti and Yun, 1996, Chatti et. al., 2004, Ji, 2005, Matsui et. al., 2011). Excluding the solutions based on the Finite Element Analysis (FEA) that are generally more time consuming and inefficient for backcalculation (Hadidi and Gucunski, 2007), the dynamic forward solutions can be categorized into the finite layer type (Chatti and Yun, 1996, Chatti et. al., 2004, Ji, 2005, Matsui et. al., 2011) or the spectral element type solutions (Al-Khoury et. al., 2001a, 2001b, & 2002, Grenier and Konrad, 2007). However, one of the common characteristics of both solution types is that the analytical developments for solving the wave equations were made in the frequency domain. As a result, these solutions commonly utilized the Discrete Fourier Transform (DFT) algorithm for converting the load and deflection signals from the time domain to the frequency domain.

Table 2-1 Existing Dynamic Forward Solution and Backcalculation Pairs

Program Name	Forward Calculation Program	Backcalculation Method	Domain	Developed By
PAVE-SID	SCALPOT	System Identification (SID)	Frequency	Magnuson, et. al. (1991)
FEDPAN	SAP IV	Linear Least-Squares	Time	Ong, et. al. (1991)
No Name	UTFWIBM	Newton's Method	Frequency/Time	Ujan, et. al. (1994)
BKGREEN	GREEN	Nonlinear Least-Squares	Frequency	Kang, Y. V. (1998)
No Name	FEA	Gauss-Newton	Time	Matsui, et. al. (1998)
No Name	SAPSI	Levenberg-Marquardt	Frequency	Losa (2002)
No Name	LAMDA	Secant Update, Levenberg-Marquardt, Powell Hybrid	Frequency	Al-Khoury, et. al. (2002)
DYNABACK- F/T	SAPSI	Newton Raphson Method	Frequency/Time	Ji (2005)
No Name	FEA	Neighborhood Algorithm	Time	Hadidi and Gucunski (2007)
UCODE	DYNAPAV-UL	Levenberg-Marquardt	Time	Grenier and Konrad (2007)

As it was pointed out by Bendat and Piersol (2010), the aforementioned discrete transform is not appropriate for transient nonperiodic signals such as those generated by the FWD. Some of the drawbacks and difficulties arising from the use of the discrete transform that are documented in

the dynamic backcalculation literature can be summarized as: (1) the truncation in the FWD time histories – i.e., the recording of the signal being terminated before the pavement system has come to a rest, which acts like a box filter applied to the signal, (2) the periodicity of the signal assumed in the discrete DFT algorithm not being able to accurately disclose the frequency content of the transient FWD time histories with short duration, (3) the DFT being very sensitive to noise that is always present in the FWD data (Chatti et. al., 2004, Ji, 2005, Matsui et. al., 2011), and (4) the DFT being impractical for representing the fundamental properties of a viscoelastic material such as creep compliance or dynamic modulus, due to a large number of harmonics necessary for modeling them (Zhang et. al., 1997a, 1997b) – this is also the reason behind most of the frequency domain solutions utilizing the damping ratio concept and hence failing to model and/or backcalculate the fundamental properties of a viscoelastic material.

CHAPTER 3 - REVIEW OF UNIAXIAL THEORY OF LINEAR VISCOELASTICITY

Prior to the presentation of the mathematical formulation of the developed algorithm, it is necessary to review the constitutive relation of a viscoelastic material. Therefore, this chapter is dedicated to providing a theoretical review on the fundamental properties of a viscoelastic material and the theory of linear viscoelasticity.

3.1. Fundamental Properties of a Viscoelastic Material in Time Domain

According to the theory of linear viscoelasticity, the time-dependent stress-strain relationship of a viscoelastic material subjected to a constant uniaxial stress, σ_0 , can be expressed as the creep compliance, D(t):

$$D(t) = \frac{\varepsilon(t)}{\sigma_0} \text{ for } t \ge 0$$
 (3-1)

where $\varepsilon(t)$ is the resulting time dependent strain. The strain resulting from any stress history can be expressed in the form of a convolution integral by means of the Boltzman's superposition principle as:

$$\varepsilon(t) = \int_{0}^{t} D(t - \tau) \frac{\partial \sigma(\tau)}{\partial \tau} d\tau \tag{3-2}$$

where τ is the integral variable.

On the other hand, the relaxation modulus, E(t), is defined as the time dependent stress resulting from an applied step of constant unit strain, that is:

$$E(t) = \frac{\sigma(t)}{\varepsilon_0} \text{ for } t \ge 0$$
 (3-3)

where $\sigma(t)$ is the resulting time dependent stress and ε_0 is the magnitude of the constant strain. With the relaxation modulus defined as above, the stress history resulting from any strain history can be expressed as:

$$\sigma(t) = \int_{0}^{t} E(t - \tau) \frac{\partial \varepsilon(t)}{\partial \tau} d\tau \tag{3-4}$$

3.2. Fundamental Properties of a Viscoelastic Material in Frequency Domain

In the frequency domain, the sinusoidal oscillations of stress and strain are commonly represented by complex variables through Euler's formula:

$$\sigma(t) = \sigma_0 e^{i\omega t} = \sigma_0 (\cos \omega t + i \sin \omega t)$$
(3-5)

where σ_0 and ω are the amplitude and the angular frequency of the axial stress oscillation. The resulting strain, $\varepsilon(t)$, at a steady state oscillates at the same frequency as the stress oscillation but with a phase angle:

$$\varepsilon(t) = \varepsilon_0 \cdot e^{i\{\omega t - \delta\}} = \varepsilon * \cdot e^{i\omega t}$$
(3-6)

where ε_0 is the strain amplitude, δ is the phase angle by which the strain lags behind the stress, and ε^* is a complex strain amplitude defined as:

$$\varepsilon^* = \varepsilon_0 \cdot e^{-i\delta} = \varepsilon_0 (\cos \delta - i \sin \delta) \tag{3-7}$$

The complex compliance defined as the strain over stress can be obtained from Equations (3-5) and (3-7), analogous to the creep compliance as follows:

$$D^*(\omega) = D'(\omega) - D''(\omega) = \frac{\varepsilon^*}{\sigma_0} = \frac{\varepsilon_0}{\sigma_0} \cdot e^{-i\delta}$$
 (3-8)

where $D'(\omega)$ and $D''(\omega)$ are the real and imaginary parts of the complex compliance. Similarly, if the viscoelastic material is subjected to a sinusoidal strain oscillation, that is:

$$\varepsilon(t) = \varepsilon_0 e^{i\omega t} = \varepsilon_0 (\cos \omega t + i \sin \omega t)$$
 (3-9)

Then, the resulting stress is:

$$\sigma(t) = \sigma_0 \cdot e^{i\{\omega t + \delta\}} = \sigma \cdot e^{i\omega t}$$
(3-10)

where σ^* is the complex stress amplitude defined as:

$$\sigma^* = \sigma_0 \cdot e^{i\delta} = \sigma_0 (\cos \delta + i \sin \delta) \tag{3-11}$$

The complex modulus is defined as the ratio between the complex stress amplitude, σ^* , over the input strain amplitude ε_0 :

$$E^*(\omega) = E'(\omega) + E''(\omega) = \frac{\sigma^*}{\varepsilon_0} = \frac{\sigma_0}{\varepsilon_0} \cdot e^{i\delta}$$
 (3-12)

where $E'(\omega)$ and $E''(\omega)$ are the real and imaginary parts of the complex modulus.

It is also worthwhile to note that within the field of pavement engineering, the magnitude of the complex modulus given as the following equation has frequently been referred to using the term "Dynamic Modulus" (Kim, 2009).

$$\left|E^*(\omega)\right| = \sqrt{\left\{E'(\omega)\right\}^2 + \left\{E''(\omega)\right\}^2} \tag{3-13}$$

3.3. Relationship between Viscoelastic Properties

Since creep and stress relaxation phenomena are two aspects of the same viscoelastic behavior of a given material, they are obviously related. In other words, the viscoelastic properties presented above are not independent of each other. However, determining the relationship between the fundamental properties in time domain becomes quite tedious (although possible) due to the convolution integrals shown in Equations (3-2) and (3-4). Instead, it is more convenient to derive

the relationships in the Laplace domain. Taking the Laplace transform on Equations (3-2) and (3-4) yields the following:

$$\widehat{\varepsilon}(s) = s\widehat{D}(s)\widehat{\sigma}(s) \tag{3-14}$$

$$\widehat{\sigma}(s) = s\widehat{E}(s)\widehat{\varepsilon}(s) \tag{3-15}$$

where s is the Laplace variable and $L[f(t)] = \hat{f}(s) = \int_0^\infty e^{-st} f(t) dt$ is the Laplace transform of the function f(t). By combining the two equations above, the relationship between creep compliance and relaxation modulus can be expressed as an algebraic equation in the Laplace domain as follows:

$$\hat{D}(s)\hat{E}(s) = 1/s^2 \tag{3-16}$$

The inverse Laplace transform of the above equation reveals the relationship between the creep compliance and relaxation modulus in time domain:

$$\int_{0}^{t} E(t-\tau)D(\tau)d\tau = \int_{0}^{t} E(\tau)D(t-\tau)d\tau = t$$
(3-17)

In the frequency domain, the relationship between the complex compliance and the complex modulus can easily be derived by combining Equations (3-8) and (3-12) as:

$$D^*(\omega) \cdot E^*(\omega) = 1 \tag{3-18}$$

In addition, the relationship between the complex compliance and the creep compliance can be obtained by substituting Equations (3-5) and (3-7) into Equation (3-2). After rearranging the variables, the final relationship can be written as (Findley et al, 1976):

$$D^*(\omega) = i\omega \cdot \hat{D}(s)|_{s=i\omega}$$
(3-19)

The relationship between the complex modulus and the relaxation modulus can be obtained in a similar manner. Substituting Equations (3-9) and (3-11) into Equation (3-4) results in the following upon summarizing:

$$E^*(\omega) = i\omega \cdot \hat{E}(s)|_{s=i\omega}$$
(3-20)

Although the detailed derivation for Equations (3-19) and (3-20) is omitted here, similar derivation will be shown in the following chapter for the viscoelastic Poisson's ratio (Section 4.1.3).

3.4. Time-Temperature Superposition Principle

As it has been reported by several researchers in the past, the behavior of a viscoelastic material is strongly affected by temperature (Findley et. al., 1976, Tschoegl, 1989, Wineman and Rajagopal, 2000). However, the constitutive relations provided so far did not account for the

effect of temperature (since the fundamental properties were assumed to be function of time only) and hence, they should be used only when the material is subjected to a constant temperature. In order to account for the effect of temperature, it is necessary to generalize the fundamental properties described above to include temperature as an independent variable. For example, the relaxation modulus can now be defined as:

$$E = E(t, T) \tag{3-21}$$

where the uppercase T has been used for temperature to distinguish from the time variable, t.

Fortunately, there has been sufficient theoretical and experimental evidence showing that most linearly viscoelastic materials obey the Time-Temperature Superposition Principle (TTSP) which allows for combining the effect of time and temperature (Findley et. al., 1976, Tschoegl, 1989, Wineman and Rajagopal, 2000). A viscoelastic material obeying the TTSP is also frequently referred to as a "Thermorheologically Simple" material. According to the TTSP, the above relaxation modulus can be written as the following:

$$E = E(t,T) = E(\xi,T_0)$$
 (3-22)

where T_0 is the reference temperature and ξ is called the "Reduced Time" which is related to the physical time in the following manner:

$$\xi = t/a_T(T) \tag{3-23}$$

where $a_{\rm T}$ is the shift factor. The above equation can be also be written as:

$$\log(\xi) = \log(t/a_T(T)) = \log(t) - \log(a_T(T)) \tag{3-24}$$

The above equations indicate that fundamental property of a viscoelastic material at the time t and at temperature T is equal to that property at the reduced time ξ and at the reference temperature T_0 . This in turn, indicates that the fundamental properties at different temperatures can be shifted by the amount $\log(a_T)$ when plotted in log-scale (or stretched/shrunk in arithmetic-scale), as shown conceptually in Figure 3-1.

As shown in the figure, once the fundamental properties obtained from multiple temperatures have been shifted to their equivalent at the reference temperature T_0 , it results in a curve representing the viscoelastic material property for a wide range of frequencies (or time) and is called the mastercurve of a viscoelastic material.

In reality, testing of a viscoelastic material for its characterization is typically conducted at a limited range of frequencies or for a short duration of time. This is due to (1) the limitations of the testing equipment (e.g., the duration of the FWD load is typically between 20 ms and 40 ms) and (2) the specimen being damaged when tested for a long period of time (or a wide range of frequencies). In that sense, the TTSP provides a great deal of advantage for characterization of viscoelastic material properties because it provides a methodology for overcoming this problem. In other words, instead of testing the material at a wide range of frequencies or time, the TTSP

allows for testing the material at multiple temperatures (and at a limited range of frequencies or time) and providing the same mastercurve.

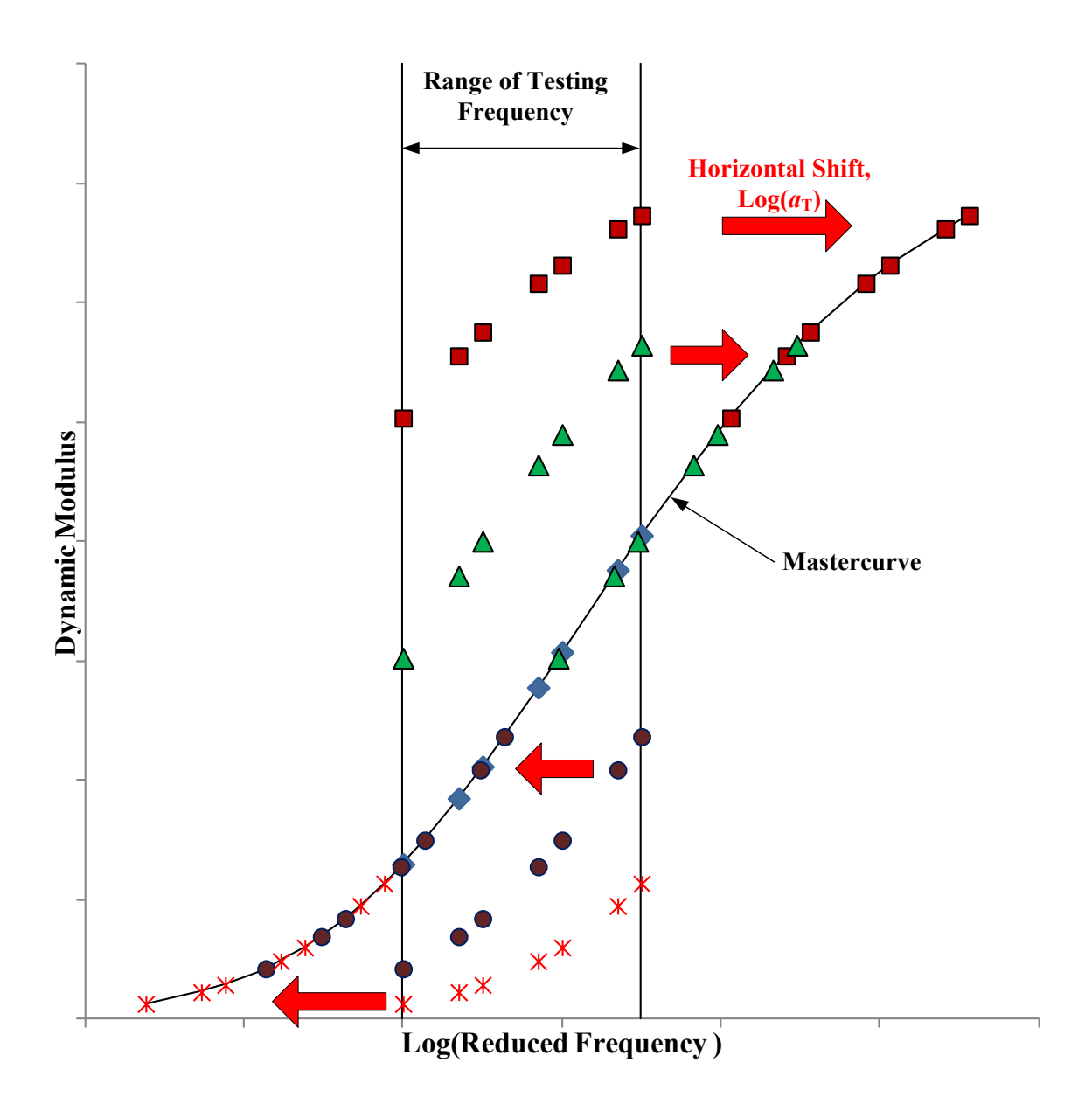


Figure 3-1. Concept of Time-Temperature Superposition Principle and Mastercurve (For interpretation of the references to color in this and all other figures, the reader is referred to the electronic version of this dissertation).

3.5. Analytical Models for Viscoelastic Properties

Numerous closed form equations have been proposed and used to model the fundamental properties of a viscoelastic material and they will be briefly reviewed in this section. Although the equations will be presented in the form of creep compliance or relaxation modulus, they can generally be used to model both (Kim, 2009).

One of the simplest equations for modeling the viscoelastic property is the pure power function shown below:

$$D(t) = D_1 \cdot t^m \tag{3-25}$$

where D_1 and m are the power function parameters. The Laplace transform of the above equation is given as:

$$\widehat{D}(s) = \frac{D_1 \Gamma(m+1)}{s^{m+1}} \tag{3-26}$$

where $\Gamma(m)$ is the gamma function.

Although the above equation is very simple, the critical disadvantage of the pure power function is that it does not account for the instantaneous (or elastic) response of the viscoelastic material which may become important at low temperatures.

Alternatively, the generalized power function still maintains a simple form while representing the viscoelastic property effectively. The function is expressed as:

$$D(t) = D_0 + D_1 \cdot t^m \tag{3-27}$$

where D_0 , D_1 , and m are the power function parameters. The disadvantage of the above equation is that it fails to model the entire creep compliance (or dynamic modulus) mastercurve which spans over a wide range of temperature and frequency. Nevertheless, it has been shown that the generalized power function is an excellent analytical representation of the uniaxial viscoelastic creep compliance at a single temperature (Roque et al. 1997, Roque et al. 1998, Kim et al. 2005, and Kim et al. 2008). In addition, it has been shown by some of the previous research studies (Lee et. al., 2012, and Kim et. al. 2010) that the generalized power function can be used successfully to fit the laboratory test data for each temperature prior to fitting the master curve using a sigmoidal function proposed by the latest Mechanistic-Empirical Pavement Design Guide (MEPDG) (ARA, 2004). Therefore, it was decided to use the generalized power function for modeling the viscoelastic material behavior in this research. Taking the Laplace transform on the above equation results in:

$$\widehat{D}(s) = \frac{D_0 s^m + D_1 \Gamma(m+1)}{s^{m+1}}$$
 (3-28)

On the other extreme, the modified power function shown below is one of the most complicated closed form equations that have been used for modeling the viscoelastic creep compliance.

$$D(t) = D_0 + \sum_{i=1}^{M} \frac{D_i}{\left(1 + \frac{\tau_i}{t}\right)^n}$$
 (3-29)

where D_0 , D_i , τ_i , and n are the parameters for the modified power function. Although the above function is generalized enough so that the entire creep compliance mastercurve can be fitted, taking the Laplace transform of the above equation is close to impossible due to its complicated form and the number of parameters involved.

The recent Mechanistic-Empirical Pavement Design Guide (MEPDG) has adopted the sigmoidal function for representing the mastercurve which is given as the following (ARA, 2004):

$$\log(|E^*|) = \delta + \frac{\alpha}{1 + e^{\beta - \gamma \log(\xi)}}$$
 (3-30)

where α , β , γ , and δ are the parameters for the sigmoidal function. The advantage of the above equation is that the mastercurve can be fitted accurately with less number of parameters when compared to the modified power function. Nonetheless, as it was the case for the modified power function, the Laplace transform of the above cannot be obtained in closed form.

3.6. Prony Series

Although the analytical functions introduced above have been successfully used as fitting functions that represent the viscoelastic behavior of materials, mathematical difficulties arise

when attempting the strict analytical interconversion of the fundamental properties necessary for the stress or strain development under various loading conditions in viscoelastic media. For example, the Laplace transforms of the modified power function and the sigmoidal function cannot be obtained in closed form and hence the interconversion equations presented earlier cannot be used directly.

Although the Laplace transforms of the pure power function and the generalized power function can be obtained analytically, they still fail to provide an analytical interconversion of the viscoelastic properties. For example, substituting Equation (3-27) into Equation (3-16) results in the following for the relaxation modulus in the Laplace domain whose inverse transform cannot be carried out analytically:

$$\widehat{E}(s) = \frac{s^{m-1}}{D_0 s^m + D_1 \Gamma(m+1)}$$
(3-31)

Furthermore, substituting Equation (3-27) into Equation (3-19) results in a non-integer power of the ($i\omega$) term (since 0 < m < 1), which in turn yields a non-unique solution for the complex compliance (Findley et. al., 1976).

Instead, Prony series (generalized model), which has one Maxwell model (a spring element and dashpot element connected in series) and several Kelvin elements (a spring element and dashpot element connected in parallel), has been widely used for analytical representation of viscoelastic materials due to its remarkable computational efficiency. For creep compliance, the Prony series representation is of the following form:

$$D(t) = D_0 + \frac{1}{\eta}t + \sum_{i=1}^{N} D_i (1 - e^{-\frac{t}{\tau_i}})$$
(3-32)

where D_0 , and D_i are Prony series parameters, η is the dashpot constant, and τ_i are retardation times.

Prony series is convenient for viscoelastic analysis in cases where the stress history is prescribed, whereas the generalized Maxwell model, which is several Maxwell elements connected in parallel, is rather convenient for predicting stress associated with a prescribed strain. Therefore, converting creep compliance to relaxation modulus is the process of converting the Prony series to the generalized Maxwell model. Taking the Laplace transform on the above equation results in:

$$\widehat{D}(s) = \frac{D_0}{s} + \frac{1}{\eta \cdot s^2} + \sum_{i=1}^{N} \frac{D_i}{s \cdot (\tau_i \cdot s + 1)}$$
(3-33)

Substituting the above into Equation (3-16) yields the following equation for the relaxation modulus in the Laplace domain:

$$\widehat{E}(s) = \frac{1}{s \left(D_0 + \frac{1}{\eta \cdot s} + \sum_{i=1}^{N} \frac{D_i}{(\tau_i \cdot s + 1)} \right)}$$
(3-34)

The above equation can be rearranged as a ratio of two polynomials of *s*:

$$\hat{E}(s) = \frac{(a_{M-1} \cdot s^{M-1} + a_{M-2} \cdot s^{M-2} + \dots + a_1)}{(b_M \cdot s^M + b_{M-1} s^{M-1} + \dots + b_1)}$$
(3-35)

where, a and b are the coefficients of polynomial functions. Expanding Equation (3-35) by partial fractions yields the following form:

$$\hat{E}(s) = \frac{E_1}{s + \frac{1}{\rho_1}} + \frac{E_2}{s + \frac{1}{\rho_2}} + \dots + \frac{E_M}{s + \frac{1}{\rho_M}}$$
(3-36)

where, $1/\rho_1$, $1/\rho_2$, etc., are the roots of the denominator in Equation (3-35), and E_1 , E_2 , etc., are numerators that satisfy the partial fractions (the terms ρ_i are frequently called the relaxation times in the literature). Performing inverse Laplace transformation finally yields the generalized Maxwell model in parallel (Prony series for relaxation modulus):

$$E(t) = E_1 \cdot e^{-\frac{t}{\rho_1}} + E_2 \cdot e^{-\frac{t}{\rho_2}} + \dots + E_M \cdot e^{-\frac{t}{\rho_M}} = \sum_{i=1}^M E_i \cdot e^{-\frac{t}{\rho_i}}$$
(3-37)

Frequently, the Prony series of the following form is used in which the term including the dashpot constant is eliminated by setting $\eta \to 0$ in Equation (3-32), that is:

$$D(t) = D_0 + \sum_{i=1}^{N} D_i (1 - e^{-\frac{t}{\tau_i}})$$
(3-38)

Following the same procedure above, it can be shown that the relaxation modulus corresponding to Equation (3-38) is obtained as:

$$E(t) = E_0 + \sum_{i=1}^{M} E_i \cdot e^{-\frac{t}{\rho_i}}$$
(3-39)

Using the Prony series presented above, their frequency domain counterparts can also be derived easily. Substituting Equation (3-33) into Equation (3-19) results in the Prony representation of the complex compliance:

$$D'(\omega) = D_0 + \sum_{i=1}^{N} \frac{D_i}{\varpi^2 \tau_i^2 + 1}$$
 (3-40)

$$D''(\omega) = \frac{1}{\eta \varpi} + \sum_{i=1}^{N} \frac{\varpi \tau_i D_i}{\varpi^2 \tau_i^2 + 1}$$
(3-41)

Similarly, the Prony representation for the complex modulus can be obtained by substituting Equation (3-36) into Equation (3-20). Upon summarizing, the outcome is given as:

$$E'(\omega) = \sum_{i=1}^{M} \frac{\varpi^2 \rho_i^2 E_i}{\varpi^2 \rho_i^2 + 1}$$
 (3-42)

$$E''(\omega) = \sum_{i=1}^{M} \frac{\varpi \rho_i E_i}{\varpi^2 \rho_i^2 + 1}$$
(3-43)

3.7. Elastic-Viscoelastic Correspondence Principle

The uniaxial constitutive equation for a linear elastic material is given as the well known Hooke's law:

$$\sigma = E\varepsilon \tag{3-44}$$

where σ , ε , and E are the stress, strain, and the Young's modulus, respectively. Alternatively, the above equation can also be written in terms of the elastic compliance D=1/E as:

$$\varepsilon = D\sigma \tag{3-45}$$

By comparing Equation (3-44) to Equations (3-15) and (3-12), it can be seen that replacing the Young's modulus, E, in Equation (3-44) by $s\hat{E}(s)$ and E^* results in the uniaxial viscoelastic constitutive relation in the Laplace domain as shown in Equation (3-15) and in the frequency domain as shown in Equation (3-12), respectively. Similarly, replacing the elastic compliance, D, in Equation (3-45) with $s\hat{D}(s)$ yields the viscoelastic equation shown in Equation (3-14) while replacing it with the complex compliance, D^* , results in the constitutive equation shown in Equation (3-8). This indicates that the viscoelastic constitutive relation can be obtained easily in the Laplace domain or in the frequency domain if the elastic constitutive relation is determined and the elastic constants are replaced with their appropriate viscoelastic counterparts. This is known as the elastic-viscoelastic correspondence principle. Although it seems obvious and trivial

in the uniaxial case shown here, the elastic-viscoelastic correspondence principle will prevail a great advantage in the multi-axial viscoelasticity which will be discussed later.

CHAPTER 4 - EXTENSION TO MULTI-AXIAL VISCOELASTICITY AND ANALYSIS OF INDIRECT TENSILE TEST DATA

In this chapter, the theory of viscoelasticity introduced in the previous chapter will be extended to multi-axial viscoelasticity. After a brief theoretical development, the methodology for analyzing the laboratory Indirect Tensile (IDT) test data will be presented.

4.1. Viscoelastic Poisson's Ratio

4.1.1. Viscoelastic Poisson's Ratio in Time Domain

Tschoegl (1989), Wineman and Rajagopal (2000), and Tschoegl et al (2002) emphasized that the time-dependent Poisson's ratio, v(t), of a linearly isotropic viscoelastic material should be defined as the ratio of the time dependent lateral strain, $\varepsilon_2(t)$, to a constant axial strain, ε_1^0 . By the definition, Poisson's ratio is expressed as:

$$\nu(t) = -\frac{\varepsilon_2(t)}{\varepsilon_1^0} \text{ for } t \ge 0$$
 (4-1)

The above definition implies that the theoretical viscoelastic Poisson's ratio can be obtained from a uniaxial relaxation test in which the strain in the axial direction is held constant. The definition also reveals that Poisson's ratio cannot be obtained directly by taking the ratio of the time-dependent strains resulting from a uniaxial creep test because in this testing mode, the axial

stress is held constant rather than the axial strain. Hence, the ratio of $\varepsilon_1(t)$ and $\varepsilon_2(t)$ directly measured from a creep test cannot be termed Poisson's ratio (Tschoegl et al, 2002).

From the definition of the Poisson's ratio shown in Equation (4-1), one can observe that the Poisson's ratio is the lateral strain as a function of time resulting from a unit step strain applied in the axial direction. Therefore, for any given time-dependent axial strain function, $\varepsilon_1(t)$, the resulting lateral strain, $\varepsilon_2(t)$, is given as a convolution integral (observe the similarities between Equations (3-3), (3-4), (4-1), and (4-2)):

$$\varepsilon_2(t) = -\int_0^t v(t-\tau) \frac{\partial \varepsilon_1(\tau)}{\partial \tau} d\tau \tag{4-2}$$

Taking Laplace transform on the above equation yields:

$$\widehat{\varepsilon}_2(s) = -s\,\widehat{v}(s)\widehat{\varepsilon}_1(s) \tag{4-3}$$

Equation (11) can also be expressed in terms of the axial stress, $\hat{\sigma}_1(s)$, by means of Equation (3):

$$\widehat{\varepsilon}_{2}(s) = -s^{2}\widehat{v}(s)\widehat{D}(s)\widehat{\sigma}_{1}(s) \tag{4-4}$$

4.1.2. Viscoelastic Poisson's Ratio in Frequency Domain

Similar to Poisson's ratio in the time domain that was defined under the uniaxial relaxation testing mode, Poisson's ratio in the frequency domain can be defined under a uniaxial, strain-controlled complex modulus testing mode as (Tschoegl, 1989 and Tschoegl et al., 2002):

$$v^*(\omega) = -\frac{\varepsilon_2^0 e^{i(\omega t - \delta')}}{\varepsilon_1^0 e^{i\omega t}} = -\frac{\varepsilon_2^0 e^{-i\delta'}}{\varepsilon_1^0}$$
(4-5)

where $\varepsilon_2^0(\omega)$ is the amplitude of the lateral strain and δ' is the phase angle between $\varepsilon_1(t)$ and $\varepsilon_2(t)$.

Under a uniaxial, stress-controlled complex modulus test, the axial strain, $\varepsilon_1(t)$, lags behind the axial stress, $\sigma_1(t)$, with a phase lag δ . At the same time, the lateral strain, $\varepsilon_2(t)$, lags behind the axial strain, $\varepsilon_1(t)$, which already has a phage lag. Therefore, the lateral strain can be expressed as:

$$\varepsilon_{2}(t) = \varepsilon_{2}^{0} \cdot e^{i\{\omega t - \delta - \delta'\}} = \varepsilon_{2}^{*,p} \cdot e^{i(\omega t - \delta)} = \varepsilon_{2}^{*,t} \cdot e^{i\omega t}$$

$$\tag{4-6}$$

In the above equation, two complex amplitudes are introduced. First, $\varepsilon_2^{*,p}$ is the complex amplitude that contains only the phase lag between $\varepsilon_1(t)$ and $\varepsilon_2(t)$:

$$\varepsilon_2^{*,p} = \varepsilon_2^0 e^{-i\delta'} \tag{4-7}$$

whereas $\varepsilon_2^{*,t}$ is the complex amplitude that includes both phase angles:

$$\varepsilon_2^{*,t} = \varepsilon_2^{*,p} e^{-i\delta} = \varepsilon_2^0 e^{-i(\delta + \delta')} \tag{4-8}$$

Then, the definition of the complex Poisson's ratio, v^* , can be rewritten in terms of the complex strains as:

$$v^*(\omega) = -\frac{\varepsilon_2^{*,t}}{\varepsilon_1^*} = -\frac{\varepsilon_2^0 e^{-i\{\delta + \delta'\}}}{\varepsilon_1^0 e^{-i\delta}} = -\frac{\varepsilon_2^0 e^{-i\delta'}}{\varepsilon_1^0} = -\frac{\varepsilon_2^{*,p}}{\varepsilon_1^0}$$
(4-9)

It should be noted that the last term shown in Equation (4-9) is the same as the form of that shown in Equation (4-1). After substituting Equation (3-8) into the above equation for ε_1^* , the complex lateral strain can be described as a function of the complex compliance and complex Poisson's ratio as follows:

$$\varepsilon_2^{*,t}(\omega) = -v^*(\omega)\varepsilon_1^*(\omega) = -v^*(\omega)D^*(\omega)\sigma_1^0$$
(4-10)

4.1.3. Relationship Between Time and Frequency Dependent Poisson's Ratios

In order to find a relationship between v(t) and $v^*(\omega)$, a new integration variable $\tau' = t - \tau$ is substituted into Equation (4-2):

$$\varepsilon_{2}(t) = \int_{0}^{t} \nu(\tau') \frac{\partial \varepsilon_{1}(t - \tau')}{\partial \tau'} d\tau'$$
(4-11)

Since a stress term is not included in the above equation, it is more convenient to use the complex strain function, $\varepsilon_1^0 e^{i\omega t}$, than Equation (4-8) because the phase angle between the axial stress and strain is not included in this equation. According to Euler's formula, the complex strain function can be expressed as:

$$\varepsilon_1(t) = \varepsilon_1^0 e^{i\omega t} = \varepsilon_1^0 (\cos \omega t + i\sin \omega t)$$
(4-12)

or

$$\varepsilon_{1}(t-\tau') = \varepsilon_{1}^{0} e^{i\omega(t-\tau')} = \varepsilon_{1}^{0} e^{i\omega t} e^{-i\omega \tau'} = \varepsilon_{1}^{0} e^{i\omega t} (\cos \omega \tau' - i\sin \omega \tau')$$
(4-13)

Substituting the above strain into Equation (4-11) yields:

$$\varepsilon_{2}(t) = \int_{0}^{t} v(\tau') \frac{\partial}{\partial \tau'} \left[\varepsilon_{1}^{0} e^{i\omega t} \left(\cos \omega \tau' - i \sin \omega \tau' \right) \right] d\tau'$$
 (4-14)

The lateral strain, $\varepsilon_2(t)$, in the above equation is a result of an axial strain oscillation, $\varepsilon_1(t) = \varepsilon_1^0 e^{i\omega t}$, and can be expressed as the lateral complex strain function with only the phase angle between the two strains, that is:

$$\varepsilon_2(t) = \varepsilon_2^{*,p} e^{i\omega t} \tag{4-15}$$

Therefore, from Equations (4-14) and (4-15),

$$\varepsilon_{2}^{*,p}e^{i\omega t} = \int_{0}^{t} v(\tau') \frac{\partial}{\partial \tau'} \left[\varepsilon_{1}^{0} e^{i\omega t} (\cos \omega \tau' - i\sin \omega \tau') \right] d\tau'$$
 (4-16)

After canceling $e^{i\omega t}$ and dividing both sides of the above equation by ε_1^0 , the left-hand side of the equation is left with the complex Poisson's ratio due to Equation (4-9).

$$v^* = -\int_0^t v(\tau') \frac{\partial}{\partial \tau'} [(\cos \omega \tau' - i \sin \omega \tau')] d\tau'$$

$$= \omega \int_0^t v(\tau') \sin \omega \tau' d\tau' + i \omega \int_0^t v(\tau') \cos \omega \tau' d\tau'$$

$$= i \omega \left[\int_0^t v(\tau') \cos \omega \tau' d\tau' - i \int_0^t v(\tau') \sin \omega \tau' d\tau' \right]$$
(4-17)

After changing the upper limit to infinity:

$$v^* = i\omega \left[\int_0^\infty v(\tau') \cos \omega \tau' d\tau' - i \int_0^\infty v(\tau') \sin \omega \tau' d\tau' \right]$$

$$= i\omega \int_0^\infty v(\tau') \{\cos \omega \tau' - i \sin \omega \tau'\} d\tau'$$

$$= i\omega \int_0^\infty v(\tau') \cdot e^{-i\omega \tau'} d\tau'$$
(4-18)

The last equality in the above equation indicates that the relationship between the Poisson's ratio functions in the two domains is obtained as:

$$v^*(\omega) = i\omega \cdot \widehat{v}(s)|_{s=i\omega} \tag{4-19}$$

4.2. Extension of the Elastic-Viscoelastic Correspondence Principle

In the previous chapter, it was shown that for the uniaxial case, the viscoelastic constitutive equations can be obtained by replacing the elastic constant by its appropriate viscoelastic counterpart. Equation (4-4) indicates that in order to apply the elastic-viscoelastic correspondence principle for the multiaxial case, the elastic compliance, D, and the Poisson's ratio, v, should be replaced by $s\widehat{D}(s)$ and $s\widehat{v}(s)$, respectively. On the other hand, Equation (4-10) shows that the above elastic constants should be replaced by D^* and v^* in order to yield the viscoelastic constitutive relations in the frequency domain. For example, starting with the three-dimensional constitutive equation for an elastic material given as:

$$\varepsilon_{x} = D \cdot \left[\sigma_{x} - \nu \sigma_{y} - \nu \sigma_{z} \right]$$

$$\varepsilon_{y} = D \cdot \left[\sigma_{y} - \nu \sigma_{z} - \nu \sigma_{x} \right]$$

$$\varepsilon_{z} = D \cdot \left[\sigma_{z} - \nu \sigma_{x} - \nu \sigma_{y} \right]$$

$$(4-20)$$

The viscoelastic constitutive relation in the Laplace domain can be obtained as:

$$\widehat{\varepsilon}_{x}(s) = s\widehat{D}(s) \cdot \left[\widehat{\sigma}_{x}(s) - s\widehat{v}(s)\widehat{\sigma}_{y}(s) - s\widehat{v}(s)\widehat{\sigma}_{z}(s)\right]$$

$$\widehat{\varepsilon}_{y}(s) = s\widehat{D}(s) \cdot \left[\widehat{\sigma}_{y}(s) - s\widehat{v}(s)\widehat{\sigma}_{z}(s) - s\widehat{v}(s)\widehat{\sigma}_{x}(s)\right]$$

$$\widehat{\varepsilon}_{z}(s) = s\widehat{D}(s) \cdot \left[\widehat{\sigma}_{z}(s) - s\widehat{v}(s)\widehat{\sigma}_{x}(s) - s\widehat{v}(s)\widehat{\sigma}_{y}(s)\right]$$

$$(4-21)$$

Similarly, in the frequency domain, the following is obtained:

$$\varepsilon_{x} * (\omega) = D * (\omega) \cdot \left[\sigma_{x}^{0} - \upsilon * (\omega) \sigma_{y}^{0} - \upsilon * (\omega) \sigma_{z}^{0} \right]$$

$$\varepsilon_{y} * (\omega) = D * (\omega) \cdot \left[\sigma_{y}^{0} - \upsilon * (\omega) \sigma_{z}^{0} - \upsilon * (\omega) \sigma_{x}^{0} \right]$$

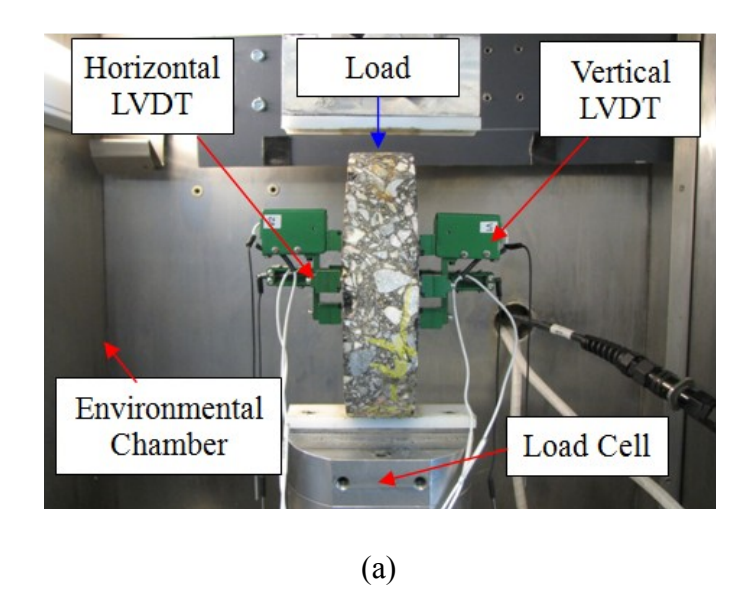
$$\varepsilon_{z} * (\omega) = D * (\omega) \cdot \left[\sigma_{z}^{0} - \upsilon * (\omega) \sigma_{x}^{0} - \upsilon * (\omega) \sigma_{y}^{0} \right]$$

$$(4-22)$$

4.3. Determining the Viscoelastic Property from the Indirect Tensile (IDT) Test

Although the uniaxial tension or compression test is desirable for testing of the materials, the problem associated with size requirements makes it difficult to perform the uniaxial test, especially on cored mixtures from the thin asphalt layers.

As an alternative to the uniaxial tests, the indirect tension test (Buttlar and Roque 1994, Zhang et al., 1997a, 1997b, and Kim et al., 2005), which is often called a Brazilian test, has been widely used for testing both laboratory-made and field-cored mixtures because the test requires relatively thin specimens. Therefore, the remainder of this chapter will be dedicated to developing a methodology for obtaining the viscoelastic properties from the IDT which is a biaxial test. This is critical because the viscoelastic property backcalculated from the FWD data will be compared to the IDT result from the pavement cores which will serve as a ground truth. A picture of the IDT set up and the IDT specimen geometry are shown in Figure 4-1.



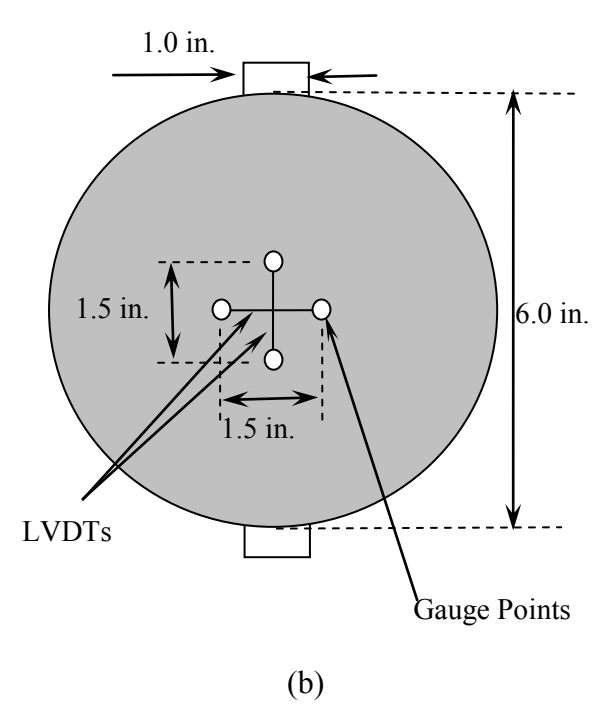


Figure 4-1. (a) Indirect tensile test setup and (b) specimen dimensions

4.3.1. Stress Distribution within an Indirect Tensile (IDT) Specimen

For an IDT specimen with radius R and thickness d subjected to a strip load of width $a = 2R \cdot \sin(\alpha)$ and magnitude P as shown in Figure 4-2 (Zhang et al., 1997a, 1997b, and Kim et al., 2005), the distributions of the tensile stress along the horizontal axis and the compressive stress along the vertical axis were given by Hondros (1959) under the assumption of plane stress conditions as:

$$\sigma_{x}(x,0) = \frac{2P}{\pi ad} \left[\frac{1 - (x/R)^{2} \sin 2\alpha}{1 + 2(x/R)^{2} \cos 2\alpha + (x/R)^{4}} - \tan^{-1} \left(\frac{1 - (x/R)^{2}}{1 + (x/R)^{2}} \tan \alpha \right) \right]$$

$$= \frac{2P}{\pi ad} m(x)$$
(4-23)

$$\sigma_{y}(0, y) = -\frac{2P}{\pi a d} \left[\frac{1 - (y/R)^{2} \sin 2\alpha}{1 - 2(y/R)^{2} \cos 2\alpha + (y/R)^{4}} + \tan^{-1} \left(\frac{1 + (y/R)^{2}}{1 - (y/R)^{2}} \tan \alpha \right) \right]$$

$$= -\frac{2P}{\pi a d} n(y)$$
(4-24)

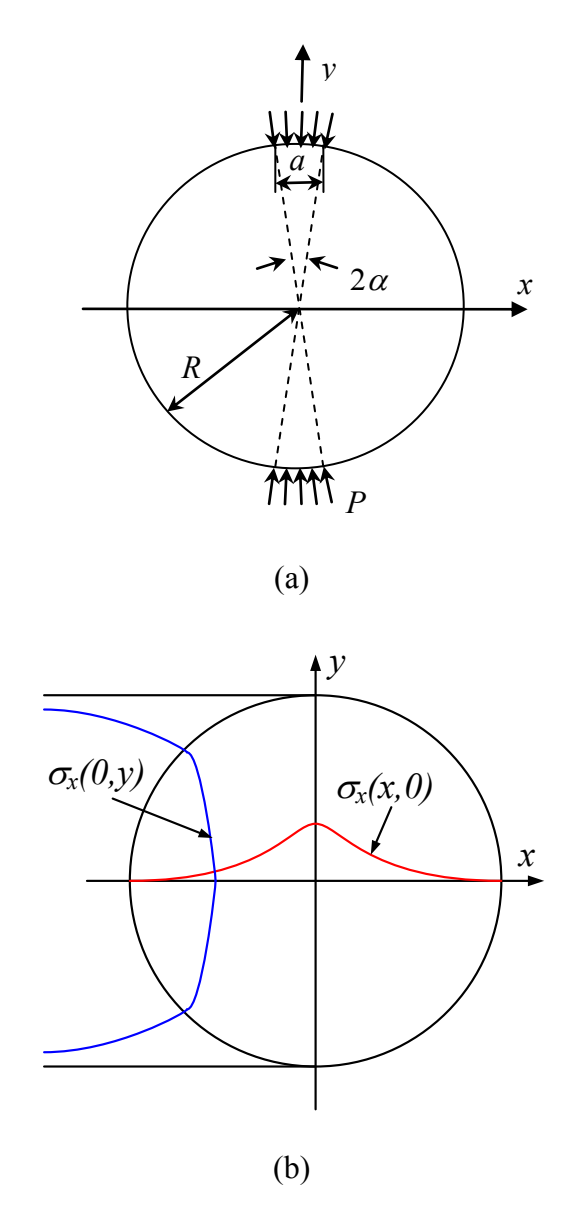


Figure 4-2 (a) Schematic illustration of the IDT test and (b) plane stress distributions

It would be ideal if the strain values could be measured at a point located at the center of the specimen, i.e., x = y = 0. The corresponding stresses then could be obtained easily as $\sigma_x(0,0)$ and $\sigma_y(0,0)$ from the above equations; however, the strain values are obtained based on the displacements measured by the strain gauges with a length of l and are better represented by the

average or the mean of the strain distributions between the gauge points. Therefore, the average stresses calculated over the gauge length in conjunction with the measured strains were used. The average stresses are calculated as:

$$\sigma_{x,avg} = \frac{2P}{\pi ad} \cdot \frac{1}{l} \int_{-l/2}^{l/2} m(x) dx$$
 (4-25)

$$\sigma_{y,avg} = -\frac{2P}{\pi ad} \cdot \frac{1}{l} \int_{-l/2}^{l/2} n(y) dy$$
(4-26)

For an IDT creep test, the load P in the above equations can be substituted with $P = P(t) = P^0H(t)$, where P^0 is the magnitude of the creep load, and H(t) is the Heaviside step function. Substituting this into Equations (4-25) and (4-26), and taking the Laplace transform yields:

$$\widehat{\sigma}_{x,avg}(s) = \frac{\sigma_x^0}{s} \tag{4-27}$$

$$\hat{\sigma}_{y,avg}(s) = -\frac{\sigma_y^0}{s} \tag{4-28}$$

where the magnitudes of the stresses σ_x^0 and σ_y^0 are:

$$\sigma_x^0 = \frac{2P^0}{\pi ad} \cdot \frac{1}{l} \int_{-l/2}^{l/2} m(x) dx$$
 (4-29)

$$\sigma_y^0 = \frac{2P^0}{\pi ad} \cdot \frac{1}{l} \int_{-l/2}^{l/2} n(y) dy$$
 (4-30)

Similarly, if the load is a sinusoidal oscillation with magnitude P^0 and angular frequency ω , then $P = P(t) = P^0 e^{i\omega t}$ and Equations (4-25) and (4-26) become:

$$\sigma_{x,avg}(t) = \sigma_x^0 \cdot e^{i\omega t} \tag{4-31}$$

$$\sigma_{y,avg}(t) = -\sigma_y^0 \cdot e^{i\omega t} \tag{4-32}$$

Another constant that is derived in this section is the ratio of the stress magnitudes. This ratio, β , will be used later to simplify the equations for the viscleoastic stress-strain relation significantly:

$$\beta = -\frac{\sigma_{y,avg}}{\sigma_{x,avg}} = \frac{\sigma_y^0}{\sigma_x^0} = \frac{\int_{l/2}^{l/2} n(y)dy}{\int_{l/2}^{l/2} m(x)dx}$$

$$(4-33)$$

With the above definition for β , the relationship between the two stresses can be written as:

$$\sigma_{v,avg} = -\beta \cdot \sigma_{x,avg} \tag{4-34}$$

For the remainder of the chapter, the subscript "avg" will be dropped from the above equation and, σ_x and σ_y will be used to represent the average stresses over the gauge length unless stated otherwise.

4.3.2. Indirect Tensile Creep Test

From Equation (4-21), the plane stress constitutive equations for a viscoelastic material with time-dependent Poisson's ratio can be written in the Laplace domain as:

$$\widehat{\varepsilon}_{x}(s) = s\,\widehat{D}(s) \cdot \left[\widehat{\sigma}_{x}(s) - s\,\widehat{v}(s)\widehat{\sigma}_{y}(s)\right] \tag{4-35}$$

$$\widehat{\varepsilon}_{\mathcal{V}}(s) = s\,\widehat{D}(s) \cdot \left[\widehat{\sigma}_{\mathcal{V}}(s) - s\,\widehat{\mathcal{V}}(s)\widehat{\sigma}_{\mathcal{X}}(s)\right] \tag{4-36}$$

After eliminating the term $s\hat{v}(s)$ from the above equations and reorganizing the variables, one can solve for an expression for the creep compliance in the Laplace domain. Upon simplifying the result using Equation (4-34), one arrives at:

$$\widehat{D}(s) = \frac{1}{s} \cdot \frac{\widehat{\varepsilon}_{x} + \beta \cdot \widehat{\varepsilon}_{y}}{\widehat{\sigma}_{x} + \beta \cdot \widehat{\sigma}_{y}}$$
 (4-37)

For an IDT creep test, the stresses in the Laplace domain were given in Equations (4-27) and (4-28). After substitution of these stresses, the denominator in the above equation simply reduces to a constant, that is:

$$\widehat{D}(s) = \frac{\widehat{\varepsilon}_x + \beta \cdot \widehat{\varepsilon}_y}{\sigma_x^0 - \beta \cdot \sigma_y^0} \tag{4-38}$$

Taking the inverse Laplace transform on the above equation results in the creep compliance in time domain:

$$D(t) = \frac{1}{\sigma_x^0 - \beta \cdot \sigma_y^0} \cdot \left\{ \varepsilon_x(t) + \beta \cdot \varepsilon_y(t) \right\}$$
 (4-39)

4.3.3. Indirect Tensile Complex Modulus Test

Equation (4-22) indicates that the plane stress constitutive equations for a viscoelastic material in the frequency domain can be written as:

$$\varepsilon_x^* = D^* \cdot \left[\sigma_x^0 - \nu^* \sigma_y^0 \right] \tag{4-40}$$

$$\varepsilon_y^* = D^* \cdot \left[\sigma_y^0 - v^* \sigma_x^0 \right] \tag{4-41}$$

Combining Equations (4-40) and (4-41) by eliminating v^* yields:

$$D^{*}(\omega) = \frac{\varepsilon_{x}^{*} + \beta \cdot \varepsilon_{y}^{*}}{\sigma_{x}^{0} + \beta \cdot \sigma_{y}^{0}}$$
(4-42)

The complex strain amplitudes in the numerator of the above equation can be expressed in a form shown in Equation (3-7) as:

$$\varepsilon_{x}^{*}(\omega) = \varepsilon_{x}^{0} \cdot e^{-i\delta_{x}} = \varepsilon_{x}^{0} \cdot (\cos(\delta_{x}) - i\sin(\delta_{x}))$$
(4-43)

$$\varepsilon_{y}^{*}(\omega) = \varepsilon_{y}^{0} \cdot e^{-i\delta_{y}} = \varepsilon_{y}^{0} \cdot \left(\cos(\delta_{y}) - i\sin(\delta_{y})\right) \tag{4-44}$$

where ε_x^0 and ε_y^0 are the horizontal and vertical strain amplitudes and δ_x and δ_y are the horizontal and vertical phase lags measured from the IDT test. However, through IDT experiments, Lee and Kim (2009) showed that the difference between the two phase lags δ_x and δ_y is negligible, that is, $\delta = \delta_x = \delta_y$. Substituting this into Equations (4-43) and (4-44), and the resulting equations into Equation (4-42) results in:

$$D^{*}(\omega) = \frac{\varepsilon_{x}^{0} + \beta \cdot \varepsilon_{y}^{0}}{\sigma_{y}^{0} + \beta \cdot \sigma_{y}^{0}} \cdot e^{-i\delta}$$
(4-45)

CHAPTER 5 - THEORETICAL DEVELOPMENT OF A TIME DOMAIN FORWARD SOLUTION

5.1. Governing Equations For Viscoelastic Wave Propagation

Similar to any other wave propagation problems, the proposed solution begins with the classical equation of motion for a continuous medium given as the following (Malvern, 1969):

$$\nabla \cdot \mathbf{\sigma} + \mathbf{b} = \rho \mathbf{\ddot{u}} \tag{5-1}$$

where σ is the stress tensor, **b** is the vector of body forces per unit volume, ρ is the mass density of the material, and **u** is the displacement vector. According to the theory of linear elasticity, the stress-strain relationship for a linear, homogenous, and isotropic material is obtained from the generalized Hooke's law:

$$\mathbf{\sigma} = \lambda t r(\mathbf{\varepsilon}) \mathbf{I} + 2\mu \mathbf{\varepsilon} \tag{5-2}$$

where ε is the strain tensor, λ and μ are the lamé constants, and \mathbf{I} is the identity tensor. The strain tensor in the above equation is related to the displacement vector according to the following:

$$\mathbf{\varepsilon} = \frac{1}{2} \left\{ \nabla \mathbf{u} + (\nabla \mathbf{u})^T \right\} \tag{5-3}$$

For a viscoelastic material such as an asphalt concrete mixture, the fundamental materials properties – in this case, the lamé constants – as well as the stresses and strains are time-dependent and hence, their relationship can be written as the following in reference to the theory of linear viscoelasticity (Schapery, 1974, Wineman, and Rajagopal, 2000, Christensen, 2003):

$$\mathbf{\sigma} = \lambda * tr(\mathbf{\varepsilon})\mathbf{I} + 2\mu * \mathbf{\varepsilon} \tag{5-4}$$

where the function $\alpha * \beta$ represents the well known Stieltjes convolution integral defined as:

$$\alpha * \beta = \int_{0}^{t} \alpha (t - \tau) \frac{\partial \beta(\tau)}{\partial \tau} d\tau$$
 (5-5)

It should be noted that the kinematic strain-displacement relationship shown in Equation (5-3) also applies to linear viscoelastic materials. The only difference from an elastic material is that the displacement and hence the strain are functions of not only the material (or spatial) coordinates but also time. Substituting Equations (5-3) and (5-4) into the equation of motion shown in Equation (5-1) and ignoring the body forces result in the following equation in terms of displacements:

$$(\lambda + \mu) * \nabla(\nabla \cdot \mathbf{u}) + \mu * \nabla^2 \mathbf{u} = \rho \ddot{\mathbf{u}}$$
 (5-6)

By means of the Helmholtz decomposition, the displacement vector in the above equation can be expressed in terms of potentials as follows:

$$\mathbf{u} = \nabla \Phi + \nabla \times \mathbf{H} \tag{5-7}$$

where Φ represent a scalar potential and \mathbf{H} is a vector potential whose divergence vanishes (i.e., $\nabla \cdot \mathbf{H} = \mathbf{0}$).

Similar to the spectral element solution provided by Al-Khoury et. al. (2001a), a cylindrical axisymmetric coordinate system shown in Figure 5-1 shall be employed herein. Then, the following equations are obtained for the potentials by substituting Equation (5-7) into Equation (5-6):

$$(\lambda + 2\mu) * \nabla^2 \Phi = (\lambda + 2\mu) * \left\{ \frac{\partial^2 \Phi}{\partial r^2} + \frac{1}{r} \frac{\partial \Phi}{\partial r} + \frac{\partial^2 \Phi}{\partial z^2} \right\} = \rho \frac{\partial^2 \Phi}{\partial t^2}$$
 (5-8)

$$\mu * \left(\nabla^2 H_{\theta} - \frac{H_{\theta}}{r^2} \right) = \mu * \left\{ \frac{\partial^2 H_{\theta}}{\partial r^2} + \frac{1}{r} \frac{\partial H_{\theta}}{\partial r} + \frac{\partial^2 H_{\theta}}{\partial z^2} - \frac{H_{\theta}}{r^2} \right\} = \rho \frac{\partial^2 H_{\theta}}{\partial t^2}$$
 (5-9)

where H_{θ} is the tangential and also the only component of **H** that does not vanish. By defining H_{θ} as:

$$H_{\theta} = -\frac{\partial \Psi}{\partial r} \tag{5-10}$$

it can be shown that the scalar potential Ψ satisfies the following wave equation. The proof can be obtained immediately if Equation (5-11) is differentiated with respect to r (Ewing et. al., 1957).

$$\mu * \nabla^2 \Psi = \mu * \left\{ \frac{\partial^2 \Psi}{\partial r^2} + \frac{1}{r} \frac{\partial \Psi}{\partial r} + \frac{\partial^2 \Psi}{\partial z^2} \right\} = \rho \frac{\partial^2 \Psi}{\partial t^2}$$
 (5-11)

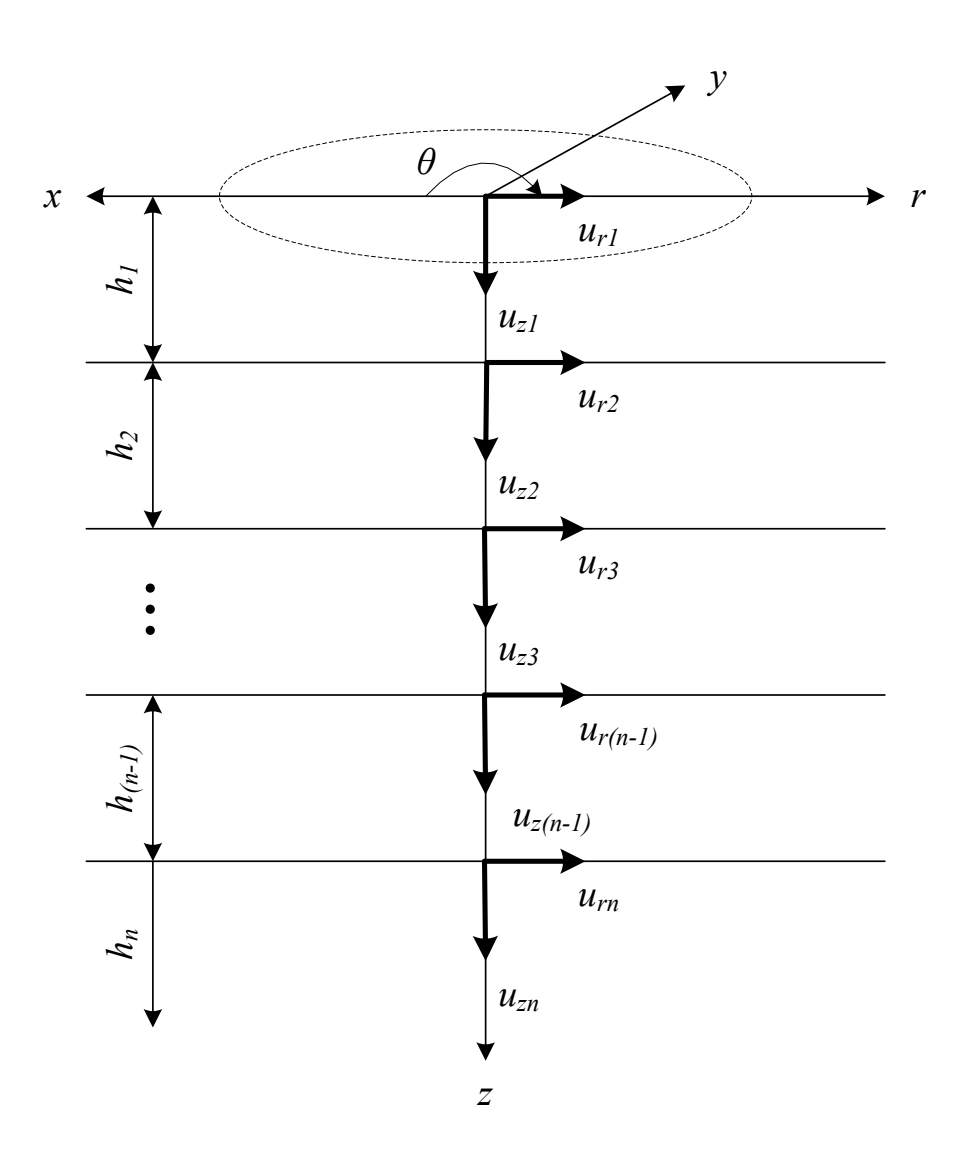


Figure 5-1 Coordinate System for Axisymmetric Layers on a Halfspace

Equations (5-8) and (5-11) are the wave equations that govern the axisymmetric wave motion in a continuous, linear viscoelastic medium. It is also worthwhile to note that if the lamé constants, λ and μ , were independent of time (i.e., the material is linear elastic), then the convolution integral in Equations (5-8) and (5-11) reduce to an arithmetic multiplication and these 2 equations become the well known axisymmetric wave equations for a linear elastic material (Ewing et. al., 1957, Graff, 1991).

Another immediate consequence of adopting the axisymmetric coordinate system is that the displacement component in the tangential direction, u_{θ} vanishes (Graff, 1991). The remaining deflections can be written as the following in terms of the scalar potentials Φ and Ψ :

$$u_r = \frac{\partial \Phi}{\partial r} + \frac{\partial^2 \Psi}{\partial r \partial z} \tag{5-12}$$

$$u_z = \frac{\partial \Phi}{\partial z} - \frac{\partial^2 \Psi}{\partial r^2} - \frac{1}{r} \frac{\partial \Psi}{\partial r}$$
 (5-13)

And the stresses can be written as:

$$\sigma_{rz} = \mu * \frac{\partial}{\partial r} \left\{ 2 \frac{\partial \Phi}{\partial z} - \frac{\partial^2 \Psi}{\partial r^2} - \frac{1}{r} \frac{\partial \Psi}{\partial r} + \frac{\partial^2 \Psi}{\partial z^2} \right\}$$
 (5-14)

$$\sigma_z = \lambda * \left\{ \frac{\partial^2 \Phi}{\partial r^2} + \frac{1}{r} \frac{\partial \Phi}{\partial r} + \frac{\partial^2 \Phi}{\partial z^2} \right\} + 2\mu * \frac{\partial}{\partial z} \left\{ \frac{\partial \Phi}{\partial z} - \frac{\partial^2 \Psi}{\partial r^2} - \frac{1}{r} \frac{\partial \Psi}{\partial r} \right\}$$
 (5-15)

5.2. Solutions For The Wave Equations In The Laplace-Hankel Domain

The solution to the wave equations presented above can be worked more conveniently by utilizing the integral transforms. Taking the Laplace transform of Equation (5-8) results in:

$$s(\hat{\lambda} + 2\hat{\mu}) \cdot \left\{ \frac{\partial^2 \hat{\Phi}}{\partial r^2} + \frac{1}{r} \frac{\partial \hat{\Phi}}{\partial r} + \frac{\partial^2 \hat{\Phi}}{\partial z^2} \right\} = \rho s^2 \hat{\Phi}$$
 (5-16)

where s is the Laplace variable and $\hat{f}(s) = \int_0^\infty e^{-st} f(t) dt$ is the Laplace transform of a function f(t). Then, taking the Hankel Transform (also known as the Fourier-Bessel transform) of order zero defined as $\bar{f}(k) = \int_0^\infty \hat{f}(r) J_0(kr) r dr$ on Equation (5-16), one finds:

$$s(\widehat{\lambda} + 2\widehat{\mu}) \cdot \left\{ \frac{\partial^2 \overline{\Phi}}{\partial z^2} - k^2 \overline{\Phi} \right\} = \rho s^2 \overline{\Phi}$$
 (5-17)

After a simple rearrangement of the terms, the above equation can be written as:

$$\frac{\partial^2 \overline{\Phi}}{\partial z^2} - \left(k^2 + \frac{s}{\overline{c_1}^2}\right) \overline{\Phi} = 0 \tag{5-18}$$

where,

$$\widehat{c}_1^2 = \frac{\widehat{\lambda} + 2\widehat{\mu}}{\rho} \tag{5-19}$$

From Equation (5-18), the solution for the Laplace-Hankel transformed potential function, $\overline{\Phi}$, is obtained as the following, after dropping the term that develops an unbounded result, that is the wave that propagates in the negative z direction (Ewing et. al., 1957, Graff, 1991):

$$\overline{\Phi} = Ae^{-z\sqrt{k^2 + \frac{s}{\hat{c}_1^2}}} = Ae^{-zf(k,s)}$$
 (5-20)

where A is an arbitrary constant.

By following the same mathematical steps shown above, Equation (5-11) can be rewritten as:

$$\frac{\partial^2 \overline{\Psi}}{\partial z^2} - \left(k^2 + \frac{s}{\widehat{c}_2^2}\right) \overline{\Psi} = 0 \tag{5-21}$$

where,

$$\hat{c}_2^2 = \frac{\hat{\mu}}{\rho} \tag{5-22}$$

Again, after dropping the term leading to unbounded results, the solution for the transformed potential, $\overline{\Psi}$, is obtained as:

$$\overline{\Psi} = Ce^{-z\sqrt{k^2 + \frac{s}{\hat{c}_2^2}}} = Ce^{-zg(k,s)}$$
 (5-23)

where *C* is also an arbitrary constant.

In order to make use of the solutions obtained above for the transformed potentials, it is also necessary to acquire the equations for the displacements and the stresses in the transformed domain. While taking the Laplace transform on the displacements and the stresses is straight forward, additional attention is needed in taking the Hankel transform due to the spatial symmetry supplied by the cylindrical coordinate system adopted for the solution. Referring back to Figure 1, one finds that the displacement at any point on the z-axis (i.e., when r = 0) is only allowed to occur in the z-direction (i.e., $u_z \neq 0$ when r = 0) but is confined in the r-direction (i.e., $u_r = 0$ when r = 0), unless the axisymmetric assumption is to be violated. Due to these physical characteristics of the axisymmetric displacements, Hankel transforms of different orders need to be applied to u_r and u_z .

Figure 5-2 shows the first few cycles of the Bessel functions of the first kind, and of orders zero (J_0) and one (J_1) that make up the kernels of the Hankel transform. The primary difference between the two Bessel functions shown in the figure is that while the Bessel function of order zero (J_0) has a nonzero value at r = 0, the Bessel function of order one (J_1) is equal to zero when r = 0. This implies that the Hankel transform of order zero whose kernel is composed of J_0 is appropriate for transforming the functions that exhibit nonzero values at the origin, whereas

the Hankel transform of order one whose kernel is made up of J_1 is more appropriate for transforming the functions that have zero values at r=0. Therefore, the appropriate Hankel transformed that should be applied to u_r and u_z are of orders one and zero, respectively. Taking the Laplace and the respective Hankel Transforms on the displacements, u_r and u_z , shown in Equations (5-12) and (5-13) results in:

$$\overline{u}_r = -k\overline{\Phi} - k\frac{\partial\overline{\Psi}}{\partial z} \tag{5-24}$$

$$\overline{u}_z = \frac{\partial \overline{\Phi}}{\partial z} + k^2 \overline{\Psi} \tag{5-25}$$

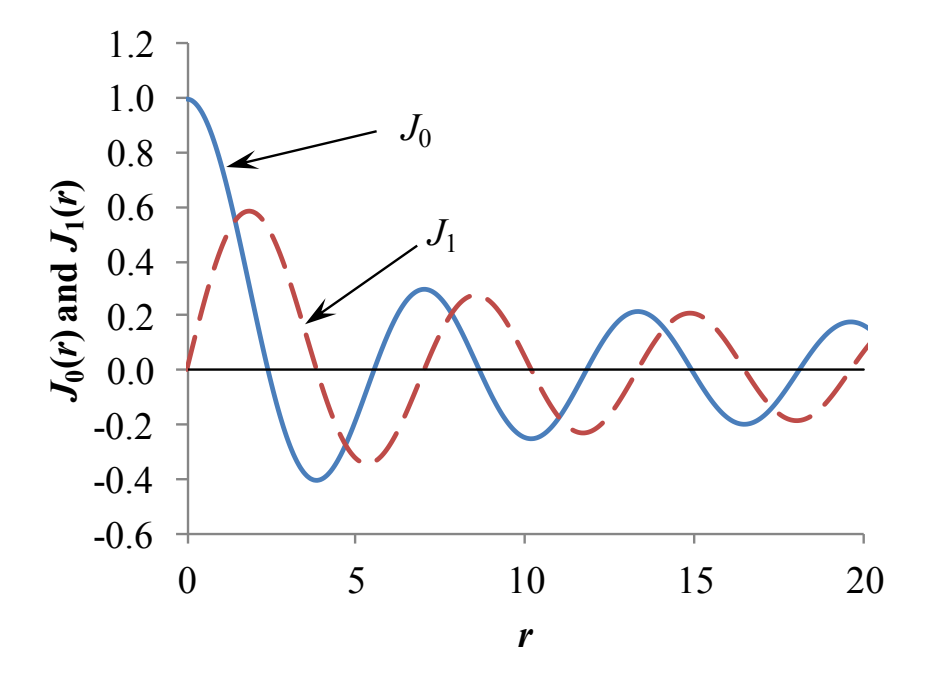


Figure 5-2 Bessel Functions of the First Kind

It should be noted that although the Hankel transform of order one was used to transform u_r shown in Equation (5-12), the Hankel transform of the potentials shown in Equation (5-24) is still of order zero. This is a consequence of the partial derivative with respect to r that is present in both terms of the right hand side of Equation (5-12) and the following property of the Hankel transform which associates the first order transform of a function's derivative to the zero order transform of the original function (Graff, 1991, Sneddon, 1995):

$$\int_{0}^{\infty} \frac{\partial \widehat{f}(r)}{\partial r} J_{1}(kr) r dr = -k \int_{0}^{\infty} \widehat{f}(r) J_{0}(kr) r dr = -k \cdot \overline{f}(k)$$
 (5-26)

Subsequently, the Laplace-Hankel transforms need to be carried out on the relevant stresses. Due to the same mathematical arguments presented above for the displacements, the Hankel transform of orders one and zero should be applied respectively on σ_{rz} and σ_z to allow for a solution that is compatible with the axisymmetric coordinate system chosen for the solution. After simplifying, these equations are obtained as:

$$\sigma_{rz} = -sk\hat{\mu} \left\{ 2\frac{\partial \overline{\Phi}}{\partial z} + 2\frac{\partial^2 \overline{\Psi}}{\partial z^2} - \frac{s}{\hat{c}_2^2} \right\}$$

$$= -sk\hat{\mu} \left\{ 2\frac{\partial \overline{\Phi}}{\partial z} + 2k^2 \overline{\Psi} + \frac{s}{\hat{c}_2^2} \overline{\Psi} \right\}$$
(5-27)

$$\begin{split} \overline{\sigma}_z &= s\widehat{\lambda} \cdot \left\{ -k^2 \overline{\Phi} + \frac{\partial^2 \overline{\Phi}}{\partial z^2} \right\} + 2s\widehat{\mu} \frac{\partial}{\partial z} \left\{ \frac{\partial \overline{\Phi}}{\partial z} + k^2 \overline{\Psi} \right\} \\ &= \widehat{\mu} \frac{s^2}{\widehat{c}_2^2} \overline{\Phi} + 2sk^2 \widehat{\mu} \left(\overline{\Phi} + \frac{\partial \overline{\Psi}}{\partial z} \right) \end{split} \tag{5-28}$$

5.3. Formulation of the Stiffness Matrices for the Layer Elements

The solutions presented above for the scalar potentials in the transformed domain are not readily applicable for a multi layered system such as the one shown in Figure 5-1. In order to allow for the analysis of a layered system such as an asphalt pavement, it is necessary to develop the formulations for the layer elements of which the underlying concept origins from the method of Finite Element Analysis (FEA). In this section, two types of layer elements are developed – a 2 noded element for a layer with a finite thickness (e.g., the top layer in Figure 5-1) and a 1 noded element for simulation of a semi-infinite halfspace (e.g., the bottom layer in Figure 5-1).

5.3.1. Two Noded Element for a Layer with a Finite Thickness

The solutions for the scalar potentials shown in Equations (5-20) and (5-23) only account for the incident waves that propagate from the upper boundary of a layer in the direction of the positive z-axis, i.e., downward direction in Figure 1. However, a layer with a finite thickness also encompasses the waves that reflect from the lower boundary and propagate in the direction of the negative z-axis. To account for these reflected waves, an additional term must be added to each of the potentials, which results in the following equations:

$$\overline{\Phi} = Ae^{-zf} + Be^{-(h-z)f} \tag{5-29}$$

$$\overline{\Psi} = Ce^{-zg} + De^{-(h-z)g} \tag{5-30}$$

where B and D are arbitrary constants and h is the layer thickness. Substituting the above equations into Equations (5-24) and (5-25) results in the following equations for the displacements within a two noded element:

$$\bar{u}_r = -Ake^{-zf} - Bke^{-(h-z)f} - Ckge^{-zg} - Dkge^{-(h-z)g}$$
 (5-31)

$$\overline{u}_z = -Afe^{-zf} + Bfe^{-(h-z)f} + Ck^2e^{-zg} + Dk^2e^{-(h-z)g}$$
 (5-32)

For the formulation of a layer element, the displacements at the upper and lower boundaries need to be extracted from the above equations. The radial and the vertical displacements at the upper boundary, denoted respectively as \bar{u}_{r1} and \bar{u}_{z1} , can be obtained by substituting z=0 in the above equations. Similarly, the displacements at the lower boundary (\bar{u}_{r2} and \bar{u}_{z2}) are acquired by substituting z=h. In matrix form, the resulting equations for the displacements can be written as:

$$\begin{cases}
\overline{u}_{r1} \\
\overline{u}_{z1} \\
\overline{u}_{r2} \\
\overline{u}_{z2}
\end{cases} = \begin{bmatrix}
-k & -ke^{-hf} & kg & -kge^{-hg} \\
-f & fe^{-hf} & k^2 & k^2e^{-hg} \\
-ke^{-hf} & -k & kge^{-hg} & -kg \\
-fe^{-hf} & f & k^2e^{-hg} & k^2
\end{bmatrix} \begin{bmatrix} A \\ B \\ C \\ D \end{bmatrix} = \mathbf{S_1} \cdot \begin{bmatrix} A \\ B \\ C \\ D \end{bmatrix} \tag{5-33}$$

It is also necessary to obtain the equations for the stresses. By substituting Equations (5-29) and (5-30) into Equations (5-27) and (5-28), one arrives at the following equations:

$$\overline{\sigma}_{rz} = -s\widehat{\mu}k \left\{ -2Afe^{-zf} + 2Bfe^{-(h-z)f} + CKe^{-zg} + DKe^{-(h-z)g} \right\}$$
 (5-34)

$$\overline{\sigma}_z = s\widehat{\mu} \left\{ AKe^{-zf} + BKe^{-(h-z)f} - 2Ck^2ge^{-zg} + 2Dk^2ge^{-(h-z)g} \right\}$$
 (5-35)

where,

$$K = 2k^2 + \frac{s}{\hat{c}_2^2} \tag{5-36}$$

Again, the stresses at the upper boundary ($\bar{\sigma}_{rz1}$ and $\bar{\sigma}_{z1}$) are obtained by substituting z=0 in Equations (5-34) and (5-35), while those at the lower boundary ($\bar{\sigma}_{rz2}$ and $\bar{\sigma}_{z2}$) are found by substituting z=h, all of which can be summarized in a matrix form as follows:

$$\begin{bmatrix}
\bar{\sigma}_{rz1} \\
\bar{\sigma}_{z1} \\
\bar{\sigma}_{rz2} \\
\bar{\sigma}_{z2}
\end{bmatrix} = s\hat{\mu} \cdot \begin{bmatrix}
2f & -2fe^{-hf} & -K & -Ke^{-hg} \\
K & Ke^{-hf} & -2k^{2}g & 2k^{2}ge^{-hg} \\
Ke^{-hf} & -2f & -Ke^{-hg} & -K \\
Ke^{-hf} & K & -2k^{2}ge^{-hg} & 2k^{2}g
\end{bmatrix} \begin{bmatrix}
A \\
B \\
C \\
D
\end{bmatrix} = s\hat{\mu} \cdot \mathbf{S}_{2} \cdot \begin{bmatrix}
A \\
B \\
C \\
D
\end{bmatrix}$$
(5-37)

Combining Equations (5-33) and (5-37) by eliminating the vector of arbitrary constants, the stresses can be expressed in terms of the displacements as:

$$\begin{cases}
\overline{\sigma}_{rz1} \\
\overline{\sigma}_{z1} \\
\overline{\sigma}_{rz2} \\
\overline{\sigma}_{z2}
\end{cases} = s\widehat{\mu} \cdot \mathbf{S}_{2} \cdot \mathbf{S}_{1}^{-1} \cdot \begin{cases}
\overline{u}_{r1} \\
\overline{u}_{z1} \\
\overline{u}_{r2} \\
\overline{u}_{z2}
\end{cases}$$
(5-38)

where S_1 and S_2 are the 4 by 4 matrices defined in Equations (5-33) and (5-37), respectively. According to the concepts of FEA, the stiffness matrix of an element defines the relationship between the displacement vector and the boundary traction vector. Owing to the Cauchy stress principle, the boundary tractions are obtained by taking the dot product between the stress tensor and a unit vector directed along the outward normal of the boundary. Calculating these tractions at the upper and the lower boundaries of the element and reorganizing them in a vector form results in the following relationship between the tractions, stresses, and displacements:

$$\begin{bmatrix}
\overline{T}_{r1} \\
\overline{T}_{z1} \\
\overline{T}_{r2} \\
\overline{T}_{r2} \\
\overline{T}_{z2}
\end{bmatrix} = \begin{bmatrix}
-\overline{\sigma}_{rz1} \\
-\overline{\sigma}_{z1} \\
\overline{\sigma}_{rz2} \\
\overline{\sigma}_{z2}
\end{bmatrix} = \mathbf{S}_{2-\mathbf{noded}} \cdot \begin{bmatrix}
\overline{u}_{r1} \\
\overline{u}_{z1} \\
\overline{u}_{r2} \\
\overline{u}_{r2}
\end{bmatrix}$$
(5-39)

From the above equation, it is seen that the 4 by 4 matrix $S_{2-noded}$ is the stiffness matrix of the 2 noded layer element which is calculated as:

$$\mathbf{S}_{2-\mathbf{noded}} = s\hat{\mu} \cdot \mathbf{N} \cdot \mathbf{S}_2 \cdot \mathbf{S}_1^{-1}$$
 (5-40)

where

$$\mathbf{N} = \begin{bmatrix} -1 & 0 & 0 & 0 \\ 0 & -1 & 0 & 0 \\ 0 & 0 & 1 & 0 \\ 0 & 0 & 0 & 1 \end{bmatrix}$$
 (5-41)

5.3.2. One Noded Semi-Infinite Element

The axisymmetric one noded element was schematically shown as the bottom layer in Figure 5-1. As shown in the figure and as its name implies, the one noded element only has a single boundary at the top of the layer and extends infinitely in all other directions. As a consequence, the waves in this element are only allowed to propagate away from the upper boundary (which is also the only boundary) without any waves reflecting back. Therefore, the solutions for the scalar potentials shown in Equations (5-20) and (5-23) can be used without any modifications. Substituting these two equations into Equations (5-24) and (5-25) results in the following for the displacements:

$$\overline{u}_r = -Ake^{-zf} - Ckge^{-zg} \tag{5-42}$$

$$\overline{u}_z = -Afe^{-zf} + Ck^2e^{-zg} \tag{5-43}$$

The displacements at the boundary are obtained by substituting z = 0 in the above equations and can be written as the following in matrix form:

Again, the equations for the shear and normal stresses are obtained by substituting the potentials (Equations (5-20) and (5-23)) into Equations (5-27) and (5-28), respectively:

$$\overline{\sigma}_{rz} = -s\widehat{\mu} \left\{ -2Akfe^{-zf} + Ck\left(k^2 + g^2\right)e^{-zg} \right\}$$
 (5-45)

$$\overline{\sigma}_z = s\widehat{\mu} \left\{ A(k^2 + g^2)e^{-zf} - 2Ck^2ge^{-zg} \right\}$$
 (5-46)

Substituting z = 0 in Equations (5-45) and (5-46) results in the stresses at the boundary:

$$\begin{cases}
\overline{\sigma}_{r1} \\
\overline{\sigma}_{z1}
\end{cases} = s\hat{\mu} \cdot \begin{bmatrix} 2kf & -k(k^2 + g^2) \\ (k^2 + g^2) & -2k^2g \end{bmatrix} \begin{bmatrix} A \\ C \end{bmatrix} = s\hat{\mu} \cdot \mathbf{S_4} \begin{Bmatrix} A \\ C \end{Bmatrix}$$
(5-47)

From Equations (5-44) and (5-47), the following relationship is attained between the stresses and the displacements:

$$\left\{ \begin{array}{l} \overline{\sigma}_{r21} \\ \overline{\sigma}_{z1} \end{array} \right\} = s\widehat{\mu} \cdot \mathbf{S_4} \cdot \mathbf{S_3}^{-1} \cdot \left\{ \begin{array}{l} \overline{u}_{r1} \\ \overline{u}_{z1} \end{array} \right\} \tag{5-48}$$

where S_3 and S_4 were defined in Equations (5-44) and (5-47), respectively. By applying the Cauchy stress principle, the following relationship is achieved between the tractions, stresses, and displacements:

$$\begin{cases}
\overline{T}_{r1} \\
\overline{T}_{z1}
\end{cases} = \begin{cases}
-\overline{\sigma}_{rz1} \\
-\overline{\sigma}_{z1}
\end{cases} = \mathbf{S}_{1-\mathbf{noded}} \cdot \begin{cases}
\overline{u}_{r1} \\
\overline{u}_{z1}
\end{cases}$$
(5-49)

where the stiffness matrix for the one noded element can be written in terms of the previously defined variables as:

$$\mathbf{S}_{1-\mathbf{noded}} = -s\hat{\mu} \cdot \mathbf{S}_3 \cdot \mathbf{S}_4^{-1} \tag{5-50}$$

5.4. Incorporating Elastic And Viscoelastic Layer Properties

For a homogenous, isotropic, elastic material whose properties are independent of time, the relationship between the elastic modulus, E, and the lamé constant, μ , is given by the theory of linear elasticity as:

$$\mu = \frac{E}{2(1+\nu)} \tag{5-51}$$

Because the parameters in the above equation are not functions of time, the Laplace transform of the above equation is simply obtained as:

$$\hat{\mu}(s) = \frac{\mu}{s} = \frac{E}{2(1+\nu)} \cdot \frac{1}{s}$$
 (5-52)

However, as it was noted by the pioneer of the spectral element method for layered media (Rizzi, 1989), it is advantageous to add a small amount of damping to the lamé constant, μ , as no realistic material is purely elastic. Following Rizzi (1989), this artificial damping can be added to the above lamé constant as:

$$\widehat{\mu}(s) = \widehat{\mu}(s) \cdot (1 + \zeta \cdot s) \tag{5-53}$$

where ζ is a damping constant. To simulate the wave propagation through an elastic layer, the above simple equation can be substituted into the equations for the layer elements presented earlier.

To incorporate the viscoelastic material effects into the solution derived in the previous sections, it is necessary to adopt a simple function that is capable of representing the fundamental property of a viscoelastic material analytically. In addition, because all of the time-dependent variables including stresses, displacements, and material properties (i.e., lamé constants) were transformed into the Laplace domain, it is preferable to choose a function that is easily transformable into the Laplace domain. Among the analytical functions described in Chapter 3, the generalized power function has been selected because it still maintains a simple form while representing the viscoelastic property effectively. Again, this function is expressed as:

$$D(t) = D_0 + D_1 \cdot t^m \tag{5-54}$$

where D_0 , D_1 , and m are the power function parameters. Taking the Laplace transform on the above equation results in:

$$\widehat{D}(s) = \frac{D_0 s^m + D_1 \Gamma(m+1)}{s^{m+1}}$$
 (5-55)

where $\Gamma(m)$ is the gamma function. By substituting Equation (5-55) into Equation (3-16) and rearranging, one obtains the following equation for the uniaxial relaxation modulus in the Laplace domain:

$$\hat{E}(s) = \frac{1}{s^2 \hat{D}(s)} = \frac{s^{m-1}}{D_0 s^m + D_1 \Gamma(m+1)}$$
 (5-56)

As it was mentioned in Chapter 4, the Poisson's ratio of a viscoelastic material is also time dependent. However, the Poisson's ratio has typically been assumed to be a time-independent constant in past literatures (Huang, 2004). In addition, Lee and Kim (2009) showed that assuming a reasonable constant value for the Poisson's ratio still results in accurate viscoelastic responses. The assumption of a constant Poisson's ratio implies that the time dependent behavior of a viscoelastic material in shear or bulk is identical to the behavior in uniaxial mode, and simplifies the solution significantly (Kim et. al., 2010). With this assumption, the relationship between the viscoelastic lamé constant and the uniaxial relaxation modulus shown in Equation (5-56) is found to be the following:

$$\widehat{\mu}(s) = \frac{\widehat{E}(s)}{2(1+\nu)} = \frac{s^{m-1}}{2 \cdot (1+\nu) \cdot \left\{ D_0 s^m + D_1 \Gamma(m+1) \right\}}$$
(5-57)

5.5. Construction Of The Global Stiffness Matrix

After the stiffness matrices have been obtained for all the layers that make up the structure, the global stiffness matrix may be constructed in the same way as the traditional FEA methods (Cook et. al., 2001). In-depth explanation on the concept of the FEA as well as the relationship between the element and the global stiffness matrices is beyond the scope of this paper. Hence, it will not be explained herein and interested readers are referred to a variety of textbooks available on this subject. In this paper, only the generic conceptual schematics will be outlined and the discussion will be kept to a minimal for conciseness of the manuscript. Figure 5-3 shows the schematics of the global stiffness matrices for the two types of layered structures that are most widely adopted for modeling a pavement system.

Figure 5-3(a) shows how the global stiffness matrix is constructed for a layered system resting on a halfspace. As mentioned, this pavement model is capable of dissipating the energy geometrically through the one noded halfspace and is generally used for simulating the FWD time histories that do not show free vibration at the end of the loading. On the other hand, Figure 5-3(b) shows the global stiffness matrix that can be used for a layered system sitting on a stiff bedrock at shallow depth. In general, the bedrock in such a model is generally assumed to have an infinite stiffness, not allowing any displacements to occur within the layer. This implies that

the wave energy is trapped between the pavement surface and the top of bedrock, which may induce free vibration in the layered system at the end of the loading.

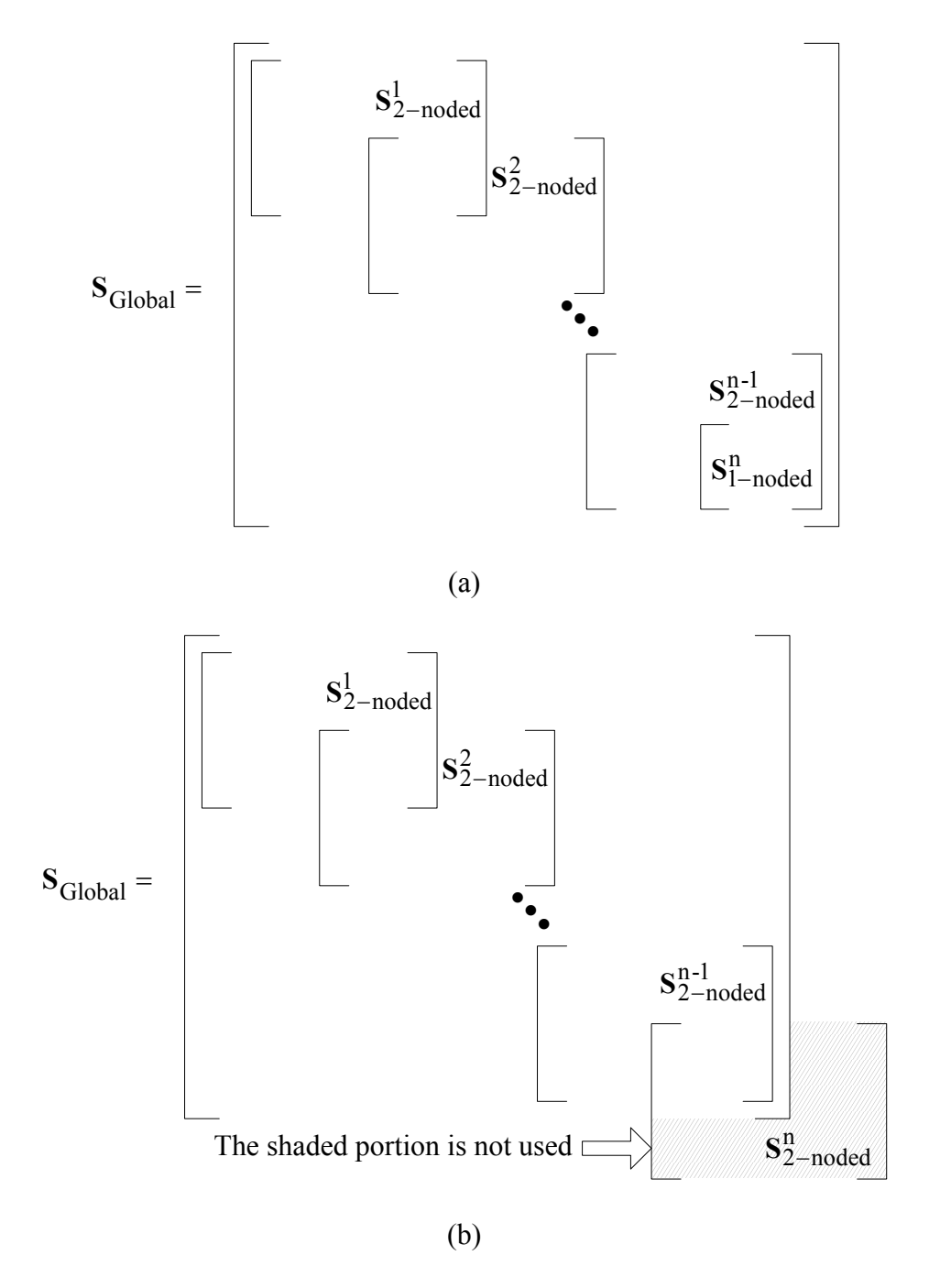


Figure 5-3 Construction of the Global Stiffness Matrix for Structures (a) with and (b) without a halfspace

Upon constructing the global stiffness matrix, the displacements at the system nodes can be found from the following equation:

$$\overline{\mathbf{U}} = \mathbf{S}_{\text{Global}}^{-1} \cdot \overline{\mathbf{P}} \tag{5-58}$$

where,

$$\overline{\mathbf{U}} = \left\{ \overline{U}_{r1} \quad \overline{U}_{z1} \quad \dots \quad \overline{U}_{ri} \quad \overline{U}_{zi} \quad \dots \quad \overline{U}_{rn} \quad \overline{U}_{zn} \right\}' \tag{5-59}$$

is a vector of system displacements to be calculated in global coordinates with \overline{U}_{ri} and \overline{U}_{zi} being the radial and vertical displacements at the i^{th} node from the top, respectively. Similarly,

$$\overline{\mathbf{P}} = \left\{ \overline{P}_{r1} \quad \overline{P}_{z1} \quad \dots \quad \overline{P}_{ri} \quad \overline{P}_{zi} \quad \dots \quad \overline{P}_{rn} \quad \overline{P}_{zn} \right\}'$$
 (5-60)

is a nodal force vector in global coordinates, with the radial and vertical forces at the i^{th} node denoted as \overline{P}_{ri} and \overline{P}_{zi} , respectively. The nodal forces in this vector should be obtained from the boundary conditions as will be presented in the next section.

5.6. Boundary Conditions for a Circular Unit Impulse Loading at the Ground Surface

For the problem in hand where the loading is induced by an impact of a falling weight at the ground surface, all components of $\overline{\mathbf{P}}$ in Equation (5-60) vanish except for \overline{P}_{z1} . In other words, the only external load applied to the system is in the vertical direction at the top node (node 1). In this paper, this surface force will also be in the form of a unit impulse load acting over a circular area, for the reasons to be explained in subsequent sections of the paper. In the physical time and spatial domain, this boundary condition is mathematically expressed as the following:

$$P_{z1}(r,t) = R(r) \cdot \delta(t) \tag{5-61}$$

where $\delta(t)$ is the dirac delta function for the impulse loading and,

$$R(r) = \begin{cases} 1 & , 0 < r \le a \\ 0 & , r > a \end{cases}$$
 (5-62)

where a is the radius of the circular loaded area. However, it should be noted that the stiffness matrices were previously derived in the Laplace-Hankel domain rather than the physical domain. As such, it is also necessary to convert the above boundary condition into the one in the transformed domain. Because the Laplace transform of $\delta(t)$ is equal to 1, taking the Laplace-Hankel transforms on Equation (5-61) simply results in the following equation:

$$\overline{P}_{z1}(k,s) = \frac{a}{k} J_1(ka) \tag{5-63}$$

5.7. Inversion Of Laplace And Hankel Transforms

As mentioned, the displacements at all nodes of the system can be obtained through Equation (5-58) from the global stiffness matrix and the force boundary condition described in the previous sections. It is noted again that the displacements obtained in this manner are in the Laplace-Hankel domain and need to be inverse transformed back to the physical domain. However, it has been shown that even for an elastic halfspace (which simply has a single boundary) subjected to a point load, the closed form inversion of the Laplace-Hankel transformed displacement is rather complicated and is close to impossible for a generalized problem (Graff, 1991). Therefore, the closed form inversion of the displacements obtained from Equation (5-58) is not even attempted due to the mathematical complexity arising from the viscoelastic material behavior and the wave propagation phenomenon. Instead, the inversion will be carried out numerically for both the Laplace and Hankel transforms.

5.8. Numerical Inversion of the Hankel Transform

As it was mentioned earlier, Hankel transforms of orders zero and one were used to transform the vertical and radial displacements, respectively. Therefore, the inverse Hankel transform of respective orders must be carried out for the two displacements. In this paper, the numerical integration scheme will be outlined for the vertical displacement (i.e, the inverse Hankel transform of order zero). The inverse transform of the radial displacement can also be evaluated in a similar manner.

The closed form equation for the inverse Hankel transform of the vertical displacement at node *i* is given as:

$$\widehat{U}_{zi}(r) = \int_{0}^{\infty} \overline{U}_{zi}(k) J_0(kr) k dk$$
 (5-64)

The above integral can also be written as a series of integrals:

$$\widehat{U}_{zi}(r) = \int_{b_1}^{b_2} \overline{U}_{zi}(k) J_0(kr) k dk + \int_{b_2}^{b_3} \overline{U}_{zi}(k) J_0(kr) k dk + \dots + \int_{b_n}^{b_{n+1}} \overline{U}_{zi}(k) J_0(kr) k dk + \dots$$
(5-65)

Then, each integral in the right hand side of Equation (5-65) needs to be evaluated numerically. Upon selecting the 6-point Gaussian quadrature as the numerical scheme to be used, the integral in the above equation can be evaluated as (Abramowitz and Stegun, 1972):

$$\int_{b_{n}}^{b_{n+1}} \overline{U}_{zi}(k) J_{0}(kr) k dk = \frac{b_{n+1} - b_{n}}{2} \sum_{p=1}^{6} w_{p} \overline{U}_{zi}(\beta_{p}) J_{0}(\beta_{p}) \beta_{p}$$
 (5-66)

where

$$\beta_p = \left(\frac{b_{n+1} - b_n}{2}\right) x_p + \left(\frac{b_{n+1} + b_n}{2}\right) \tag{5-67}$$

and x_p and w_p are the Gaussian nodes and their corresponding weights, respectively.

The parameter b_n defines the limits of each integration which can be chosen arbitrarily. However, Cornille (1972) indicated that the convergence of the Gaussian quadrature is greatly improved if the limits are selected to be the successive roots of the derivative of the Bessel function that comprise the kernel of the inverse transform. Based on a sensitivity analysis conducted by the author, subdividing the region between the successive roots of the Bessel function of order one (that is, the derivative of the Bessel function of order zero) into ten smaller regions of equal intervals provided satisfactory results for the numerical integration.

It is also noted that the upper bound of the integral shown in Equation (5-64) is equal to infinity. This indicates that the summation of integrals shown in Equation (5-65) should also span over an infinite range. However, as it was indicated by Kim (2011), the numerical integration converges very rapidly even after the first few cycles of the Bessel function comprising the kernel of the inverse Hankel transform. Therefore, in his static solution for a viscoelastic layered system, the first five cycles of the Bessel function were used to invert the Hankel transform near the loaded area, and less number of cycles in the region far from the loading (Kim, 2011). The developers of the axisymmetric spectral element method used the Fourier-Bessel series (which is the discrete version of the Hankel transform) in their solution and the summation was also carried out approximately for the first five cycles of the Bessel function (Al-Khoury et. al., 2001a). Although the details will be omitted for the compactness of this paper, the sensitivity analysis performed for the proposed algorithm also showed that the numerical integration over the first five cycles of the Bessel function is adequate for the solution.

5.9. Numerical Inversion of the Laplace Transform

For the inverse Laplace transform, a multi precision numerical scheme known as the Fixed Talbot Algorithm is adopted in this paper due to its efficiency, accuracy, and ease for implementation (Abate and Valko, 2004). The Bromwich integral which is the standard equation for the inverse Laplace transform is given as:

$$U_{zi}(t) = \frac{1}{2\pi j} \int_{B} e^{ts} \hat{U}_{zi}(s) ds$$
 (5-68)

where $j = \sqrt{-1}$. The contour, B, chosen for the above integral is along the following path:

$$s(\theta) = \alpha \theta(\cot \theta + j), \quad -\pi < \theta < +\pi$$
 (5-69)

where α is a fixed value calculated as:

$$\alpha = \frac{2M}{5t} \tag{5-70}$$

In Equation (5-70), M is the number of precision decimal digits to be used for the numerical analysis. For the sake of accuracy, this value is specified to be equal to the machine precision. By replacing the contour path in Equation (5-68) with the one shown in Equation (5-69), one finds:

$$U_{zi}(t) = \frac{\alpha}{\pi} \int_{0}^{\pi} \text{Re} \left[e^{ts(\theta)} \hat{U}_{zi}(s(\theta)) (1 + j\gamma(\theta)) \right] d\theta$$
 (5-71)

where,

$$\gamma(\theta) = \theta + (\cot \theta - 1)\cot \theta \tag{5-72}$$

Finally, the inverse Laplace transform is obtained by approximating the integral shown in Equation (5-71) through the trapezoidal rule:

$$U_{zi}(t) = \frac{\alpha}{M} \left\{ \frac{1}{2} \hat{U}_{zi}(\alpha) e^{\alpha t} + \sum_{q=1}^{M-1} \text{Re} \left[e^{ts(\theta_q)} \hat{U}_{zi}(s(\theta_q)) (1 + j\gamma(\theta_q)) \right] \right\}$$
 (5-73)

where,

$$\theta_q = \frac{q\pi}{M} \tag{5-74}$$

5.10. System Response To Arbitrary Loading

As it was described in Equations (5-61) and (5-62), the boundary condition considered in the previous sections was for a unit impulse load distributed over a circular area. As such, the vertical displacement, U_{zi} , obtained from Equation (5-73) represents the unit impulse response

of the layered system in time domain. The primary advantage of the time domain unit impulse response is that the system response to any arbitrary loading can be obtained through the convolution integral (Santamarina and Fratta, 1998, Bendat and Piersol, 2010). Theoretically, this convolution integral for a continuous function is given as:

$$y_{zi}(t) = U_{zi}(t) * T(t) = \int_{0}^{t} U_{zi}(t-\tau)T(\tau)d\tau$$
 (5-75)

where T(t) could be any arbitrary time dependent loading function and $y_{zi}(t)$ is the corresponding vertical displacement at node i. For a discrete signal such a FWD time history, the above equation needs to be evaluated numerically as (Santamarina and Fratta, 1998, Bendat and Piersol, 2010):

$$y_{zi}(t_n) = \sum_{t_p=1}^{t_n} U_{zi}(t_n - t_p) T(t_p) \Delta t$$
 (5-76)

where Δt is time interval of the discrete signal and $t_n = n\Delta t$ for an integer n.

CHAPTER 6 - IMPLEMENTATION AND VALIDATION OF ALGORITHM – VISCOWAVE

The solution presented in the preceeding chapter has been implemented into a computer algorithm named ViscoWave (for Viscoelastic Wave analysis). The algorithm was used to simulate the behavior of elastic and viscoelastic structures subjected to a FWD loading. In addition, other available solutions were also used to simulate the response of the same pavement structures for validation of the ViscoWave algorithm. The results of these numerical simulations are presented in this chapter.

6.1. Simulation of an Elastic Structure using ViscoWave and LAMDA

The properties of the pavement layers used for the elastic analysis are shown in Table 6-1. The FWD loading was idealized to be a half-sine load distributed over a circular area of radius 6 in., a peak magnitude of 9.0 kips, and a duration of 26 ms. The surface deflections were calculated at radial distances of 0 in., 8 in., 12 in., 18 in., 24 in., 36 in., and 60 in.from the center of the loading plate.

Table 6-1 Layer Properties for Elastic Simulation of LAMDA and ViscoWave

Layer	Elastic Modulus (ksi)	Poisson's Ratio	Thickness (inch)	Mass Density (pcf)
Asphalt	145	0.35	6	4.503
Base	30	0.40	10	3.882
Subgrade	15	0.45	∞	3.106

In order to verify the results from ViscoWave, the elastic simulation was also conducted using the axisymmetric spectral element algorithm, namely LAMDA, which has already been verified through a comparison with 3-dimensional FEA solution (Al-Khoury et. al., 2001a, Lee, 2011).

The time histories for the resulting surface deflections are shown in Figure 6-1. The figure indicates that ViscoWave and LAMDA showed almost identical results, which validates the algorithm behind ViscoWave.

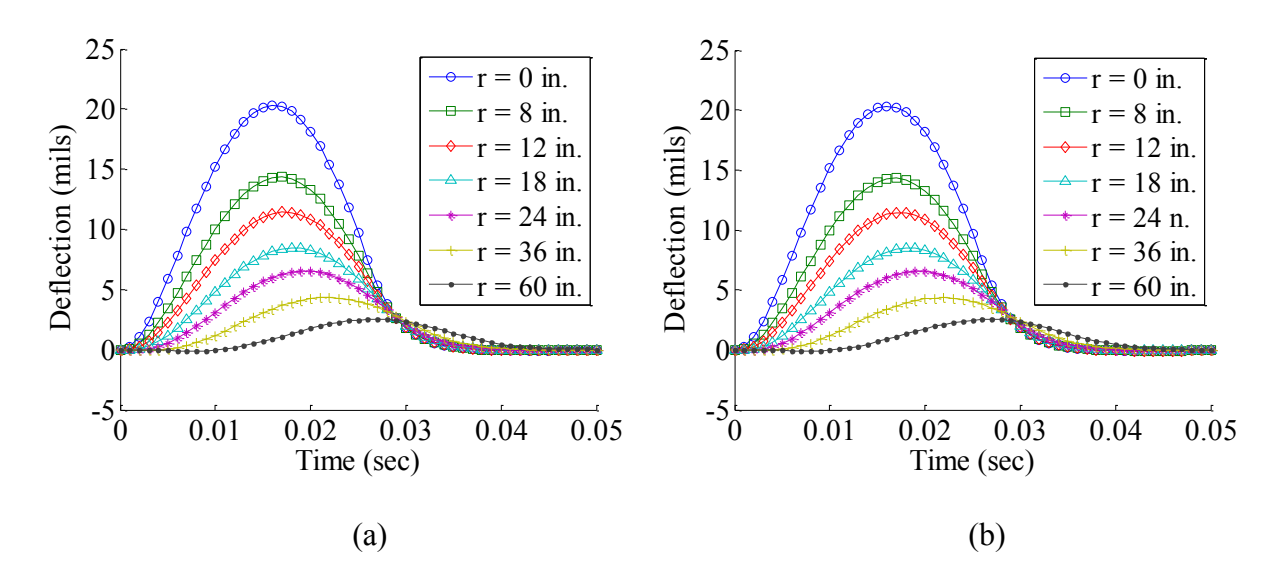


Figure 6-1 Surface Deflections of a Layered Elastic Structure from (a) ViscoWave and (b)

LAMDA

6.2. Simulation of Viscoelastic Structures using ViscoWave

The viscoelastic simulation was carried out using the same pavement structure that was used for the previous elastic simulation (Table 1) with a couple of exceptions. The viscoelasticity of the asphalt concrete was modeled using two different creep compliance functions: one that represents a low temperature behavior (Figure 6-2a) and the other representing a high temperature behavior in which the viscoelastic effects are more pronounced (Figure 6-2b). In addition, for each of the creep compliance functions shown in Figure 6-2, the subgrade layer was first modeled to be a halfspace (infinite thickness) and then with a shallow bedrock (infinite sitffness) located 9.6 ft. below the pavement surface.

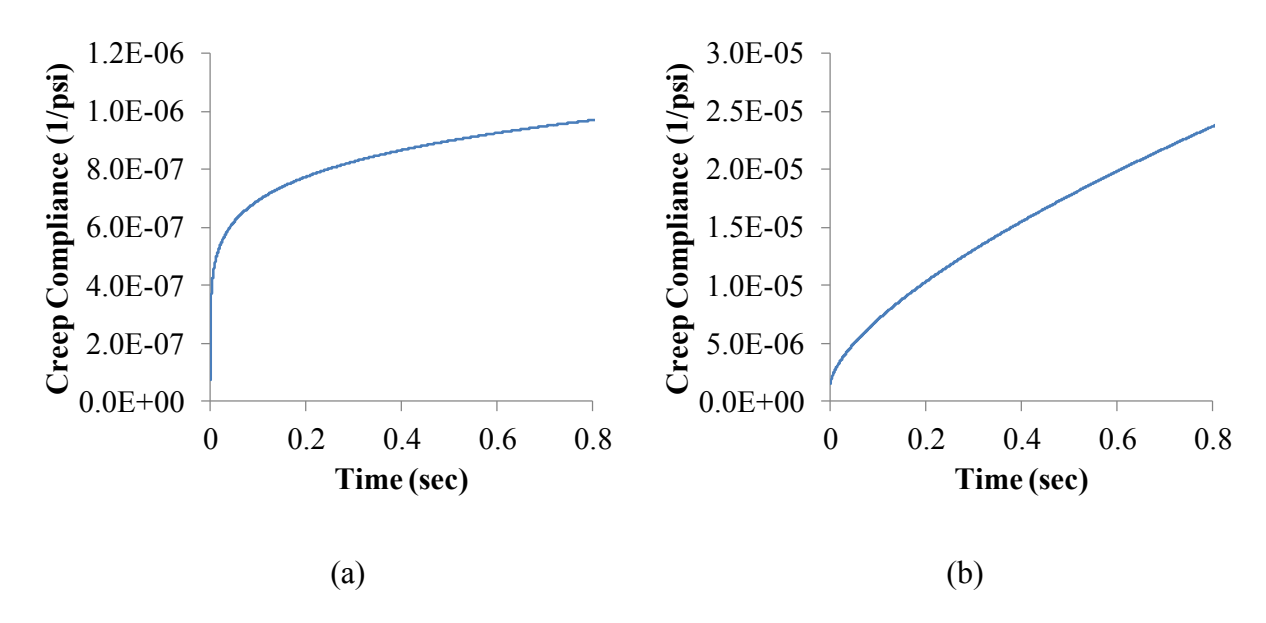


Figure 6-2 (a) Low Temperature and (b) High Temperature Asphalt Creep Compliance Curves

Used for ViscoWave Simulation

To verify the results of the viscoelastic simulation from ViscoWave, a commercially available FEA package, ADINA, was used to simulate the dynamic response of the viscoelastic pavement subjected to the FWD loading. Figure 6-3 shows the geometry and the FEA mesh that was used for the analysis. Although the elements in ViscoWave assume that the elements extend to infinity in the horizontal direction and also in the vertical direction for the one noded element, the FEA simulation was inevitably conducted with a finite geometry. More specifically, the FEA model only extended to 20 ft. in the horizontal direction and 41.3 ft. in the vertical direction for the

simulation of the halfspace (Figure 6-3a). The FEA mesh was generated in such a way that finer meshes were used near the loaded area and coarser meshes were used near the geometric boundaries. A total of approximately 8,600 axisymmetric elements, each consisting of 9 nodes, were consistently used for all FEA simulations.

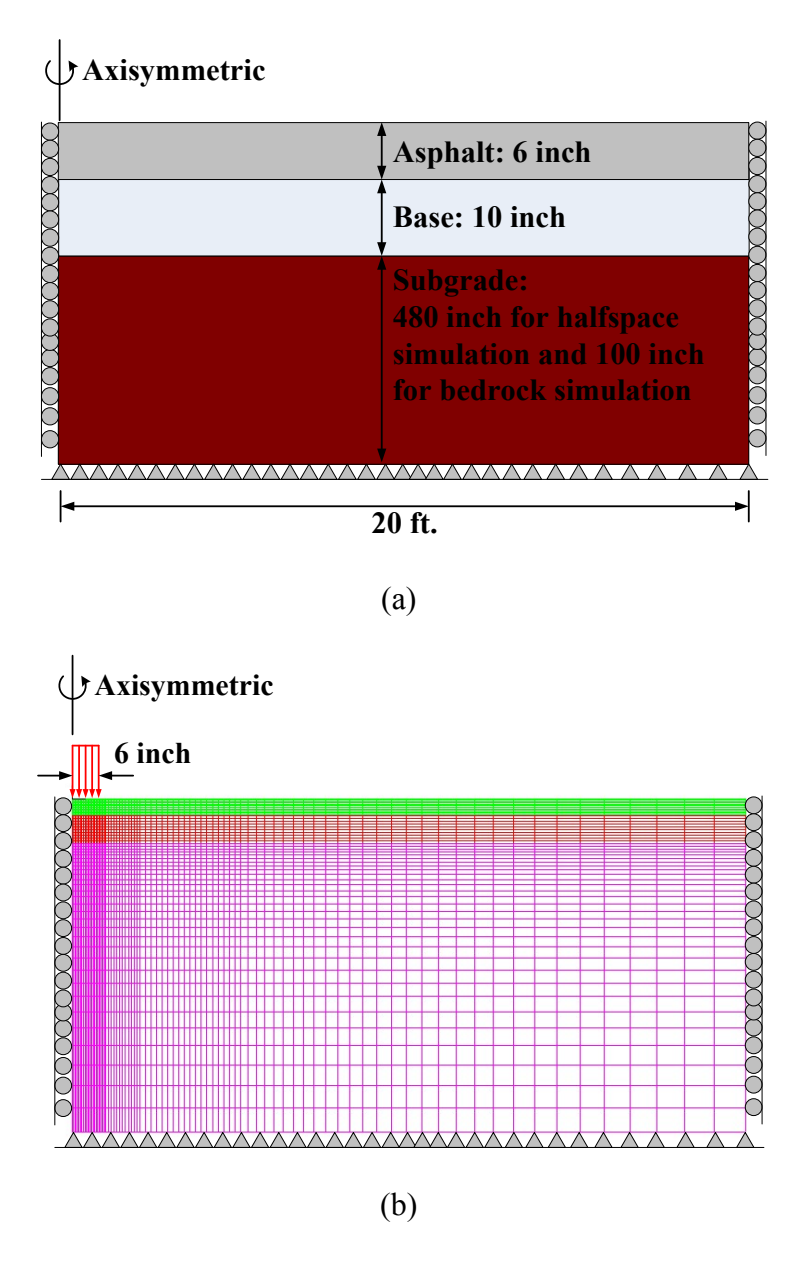


Figure 6-3 (a) Axisymmetric Finite Element Geometry and (b) Finite Element Mesh Used for Simulation of Pavement Response Under FWD Loading

The simulated deflection time histories generated for the low temperature asphalt pavement with a halfspace and with a shallow bedrock are shown in Figure 6-4 and Figure 6-5, respectively. Both figures indicate that the results from ViscoWave and ADINA are in excellent agreement. In Figure 6-4, the effect of phase characteristics in the viscoelastic material can be clearly identified as shown by the increased duration (or delayed recovery) of the deflections when compared to the elastic simulation results shown in Figure 6-1. However, the deflections calculated from ADINA at 60 in. from the center of the load plate showed some unexpected outcome towards the end of the time history, especially for the case with a shallow bedrock (Figure 6-5b). It is believed that this is primarily due to the horizontal boundary at which the stress wave is reflected back towards the loaded area and secondarily due to the increased error coming from the increased size of the mesh used for the FEA analysis (Lee, 2013).

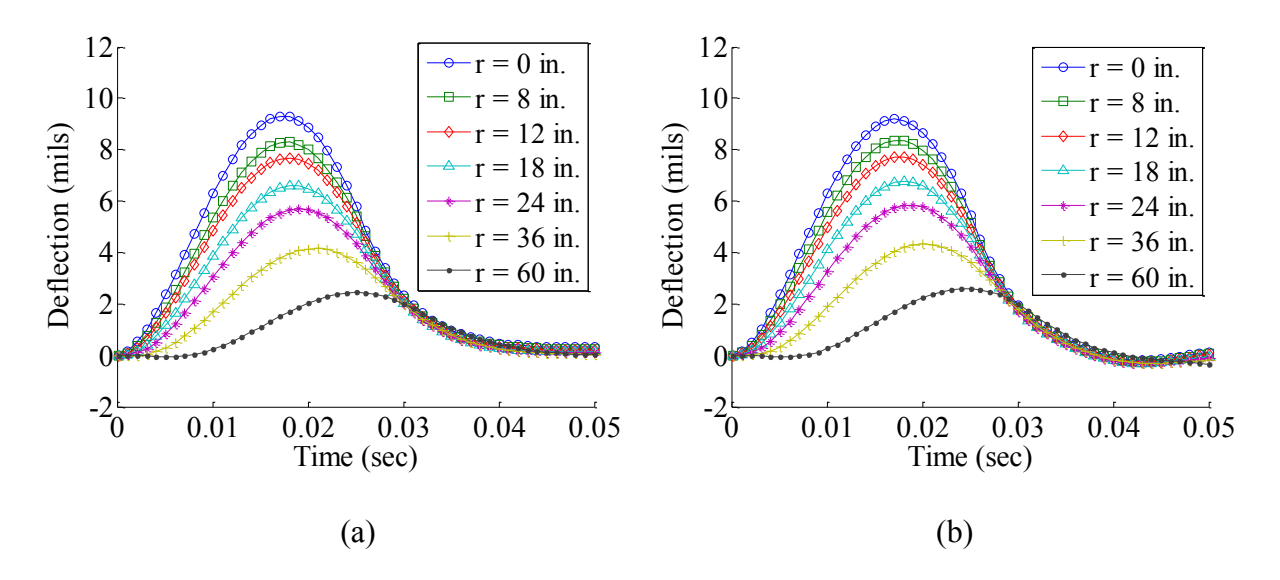


Figure 6-4 Surface Deflections of a Layered Viscoelastic Structure with a Halfspace at Low Temperature Simulated Using (a) ViscoWave and (b) ADINA

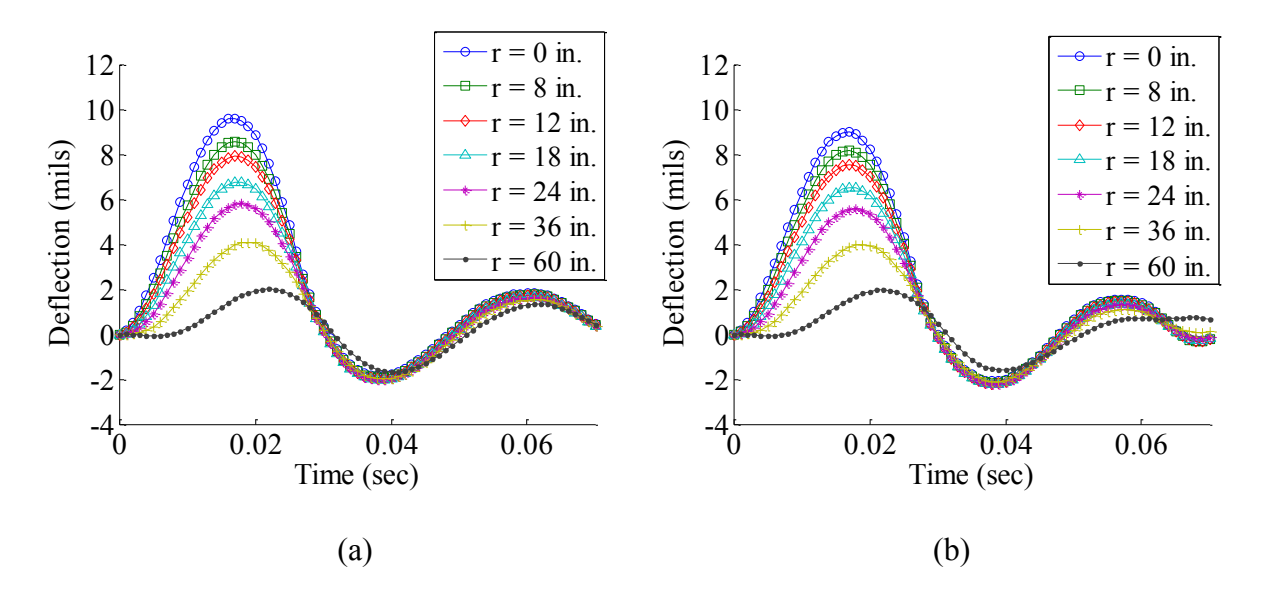


Figure 6-5 Surface Deflections of a Layered Viscoelastic Structure with a Bedrock at 3 m below Surface at Low Temperature Simulated Using (a) ViscoWave and (b) ADINA

The simulated deflection time histories for the high temperature asphalt pavement are shown in Figure 6-6 for the case with a halfspace and in Figure 6-7 for the case with a shallow bedrock. As expected, the viscoelastic effect is even more pronounced when compared to the low temperature results, as evidenced in Figure 6-6 by the delayed recovery and in Figure 6-7 by the noticeable phase difference seen in the free vibration response. Although it is not as significant as the one shown in Figure 6-5b, the deflection simulated for the outmost sensor (60 in. from center of load plate) shown in Figure 6-7b again shows the effect of the horizontal boundary placed at 20 ft. Nonetheless, both Figure 6-6 and Figure 6-7 again show that the ViscoWave results are in excellent agreement with the FEA results. This concludes the validation of the viscoelastic simulation using ViscoWave.

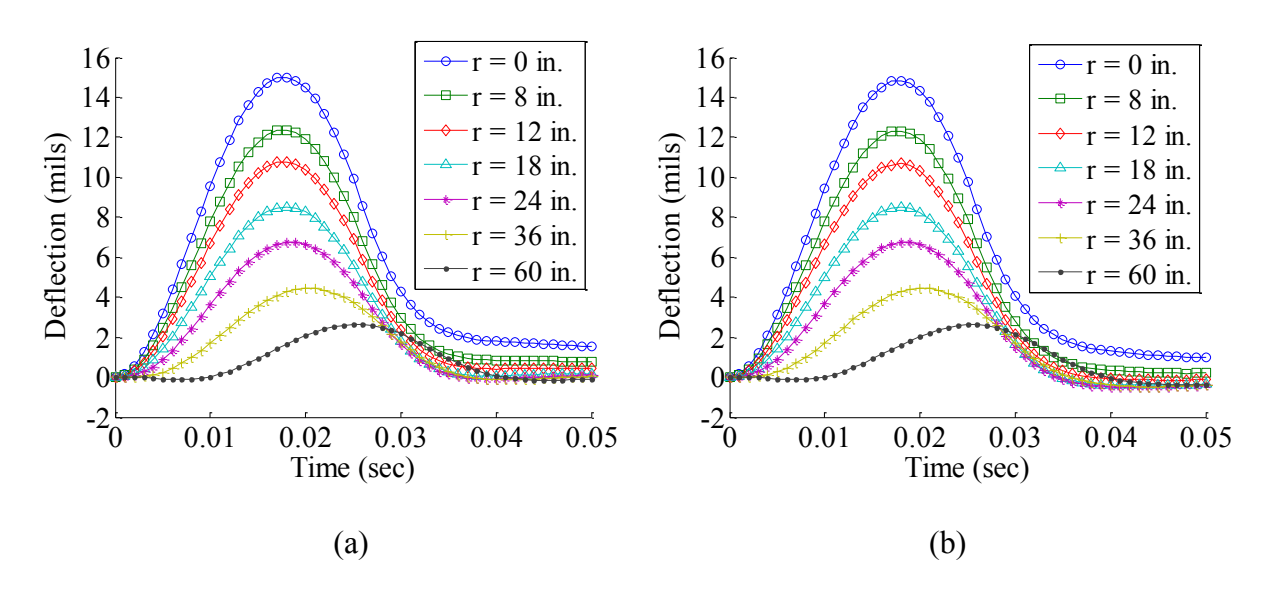


Figure 6-6 Surface Deflections of a Layered Viscoelastic Structure with a Halfspace at High Temperature Simulated Using (a) ViscoWave and (b) ADINA

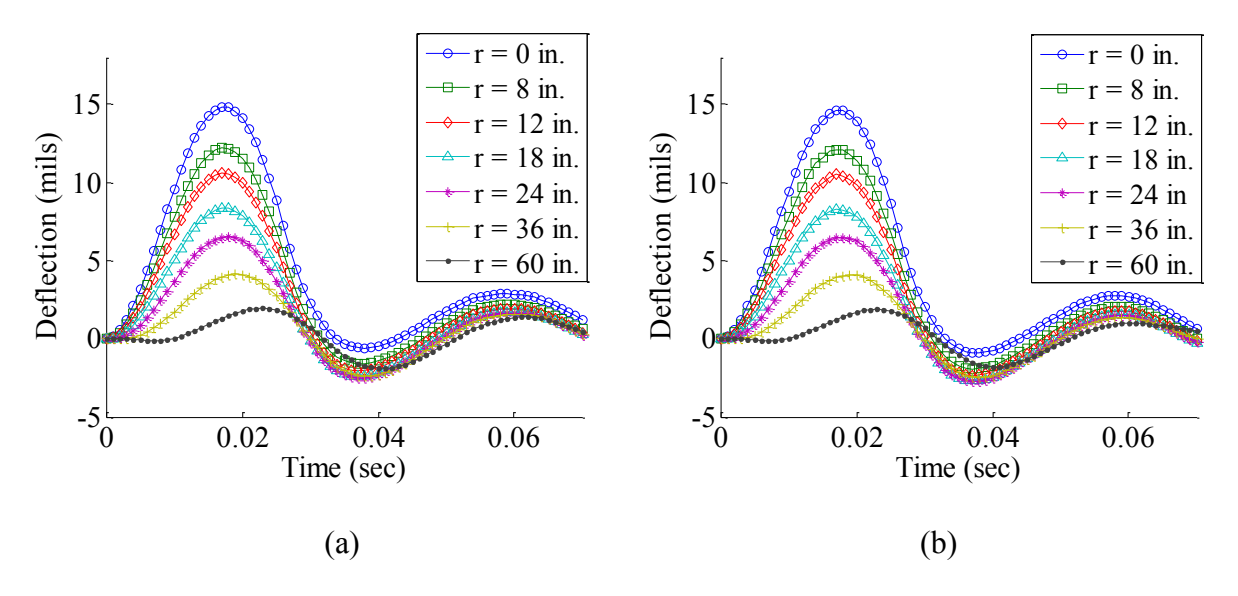


Figure 6-7 Surface Deflections of a Layered Viscoelastic Structure with a Bedrock at 3 m below Surface at High Temperature Simulated Using (a) ViscoWave and (b) ADINA

CHAPTER 7 - THEORETICAL BACKCALCULATION USING VISCOWAVE

In this chapter, the ViscoWave algorithm developed in the previous chapters will be used along with available non-linear optimization algorithms for backcalculation of layer properties from theoretically generated FWD time histories.

7.1. Review of Selected Optimization Algorithms

The non-linear optimization algorithms that were selected for backcalculation were the Gauss-Newton and Levenberg-Marquardt methods. As these are classical optimization methods and the detailed description of these algorithms are available in most optimization textbooks, only a brief overview will be provided in this report (Scales 1985, Rao 2002, Venkataraman 2002).

7.1.1. Objective Function for Optimization and its Derivatives

If the optimization problem includes n independent scalar variables denoted as x_1 through x_n , it is more convenient to gather all the scalar variables together and represent them in a vector form. That is:

$$\mathbf{x} = \begin{bmatrix} x_1 & x_2 & \cdots & x_n \end{bmatrix}^T \tag{7-1}$$

Similarly, the scalar valued functions of x can also be gathered into a vector form:

$$\mathbf{f}(\mathbf{x}) = [f_1(\mathbf{x}) \quad f_2(\mathbf{x}) \quad \cdots \quad f_m(\mathbf{x})]^T \tag{7-2}$$

In backcalculation, the individual functions, f_i , in the above equation is frequently taken as the scalar difference between the measured and simulated deflections, whereas the x_i is referred to the pavement layer parameter that needs to be backcalculated. Then, the objective of the backcalculation would be to minimize the error between the measured and simulated deflections. Mathematically, this can be achieved by finding the vector \mathbf{x} that minimizes the following objective function which is a simple sum of squares of the error:

$$F(\mathbf{x}) = \sum_{i=1}^{m} f_i^2(\mathbf{x}) = \mathbf{f}^T(\mathbf{x}) \cdot \mathbf{f}(\mathbf{x})$$
 (7-3)

It should be noted that in practice, the differences between the predicted and the measured values are more frequently presented in terms of the Root Mean Square Error (RMSE) which has the same units as the measured values. The objective function shown above is related to the RMSE in the following manner:

$$RMSE = \sqrt{\frac{F}{m}}$$
 (7-4)

For the purpose of optimization, taking the first partial derivative on Equation (7-3) with respect to x_i results in a gradient vector of F which can be written as:

$$g_{j} = \frac{\partial F}{\partial x_{j}} = 2\sum_{i=1}^{m} f_{i} \frac{\partial f_{i}}{\partial x_{j}}$$
 (7-5)

or, equivalently in vector form as the following:

$$\mathbf{g}(\mathbf{x}) = \nabla F = 2\mathbf{J}^{T}(\mathbf{x})\mathbf{f}(\mathbf{x}) \tag{7-6}$$

where the Jacobian matrix, J, is defined as the following.

$$\mathbf{J} = \begin{bmatrix} \frac{\partial f_1}{\partial x_1} & \cdots & \frac{\partial f_1}{\partial x_n} \\ \vdots & & \vdots \\ \frac{\partial f_m}{\partial x_1} & \cdots & \frac{\partial f_m}{\partial x_n} \end{bmatrix}$$
(7-7)

Differentiating Equation (7-5) or Equation (7-6) with respect to x_k results in the Hessian matrix of F. That is:

$$G_{kj} = \frac{\partial g_j}{\partial x_k} = 2\sum_{i=1}^m \left\{ \frac{\partial f_i}{\partial x_k} \frac{\partial f_i}{\partial x_j} + f_i \frac{\partial^2 f_i}{\partial x_k \partial x_j} \right\}$$
(7-8)

which can also be written in matrix form as:

$$\mathbf{G}(\mathbf{x}) = \nabla \mathbf{g} = 2\mathbf{J}^{T}(\mathbf{x})\mathbf{J}(\mathbf{x}) + 2\mathbf{S}(\mathbf{x})$$
(7-9)

where the matrix **S** is given as:

$$\mathbf{S}(\mathbf{x}) = \sum_{i=1}^{m} f_i(\mathbf{x}) \mathbf{T}_i(\mathbf{x})$$
 (7-10)

and T_i is the Hessian matrix of f_i :

$$\mathbf{T}_i(\mathbf{x}) = \nabla^2 f_i(\mathbf{x}) \tag{7-11}$$

7.1.2. Basics of Iteration

In order for the objective function given in Equation (7-3) to be minimized, it is evident that its corresponding gradient vector in Equation (7-6) must be a vector of zeros. Denoting the independent variable, objective function value, and the gradient after the p^{th} iteration as \mathbf{x}_p , F_p , and \mathbf{g}_p , respectively, the goal of the following iteration is to find \mathbf{x}_{p+1} that satisfies the zero-gradient condition. Mathematically, this can be stated as the following:

$$\mathbf{g}_{p+1} = \mathbf{g}(\mathbf{x}_{p+1}) = \mathbf{g}(\mathbf{x}_p + \mathbf{r}_p) = \mathbf{0}$$
 (7-12)

where \mathbf{r}_p is the search vector (or direction vector). Expanding the above expression by Taylor series and eliminating the higher order terms results in the following expression:

$$\mathbf{G}_{p}\mathbf{r}_{p} = -\mathbf{g}_{p} \tag{7-13}$$

After the search vector has been found from the above equation, the vector of independent variable, x, is updated in the following manner and the iteration is continued until a satisfactory point has been reached.

$$\mathbf{x}_{p+1} = \mathbf{x}_p + \mathbf{r}_p \tag{7-14}$$

7.1.3. Gauss-Newton Method

By substituting Equation (7-6) and Equation (7-9) into Equation (7-13), the following relationship is obtained for the search vector:

$$\left\{ \mathbf{J}_{p}^{T} \mathbf{J}_{p} + \mathbf{S}_{p} \right\} \cdot \mathbf{r}_{p} = -\mathbf{J}_{p}^{T} \mathbf{f}_{p}$$
 (7-15)

The above equation, along with Equation (7-14), defines the Newton's method. However, the major problem with the above formulation is that the computational effort needed for calculating the S_p is extremely expensive. In the Gauss-Newton method, the computationally expensive matrix S_p is completely neglected and the search vector is found from the following relationship.

$$\mathbf{J}_{D}^{T}\mathbf{J}_{D}\mathbf{r}_{D} = -\mathbf{J}_{D}^{T}\mathbf{f}_{D} \tag{7-16}$$

7.1.4. Levenberg-Marquardt Method

Although the Gauss-Newton method is known to be very efficient, the problem that is frequently encountered is that the matrix $\mathbf{J}_p{}^T\mathbf{J}_p$ being singular or ill-conditioned (Scales 1985). The Levenberg-Marquardt method incorporates a technique for handling the issue of $\mathbf{J}_p{}^T\mathbf{J}_p$ being singular by adding an identity matrix to $\mathbf{J}_p{}^T\mathbf{J}_p$. In other words, the search vector is found from a modified version of Equation (7-16) which can be written as:

$$\left(\mathbf{J}_{p}^{T}\mathbf{J}_{p} + \alpha_{p}\mathbf{I}_{p}\right)\mathbf{r}_{p} = -\mathbf{J}_{p}^{T}\mathbf{f}_{p} \tag{7-17}$$

It should be noted that as $\alpha_p \to 0$, the above equation becomes identical to the Gauss-Newton method. On the other extreme, as $\alpha_p \to \infty$, the matrix $\mathbf{J}_p{}^T\mathbf{J}_p$ becomes negligible and the search vector \mathbf{r}_p becomes an infinitesimal step in the direction of steepest descent (Scales 1985). However, the actual magnitude of α_p should be found such that the objective function, F, is minimized at $\mathbf{x}_p + \mathbf{r}_p$.

7.1.5. Remarks on the Optimization Routine

Both the Gauss-Newton and Levenberg-Marquardt optimization routines used for this study were readily implemented in the "Isqnonlin" function of Matlab's Optimization Toolbox (Mathworks 2008). The backcalculation was initiated using the Gauss-Newton method which is known to be

more efficient. However, when the problem of $\mathbf{J}_p^T \mathbf{J}_p$ matrix being singular or ill-conditioned for inversion, the Gauss-Newton was terminated and the backcalculation was continued using the Levenberg-Marquardt method.

7.2. Theoretical Backcalculation Using ViscoWave

The theoretical backcalculation was carried out in two folds: (1) using a single set of FWD time histories representing a single temperature and multiple sets of FWD time histories at various temperatures. The results and findings of the theoretical backcalculation exercise are provided in the remainder of the chapter.

7.2.1. Single Temperature Backcalculation

7.2.1.1. Reference Pavement Structures and Seed Values for Backcalculation

The properties of the reference pavement structures sitting on a halfspace and on a bedrock are summarized in Table 7-1. The generalized power function was used for modeling the viscoelastic behavior of the asphalt surface with its coefficients shown in the table. The FWD loading was again idealized to be a half-sine load with a peak magnitude of 9.0 kips and a duration of 26 ms, distributed over a circular area of radius 6 in. The time histories were modeled with a discrete time interval of 0.2 ms and a duration of 50 ms for pavement with a halfspace and 70 ms for the pavement on a bedrock. The surface deflections were calculated at radial distances of 0 in., 8 in., 12 in., 18 in., 24 in., 36 in., and 60 in. from the center of the loading plate. Table 7-2 shows the

three sets of seed values that were assigned to the variables prior to backcalculation. The first set of seed values set to ± 50 percent increase from the true values. In order to study the effect of seed values, the second and the third sets of seed values were set to 100 percent and -80 percent increase from the true values, respectively, for all variables. These seed values were consistently used for both the pavement structures with and without a halfspace.

Table 7-1 Reference Pavement Structures

Layer	D ₀ (1/psi)	D ₁ (1/psi)	m	Elastic Modulus (psi)	Poisson's Ratio	Density (pcf)	Thickness (in.)
Asphalt	3.00E-07	5.00E-07	0.3	N/A	0.35	145	6
Base	N/A		30,000	0.4	125	12	
Subgrade			15,000	0.45	100	$\infty^{1}/60^{2}$	

Note 1: For pavement with a halfspace Note 2: For pavement with a bedrock

Table 7-2 Seed Values Used for Backcalculation

Variable	Seed Value (Percent Increase from True Value)			
v arrable	Seed Set 1	Seed Set 2	Seed Set 3	
D ₀ (1/psi)	4.50E-07 (50%)	6.00E-07 (100%)	6.00E-08 (-80%)	
D ₁ (1/psi)	2.50E-07 (-50%)	1.00E-06 (100%)	1.00E-07 (-80%)	
m	0.45 (50%)	0.60 (100%)	0.06 (-80%)	
E_{Base} (psi)	15,000 (-50%)	60,000 (100%)	6,000 (-80%)	
$E_{ m Subgrade}$ (psi)	22,500 (50%)	30,000 (100%)	3,000 (-80%)	

7.2.1.2. Backcalculation Results for Pavement Structure With a Halfspace

The deflection time histories generated from ViscoWave for the reference pavement with a halfspace (Table 7-1) are shown in Figure 7-1a, whereas those generated for the pavement structures with the three sets of seed values (Table 7-2) are shown in Figure 7-1b through Figure 7-1d. As shown by the deflection time histories in Figure 7-1, the first set of seed values resulted in the deflection time histories that are very similar to those from the reference pavement. The second set of seed values resulted in deflection time histories that are quite different from those of the reference pavement in terms of magnitude but the shape of the time histories still resemble those of the reference pavement. The last set of seed values resulted in the poorest deflection time histories both in terms of shape and magnitude. Based on these observations, it is expected that this set of seed values has the greatest potential for converging to the true values with the fewest number of iterations, followed by the second and third set of seeds.

The backcalculation was conducted using the Gauss-Newton and Levenberg-Marquardt optimization routines previously described in this chapter. The backcalculation was initiated using the Gauss-Newton method and was switched over to the Levenberg-Marquardt method after 2 iterations for seed sets 1 and 2, and after the first iteration for seed set 3. The three solutions converged after 24 (seed set 1), 60 (seed set 2), and 42 (seed set 3) iterations. The RMSE histories and the deflection time histories obtained after backcalculation are shown in Figure 7-2 and Figure 7-3, respectively. As expected, Figure 7-2a and Figure 7-2b show that the first set of seed values converged faster than the second set, and the backcalculated deflection time histories shown in Figure 7-3b and Figure 7-3c indicate that the backcalculated solution

may be reasonably close to the true values. On the other hand, the terminal RMSE shown in Figure 7-2c indicates immediately that the backcalculation with the third set of seed values converged to a wrong solution and this is confirmed by the time histories shown in Figure 7-3d.

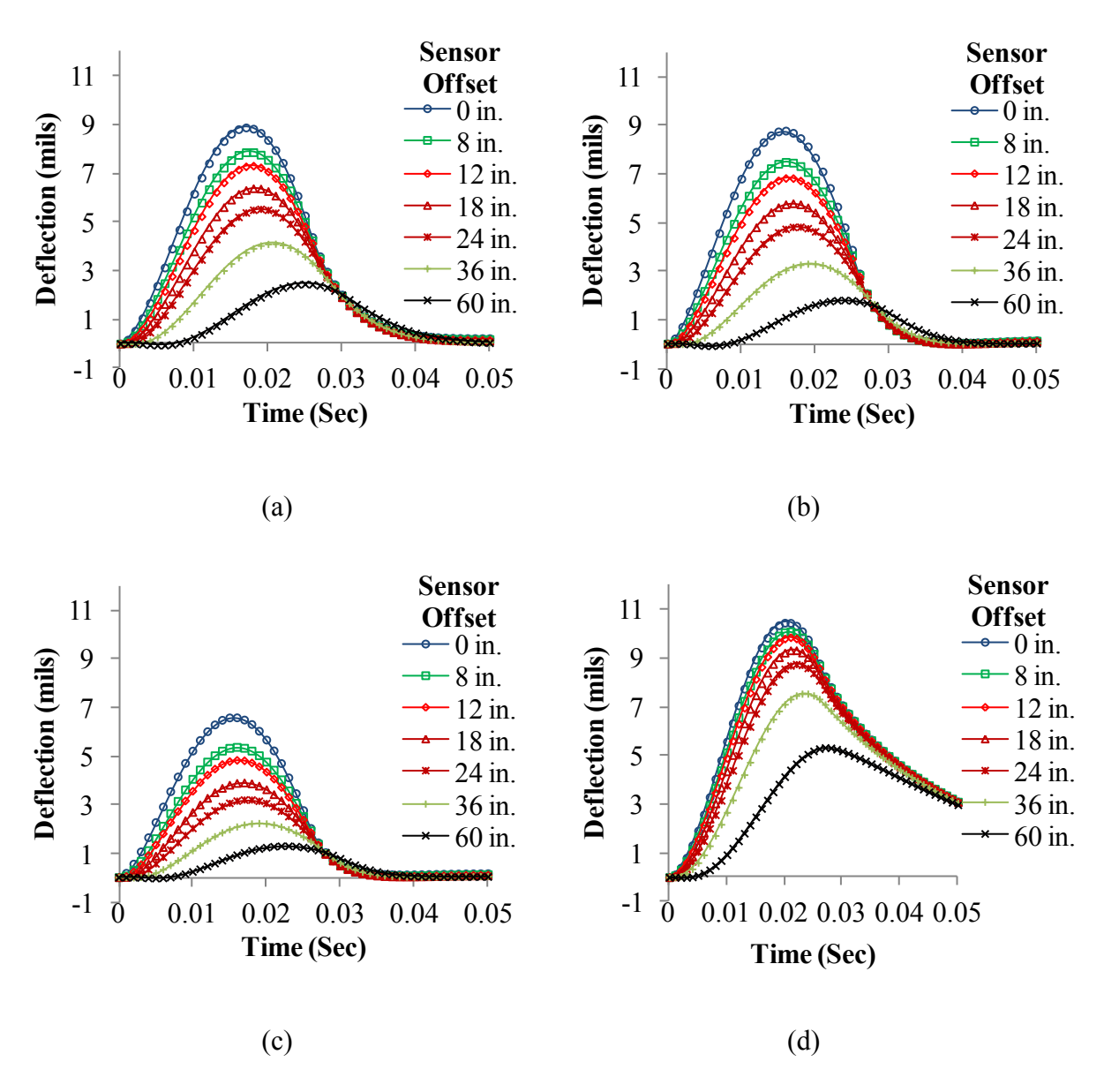


Figure 7-1 Deflection Time Histories from Pavement Structure on a Halfspace; (a) Reference Pavement, (b) Seed Set 1, (c) Seed Set 2, and (d) Seed Set 3

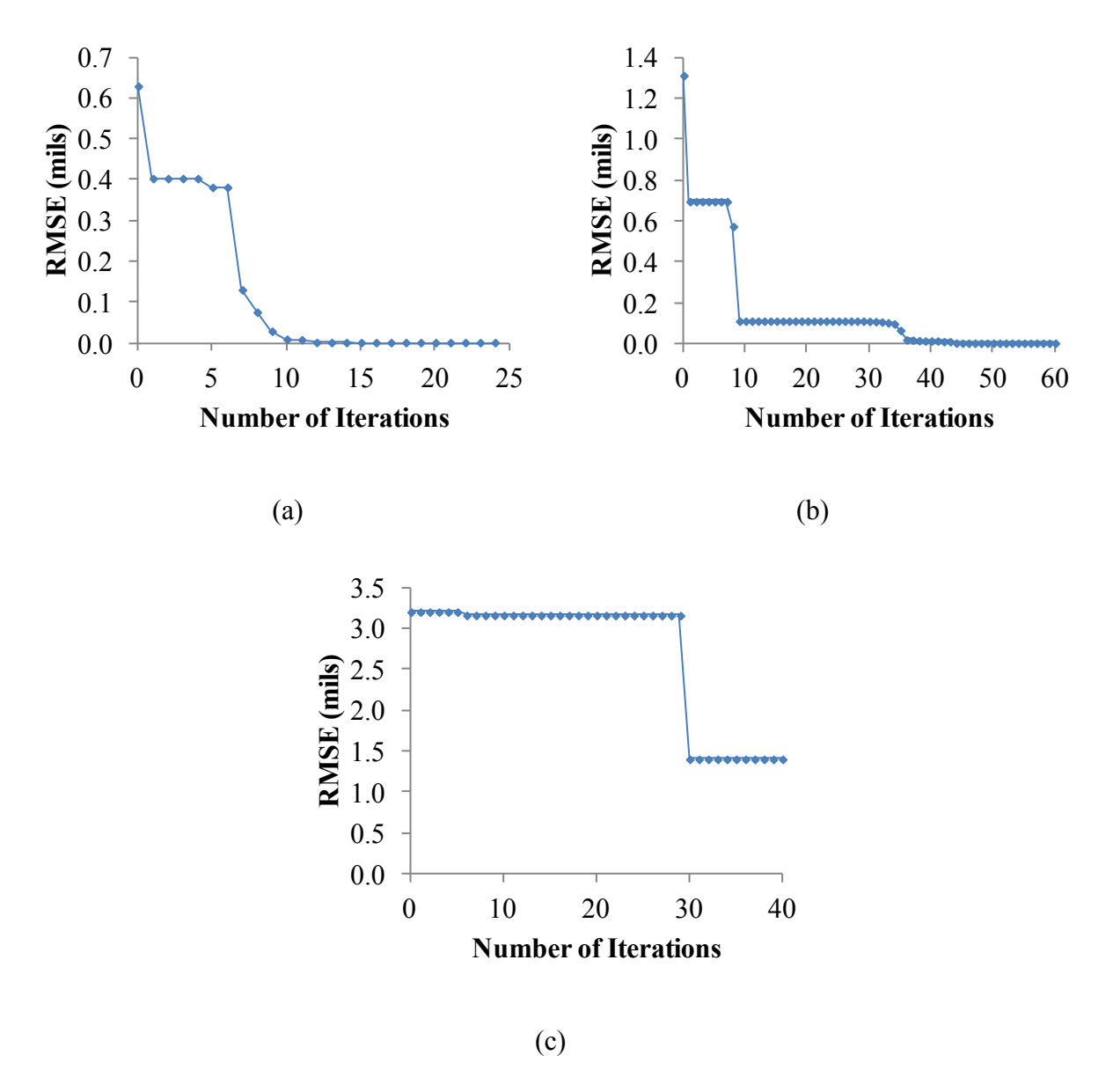


Figure 7-2 History of Root Mean Square Error for (a) Seed Set 1, (b) Seed Set 2, and (c) Seed Set 3

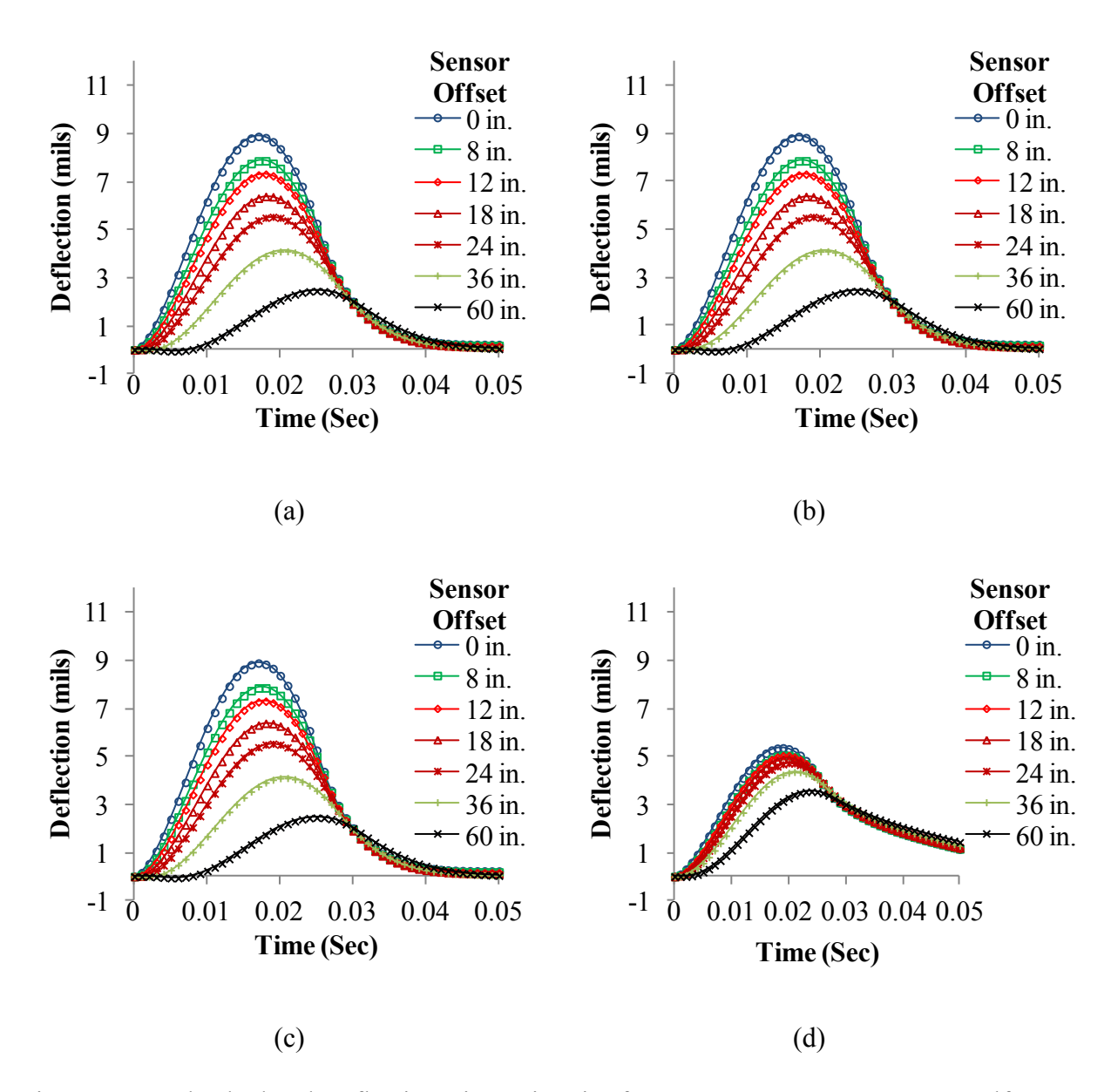


Figure 7-3 Backcalculated Deflection Time Histories from Pavement Structure on a Halfspace; (a) Reference Pavement, (b) Seed Set 1, (c) Seed Set 2, and (d) Seed Set 3

The backcalculated results are summarized in Table 7-3, for all sets of seed values. Again, the table confirms that the first set of seed values resulted in the best outcome in terms of the backcalculated values and their percent errors. It also confirms that the third set of seed values converged to a wrong solution, with the backcalculated D_1 parameter being negative and the backcalculated base and subgrade moduli being very close to the initial seed values.

Table 7-3 Backcalculated Values and Percent Error – Pavement on a Halfspace

Variable	True Value	Backcalculated Value (Absolute Percent Error)		
variable		Seed Set 1	Seed Set 2	Seed Set 3
D ₀ (1/psi)	3.00E-07	3.00E-07 (<0.001%)	3.14E-07 (4.7%)	2.14E-07 (28.8%)
D ₁ (1/psi)	5.00E-07	5.00E-07 (<0.001%)	5.27E-07 (5.5%)	-2.24E-07 (144.8%)
m	0.30	0.30 (0.002%)	0.34 (12.9%)	0.05 (84.7%)
E_{Base} (psi)	30,000	30,000 (<0.001%)	30,229 (0.8%)	5,997 (80.0%)
E _{Subgrade} (psi)	15,000	15,000 (<0.001%)	14,988 (0.1%)	3,003 (80.0%)

The above observations confirm the well-accepted fact that both the Gauss-Newton and Levenberg-Marquardt methods may only find the local minimum and not necessarily the global minimum (Scales, 1985). In other words, with the Gauss-Newton and Levenberg-Marquardt methods, it is important that reasonable seed values are chosen in order for the backcalculation to converge to the correct solution. Figure 7-4 through Figure 7-8 show the convergence histories of the backcalculated parameters for all three cases and confirm the observations already made in the above.

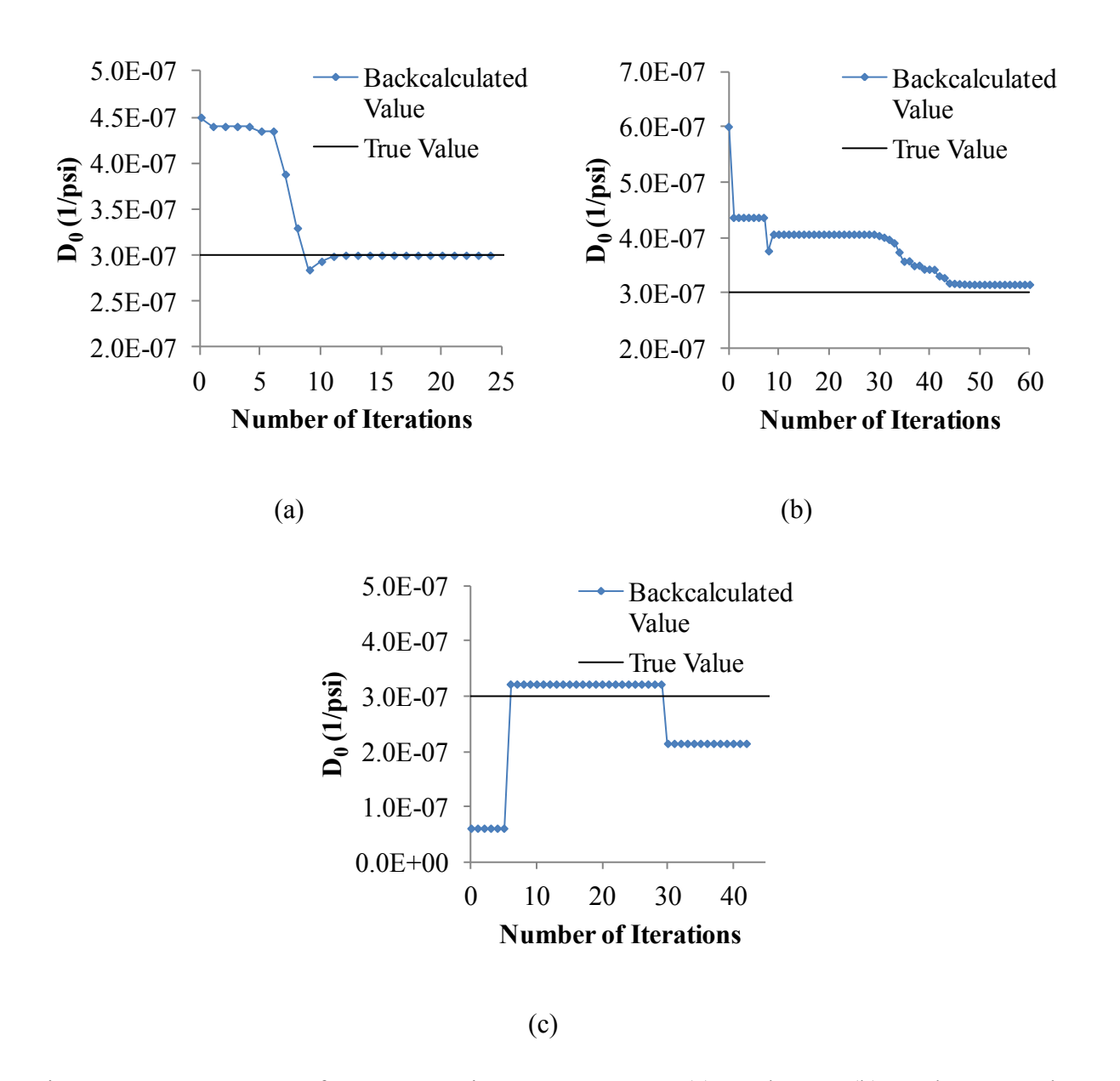


Figure 7-4 Convergence of Power Function Parameters D_0 ; (a) Seed Set 1, (b) Seed Set 2, and (c) Seed Set 3 – Pavement Structure on a Halfspace

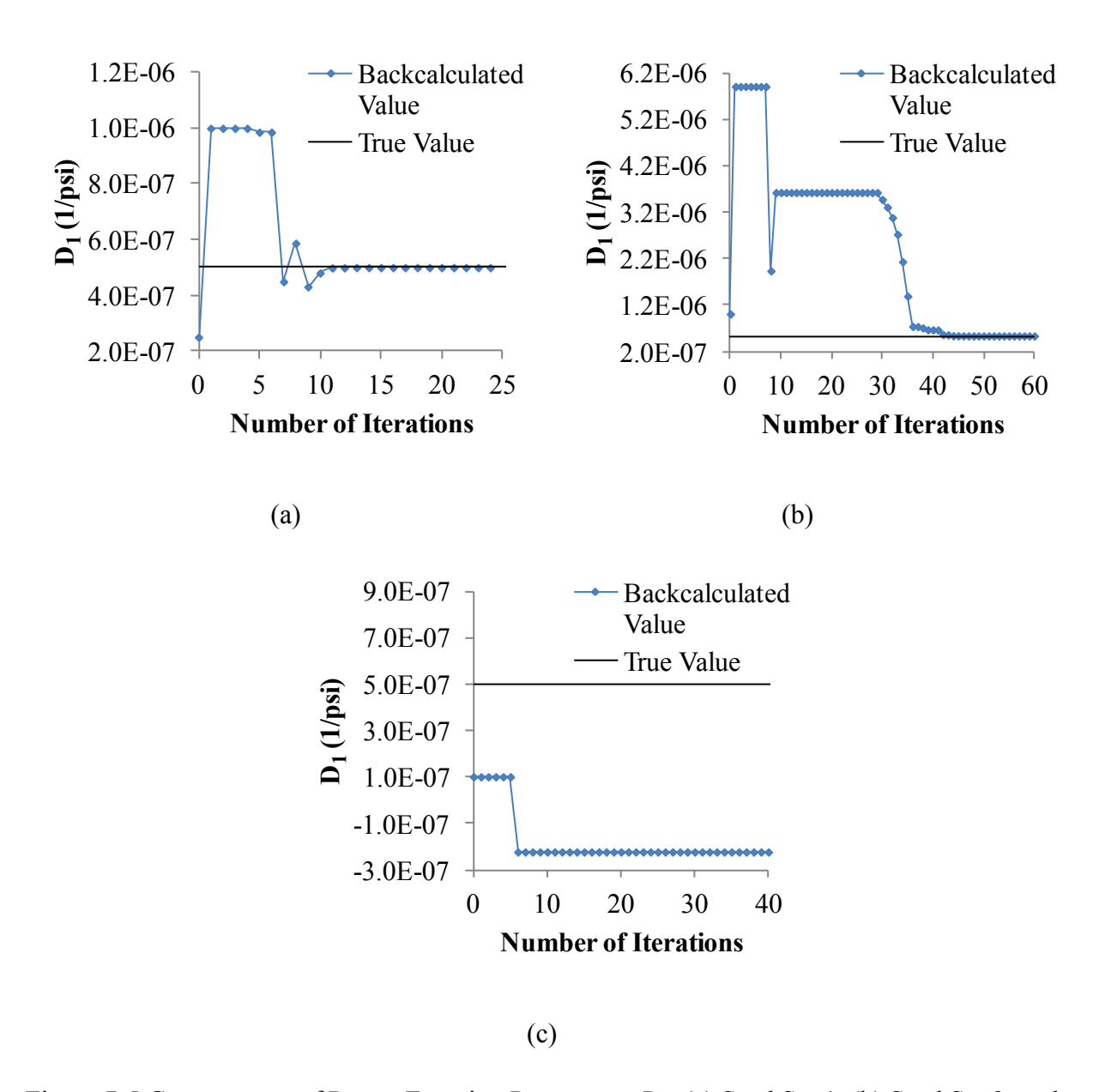


Figure 7-5 Convergence of Power Function Parameters D_1 ; (a) Seed Set 1, (b) Seed Set 2, and (c) Seed Set 3 – Pavement Structure on a Halfspace

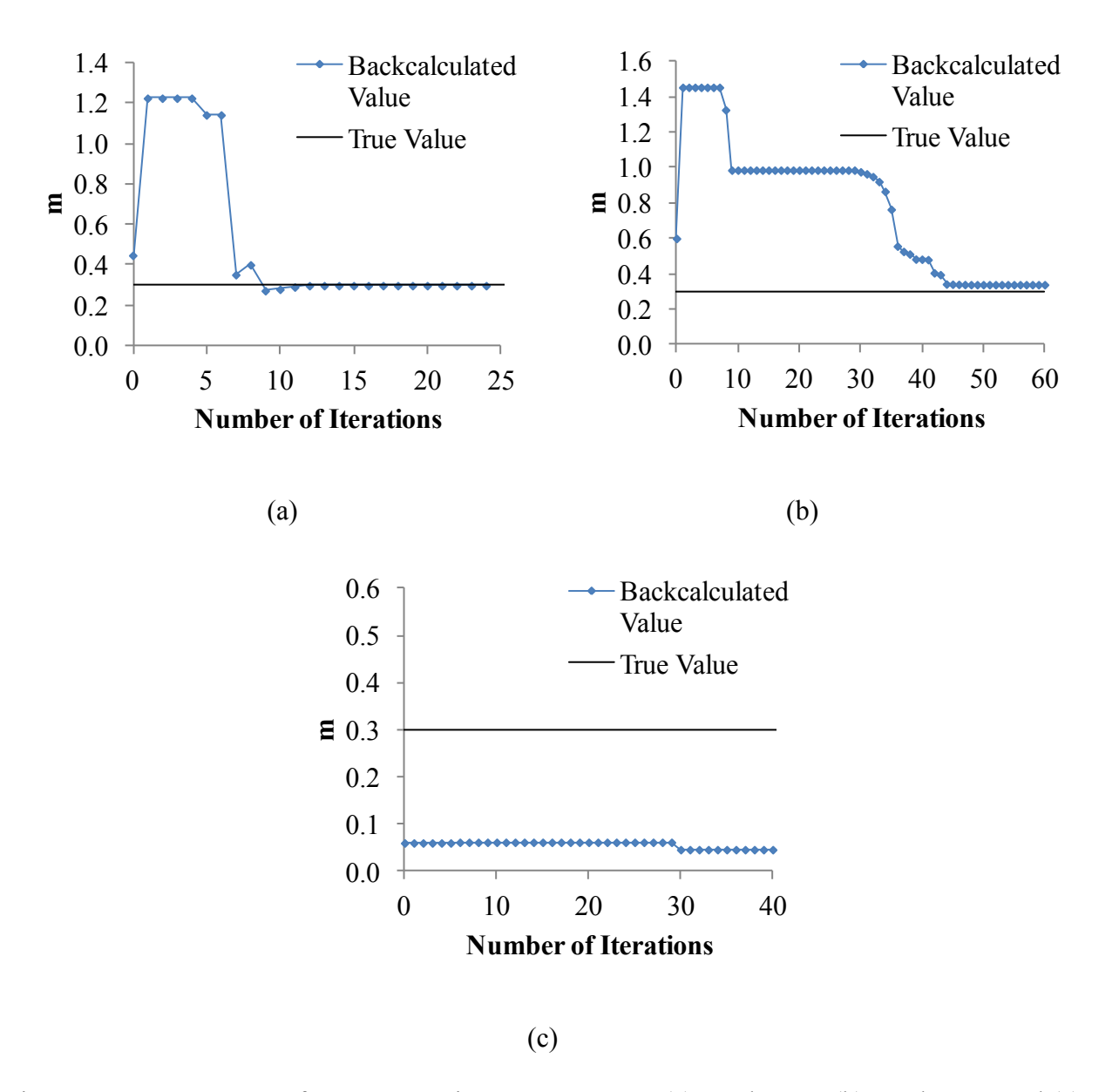


Figure 7-6 Convergence of Power Function Parameters *m*; (a) Seed Set 1, (b) Seed Set 2, and (c) Seed Set 3 – Pavement Structure on a Halfspace

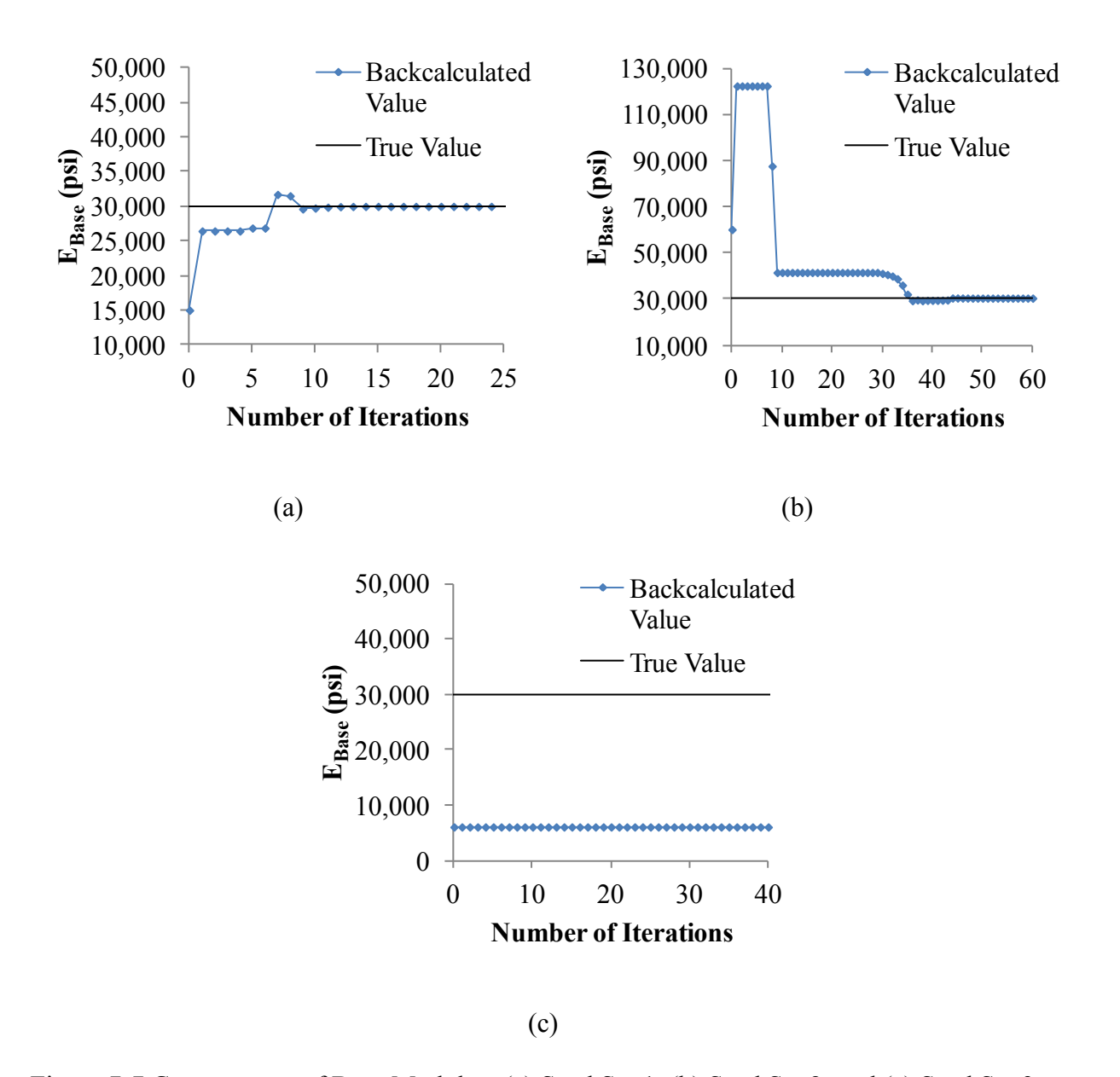


Figure 7-7 Convergence of Base Modulus; (a) Seed Set 1, (b) Seed Set 2, and (c) Seed Set 3 – Pavement Structure on a Halfspace

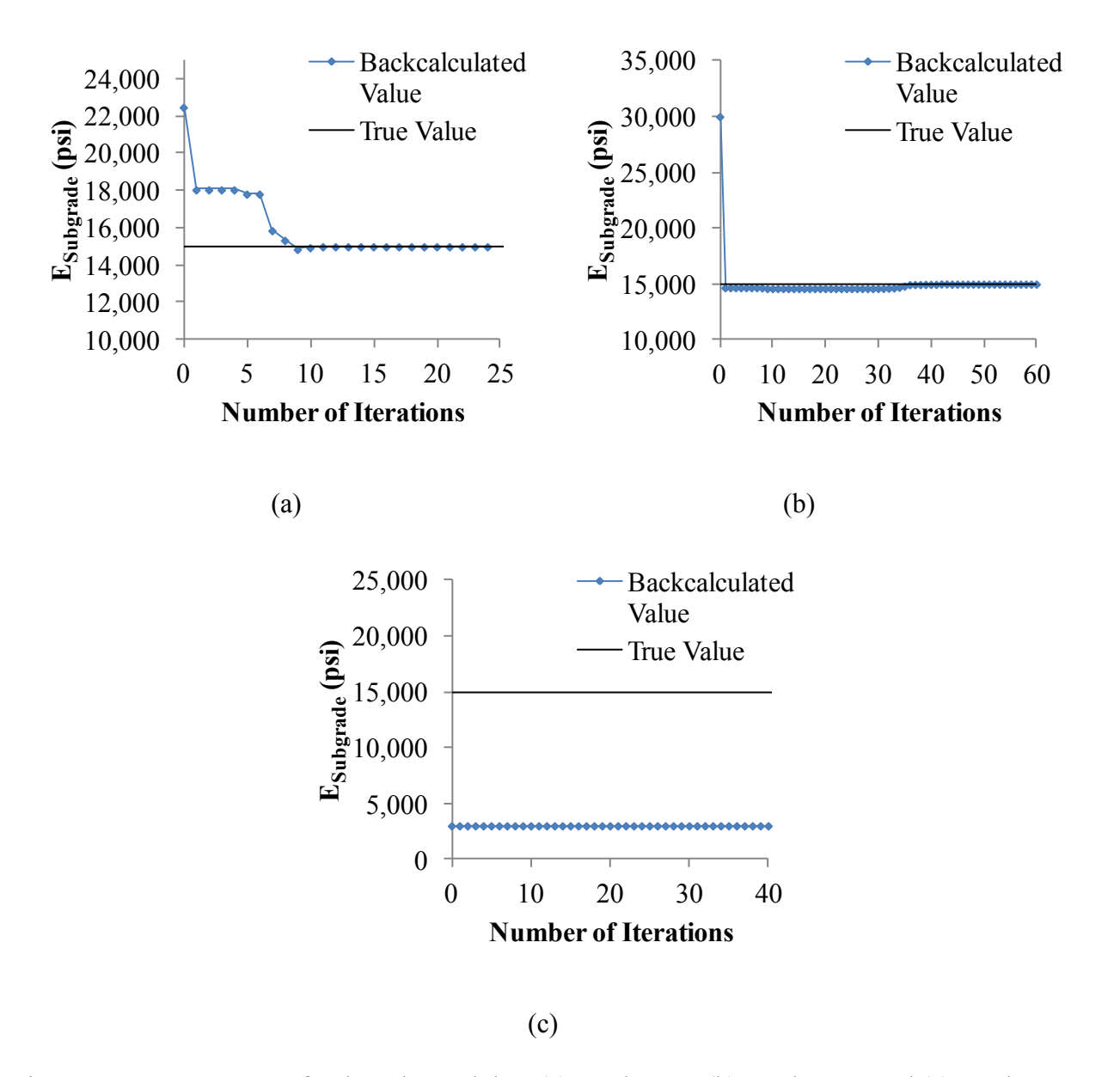


Figure 7-8 Convergence of Subgrade Modulus; (a) Seed Set 1, (b) Seed Set 2, and (c) Seed Set 3

— Pavement Structure on a Halfspace

7.2.1.3. Backcalculation Results for Pavement Structure on a Bedrock

The deflection time histories generated for the reference pavement and the seed structures on a bedrock are shown in Figure 7-9. As was the case with the pavement on a halfspace presented above, the first set of seed values resulted in the deflection time histories that resemble the true histories both in shape and magnitude. The second set of seed values resulted in deflection time histories that are similar in shape but reduced in magnitude when compared to the true ones. The last set of seed values resulted in the poorest deflection time histories both in terms of shape and magnitude.

The backcalculation was initiated using the Gauss-Newton method. As shown by the RMSE histories in Figure 7-10, the first, second, and third sets of seed values converged after 17, 42, and 39 iterations, respectively. The respective backcalculation was switched over to the Levenberg-Marquardt method after 13, 1, and 2 iterations. The deflection time histories obtained after backcalculation are shown in Figure 7-11. Both Figure 7-10 and Figure 7-11 indicate that the first set of seed values were most successful followed by the second set, and that the third set converged to a wrong solution.

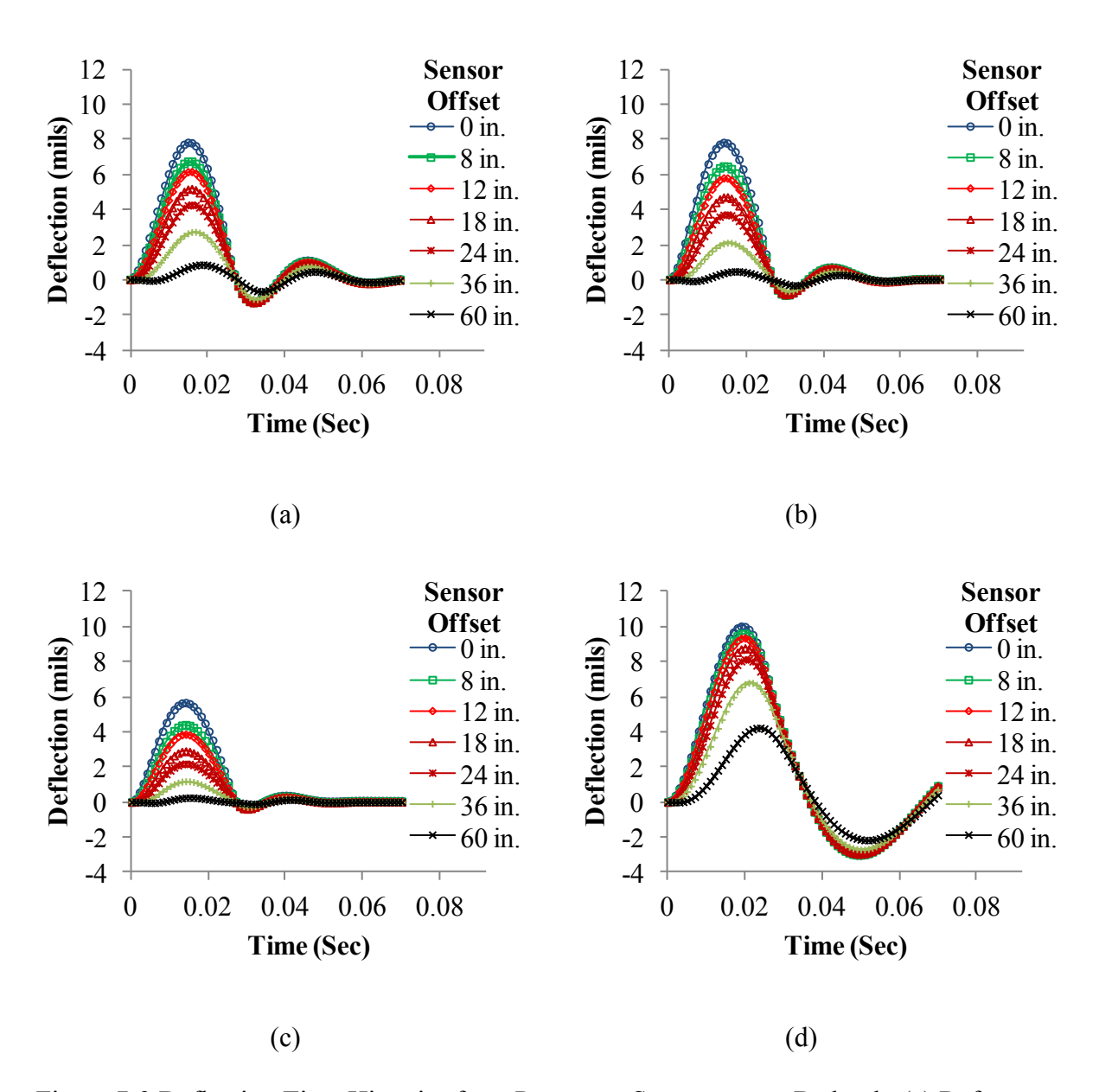


Figure 7-9 Deflection Time Histories from Pavement Structure on a Bedrock; (a) Reference Pavement, (b) Seed Set 1, (c) Seed Set 2, and (d) Seed Set 3

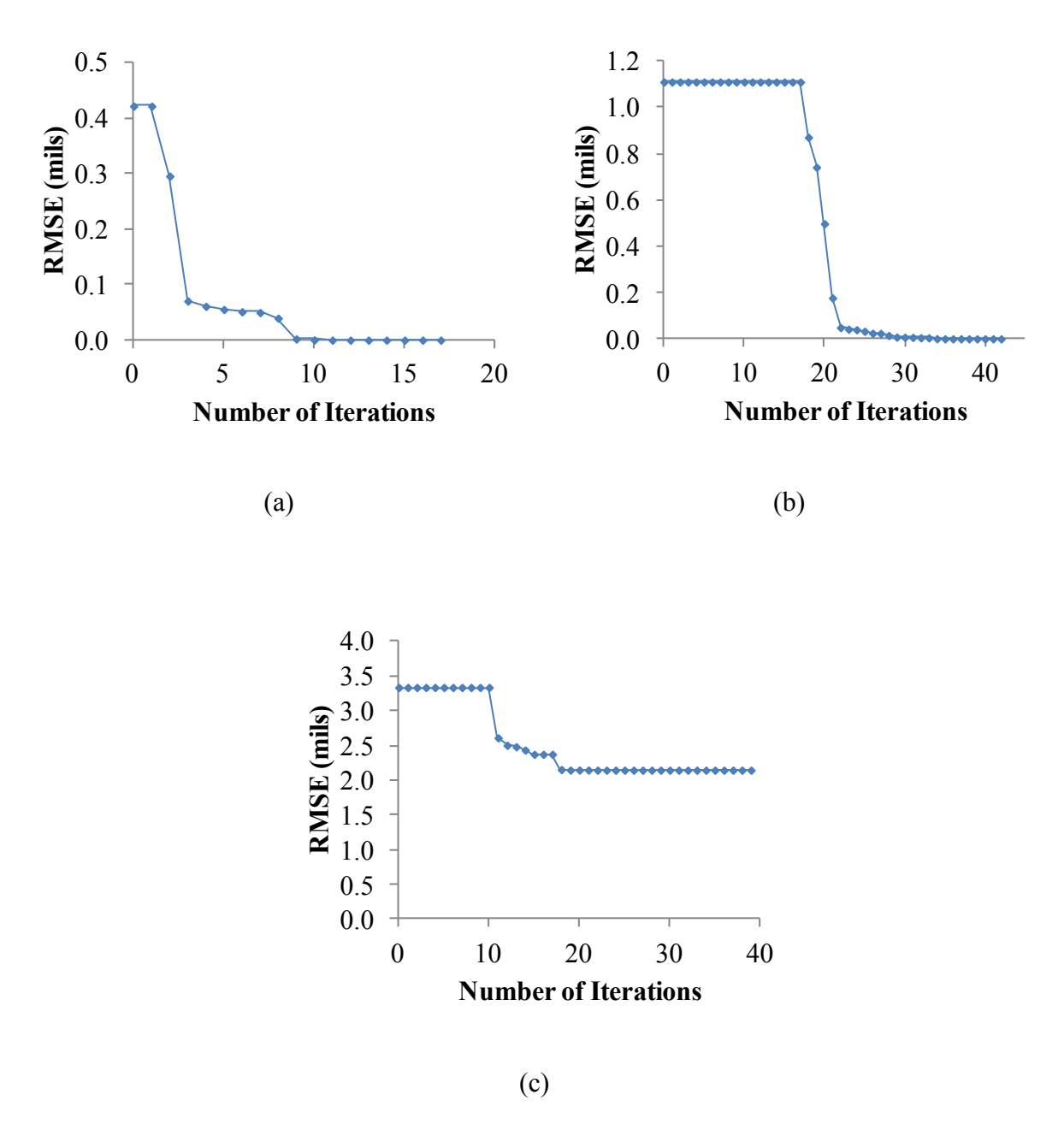


Figure 7-10 History of Root Mean Square Error for (a) Seed Set 1, (b) Seed Set 2, and (c) Seed Set 3

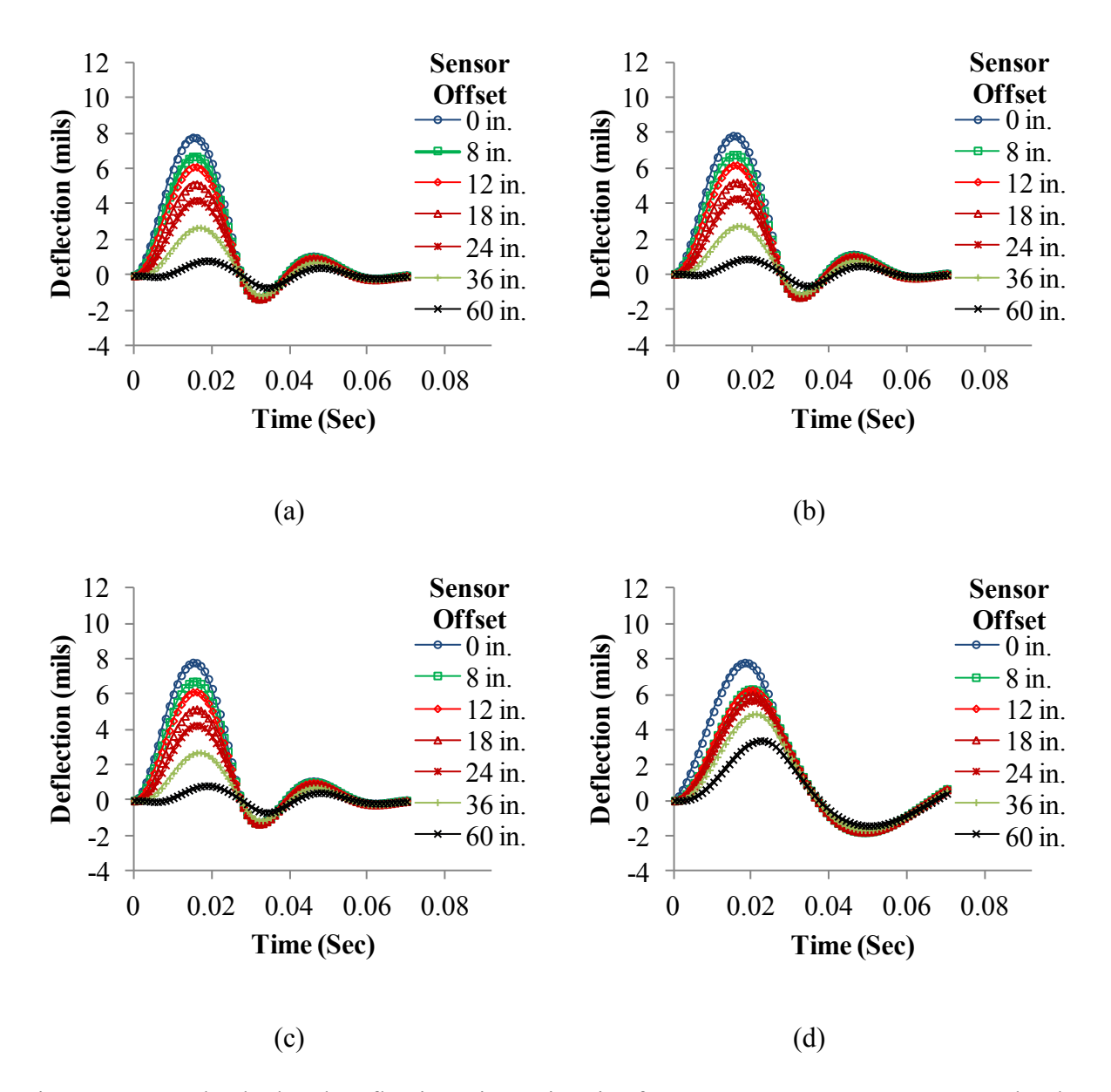


Figure 7-11 Backcalculated Deflection Time Histories from Pavement Structure on a Bedrock; (a) Reference Pavement, (b) Seed Set 1, (c) Seed Set 2, and (d) Seed Set 3

The backcalculated results for all sets of seed values are summarized in Table 7-4 which shows that the first and second sets of seeds were able to backcalculate the true values with reasonable errors. The third set of seed values converged to a wrong solution, as clearly seen by the negative power function parameters and the minimal improvement in the unbound layer modulus from the seed values. Again, these observations confirm that the Gauss-Newton method that was used for backcalculation is sensitive to the seed values. The convergence histories shown in Figure 7-12 through Figure 7-24 confirm the above observations.

Table 7-4 Backcalculated Values and Percent Error – Pavement on a Bedrock

Variable	True Value	Backcalculated Value (Absolute Percent Error)			
v arrable	variable True value		Seed Set 2	Seed Set 3	
D ₀ (1/psi)	3.00E-07	2.96E-07 (1.2%)	3.01E-07 (0.4%)	5.93E-07 (-97.6%)	
D ₁ (1/psi)	5.00E-07	4.99E-07 (0.2%)	5.01E-07 (0.2%)	-5.11E-07 (202.3%)	
m	0.3	0.29 (2.5%)	0.30 (0.9%)	-0.01 (102.9%)	
E_{Base} (psi)	30,000	29,936 (0.2%)	30,049 (0.2%)	5,989 (80.0%)	
$E_{ m Subgrade}$ (psi)	15,000	15,007 (0.1%)	14,998 (0.01%)	3,000 (80.0%)	

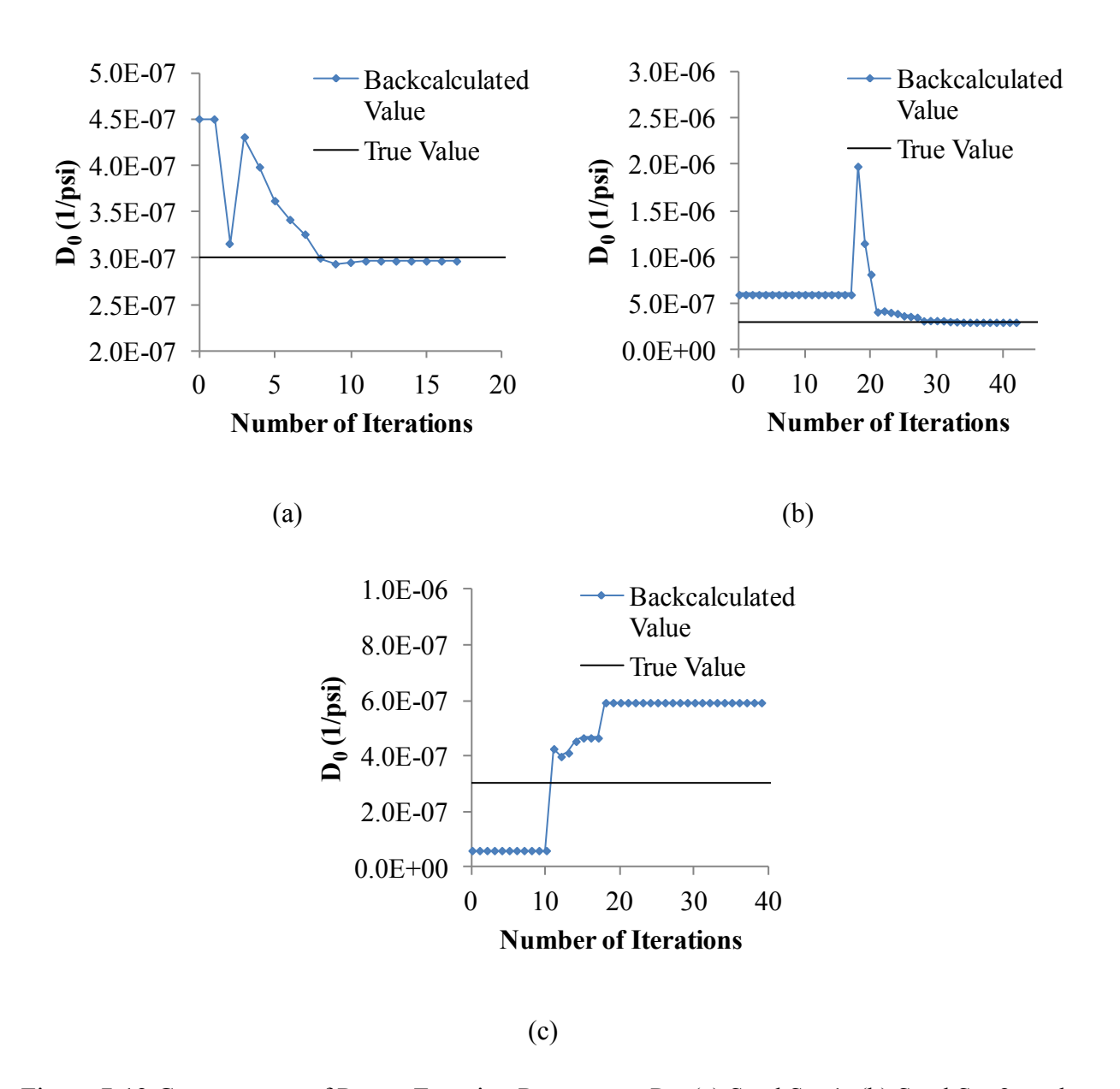


Figure 7-12 Convergence of Power Function Parameters D_0 ; (a) Seed Set 1, (b) Seed Set 2, and (c) Seed Set 3 – Pavement Structure on a Bedrock

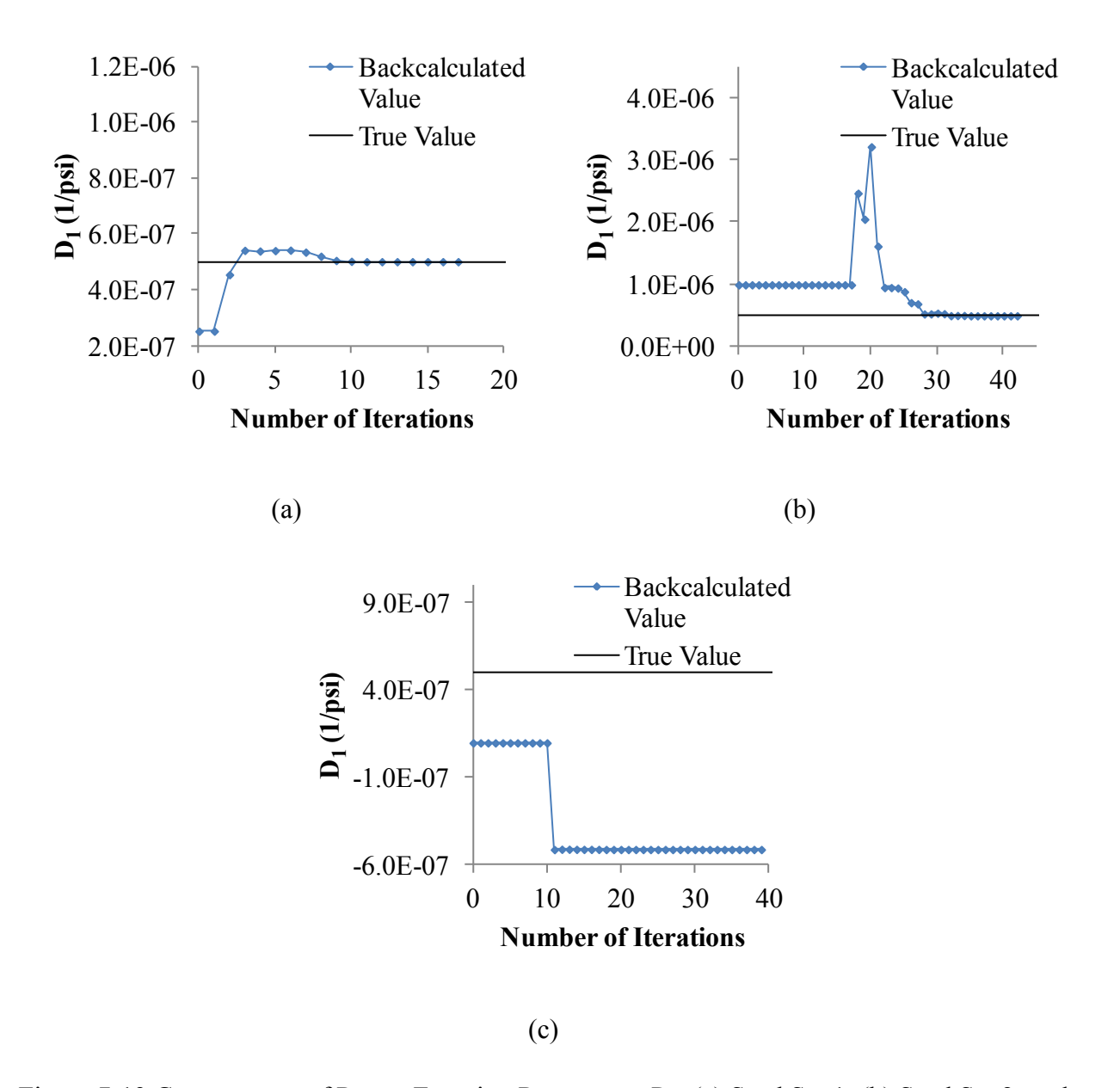


Figure 7-13 Convergence of Power Function Parameters D_1 ; (a) Seed Set 1, (b) Seed Set 2, and (c) Seed Set 3 – Pavement Structure on a Bedrock

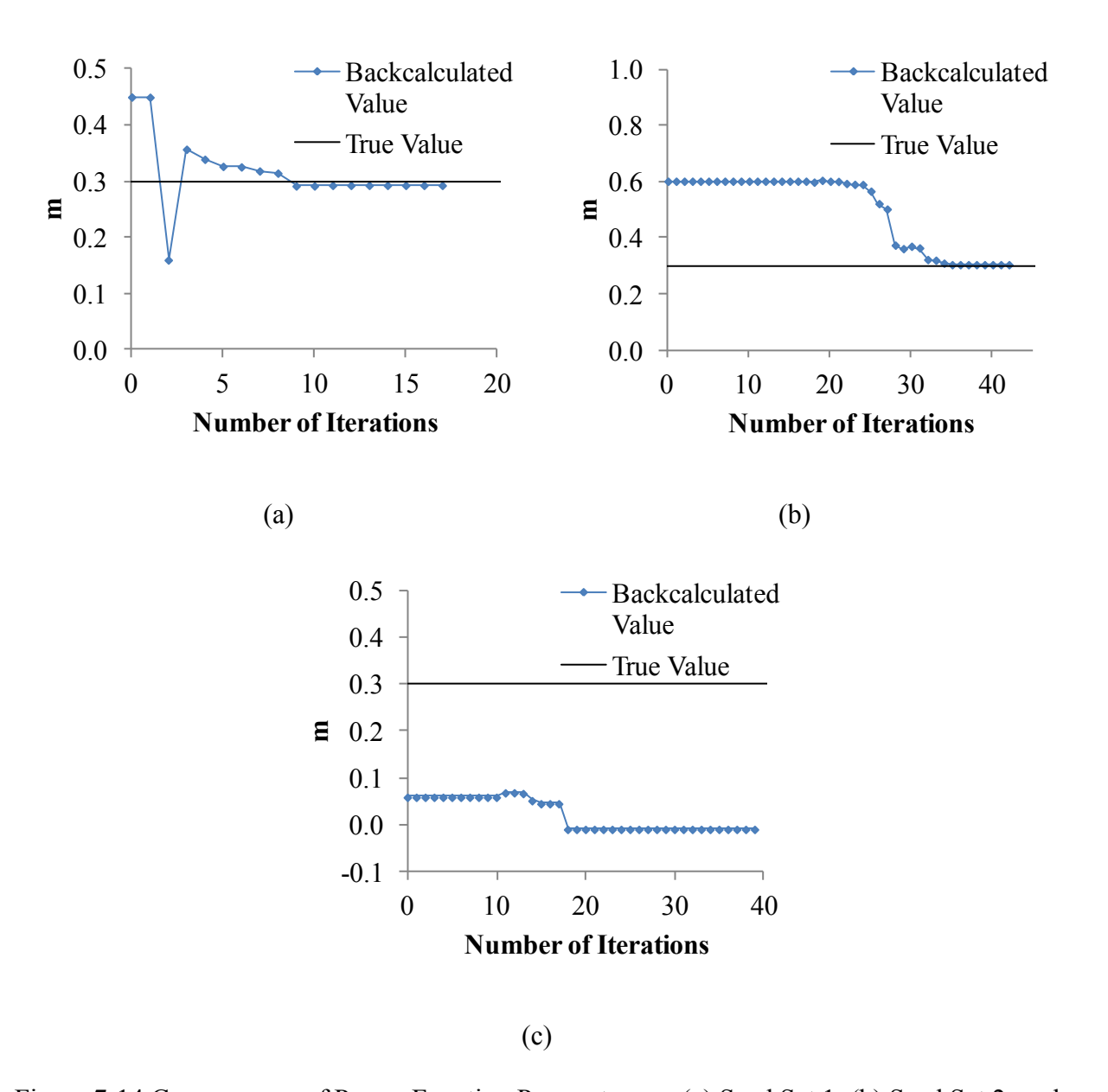


Figure 7-14 Convergence of Power Function Parameters *m*; (a) Seed Set 1, (b) Seed Set 2, and (c) Seed Set 3 – Pavement Structure on a Bedrock

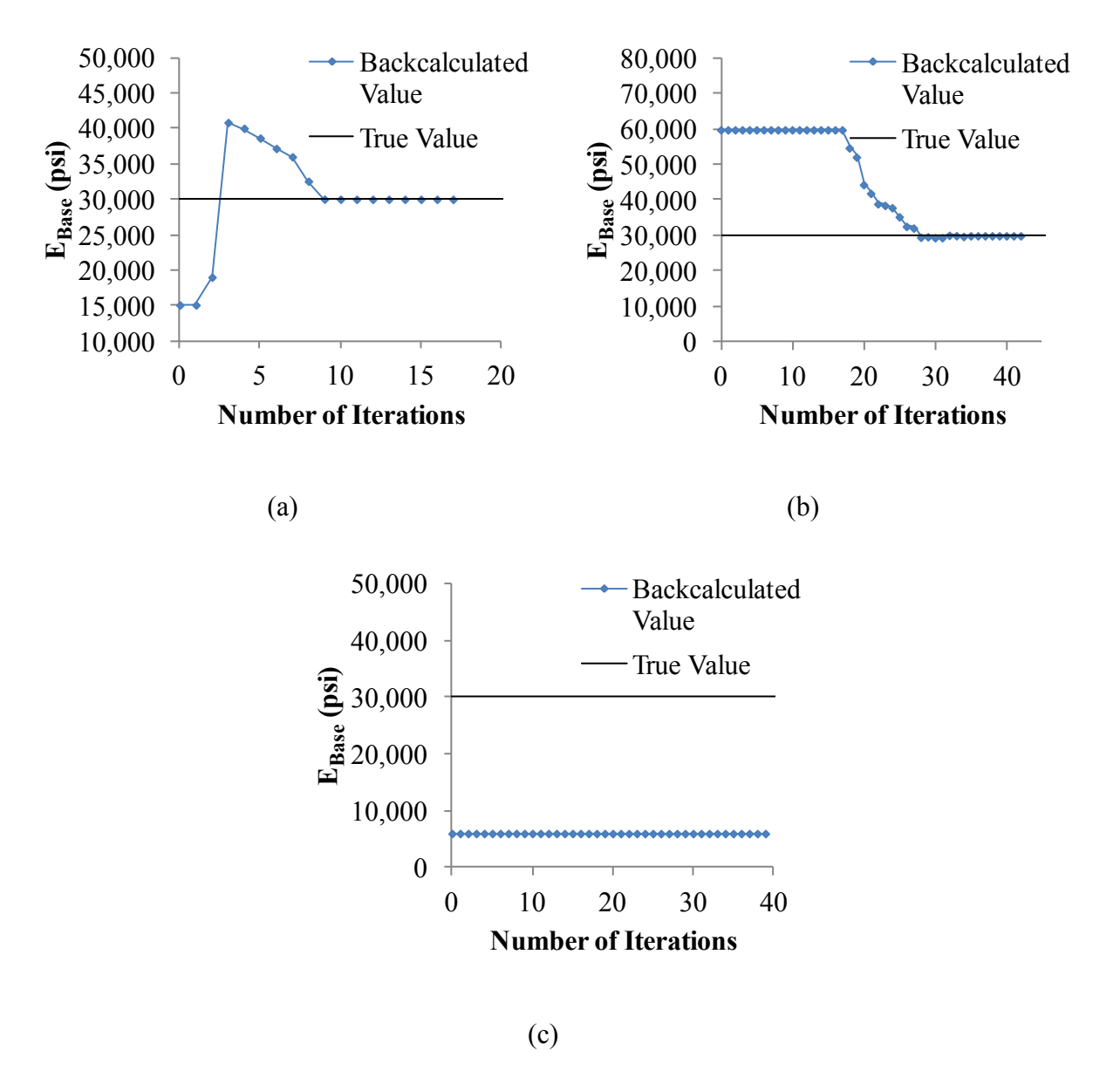


Figure 7-15 Convergence of Base Modulus; (a) Seed Set 1, (b) Seed Set 2, and (c) Seed Set 3 – Pavement Structure on a Bedrock

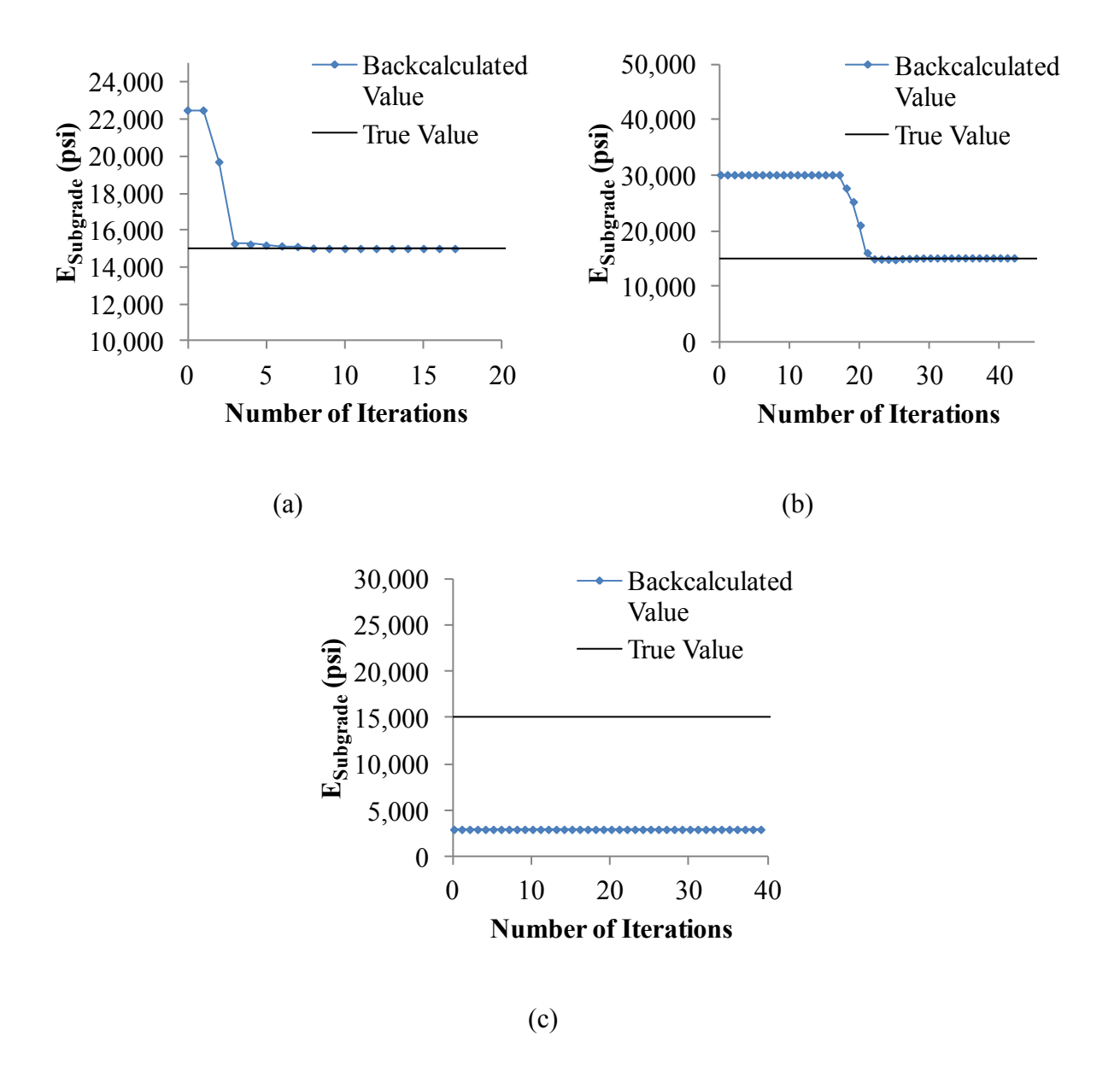


Figure 7-16 Convergence of Subgrade Modulus; (a) Seed Set 1, (b) Seed Set 2, and (c) Seed Set 3 – Pavement Structure on a Bedrock

7.2.2. Multi-Temperature Backcalculation

7.2.2.1. Theoretical Development of Generalized Power Function Relationship at Multiple Temperatures

The purpose of the theoretical backcalculation at multiple temperatures is to study if the dynamic modulus mastercurve can be obtained for a broader range of time (or frequency) and more accurately from the FWD time histories. As such, it is important to understand how the generalized power function used in ViscoWave behaves theoretically under the time-temperature superposition principle. The theoretical development is provided in this section of the report in a brief manner.

Rewriting Equation (3-27) given for the generalized power function in terms of the reduced time, ξ , results in:

$$D(\xi) = D_0 + D_1 \cdot \xi^m \tag{7-18}$$

Upon substituting the Equation (3-23) into above, the following is obtained.

$$D(\xi) = D_0 + D_1 \cdot \left(\frac{t}{a_T}\right)^m = D_0 + D_1^T \cdot t^m$$
 (7-19)

where,

$$D_1^T(T) = \frac{D_1}{a_T(T)^m} \tag{7-20}$$

The above equations reveal that D_1 is the only parameter affected by the change in material temperature and the other parameters D_0 and m remain constant irrespective of temperature. In addition, the above equations also indicate that if the creep compliances of a viscoelastic material at multiple temperatures are given in terms of generalized power functions, the shift factors can easily be obtained through Equation (7-20), since the parameter m does not vary with temperature.

7.2.2.2. Reference Pavement Structures and Seed Values for Backcalculation

For the multiple temperature backcalculation exercise, the FWD time histories were first obtained for a couple of pavement structures (with and without halfspace) exposed to four different temperatures: 0° C, 10° C, 20° C, and 40° C. The D_1 values for the viscoelastic asphalt material corresponding to these temperatures are summarized in Table 7-5 along with the other properties used for generating the time histories. Figure 7-17 and Figure 7-18 show the shift factors that were used to obtain the D_1 values and the creep compliance curves at the above mentioned temperatures, respectively. The properties of the base and subgrade layers with and without a halfspace are summarized in Table 7-6. The pavement structures were imposed to a half-sine load with the same characteristics provided in the previous section for the single temperature backcalculation. The surface deflection time histories were again obtained at radial distances of 0 in., 8 in., 12 in., 18 in., 24 in., 36 in., and 60 in. from the center of the loading plate.

Table 7-5 Asphalt Properties Used for Reference Pavement Structures

Temp(°C)	D ₀ (1/psi)	D ₁ (1/psi)	m	Poisson's Ratio	Density (pcf)	Thickness (in.)
0		7.52E-06				
10	1.01E-07	1.74E-05	0.27	0.35	145	6
20	1.01E-07	3.82E-05	0.27	0.55	143	6
40		1.57E-04				

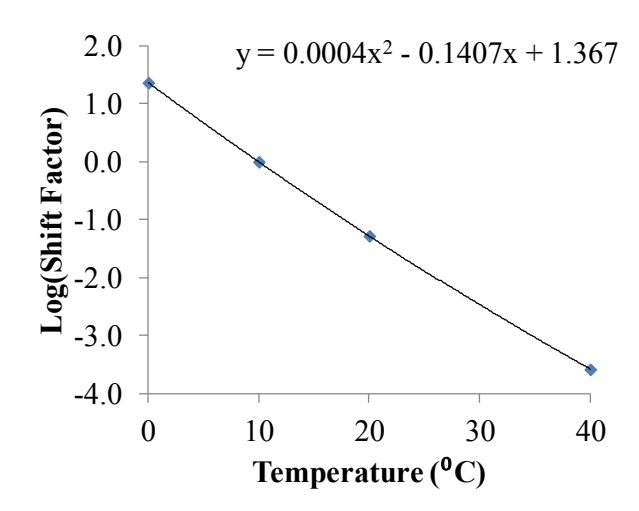


Figure 7-17 Time-Temperature Shift Factors

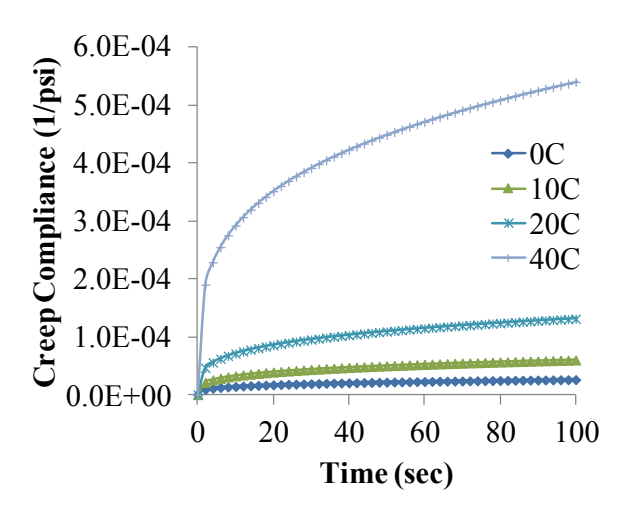


Figure 7-18 Creep Compliance Curves at Multiple Temperatures

Table 7-6 Base and Subgrade Properties Used for Reference Pavement Structures

Layer	Elastic Modulus (psi)	Poisson's Ratio	Density (pcf)	Thickness (in.)
Base	30,000	0.4	125	12
Subgrade	15,000	0.45	100	$\infty^1/60^2$

Note 1: For pavement with a halfspace

Note 2: For pavement with a bedrock

Table 7-7 summarizes the seed values used for backcalculation. Although the D_1 parameter was dependent on temperature, a single seed value was assigned regardless of temperature.

Table 7-7 Seed Values Used for Backcalculation

Variable	Temperature (°C)	Seed Value	Percent Increase from True Value
D ₀ (1/psi)	N/A	1.52E-06	50.0%
	0		15.9%
D ₁ (1/psi)	10	8.71E-06	-50.0%
	20	6./1E-00	-77.2%
	40		-94.5%
m	N/A	0.4	50.0%
E_{Base} (psi)	N/A	15,000	-50.0%
$E_{ m Subgrade}$ (psi)	N/A	22,500	50.0%

7.2.2.3. Backcalculation Results for Pavement Structure With a Halfspace

Figure 7-19 shows the deflection time histories of the reference pavement for all temperatures. The seed deflection history that was used regardless of temperature is shown in Figure 7-20. It is

also noted that the seed deflection time histories resemble the shape of the true time histories reasonably well.

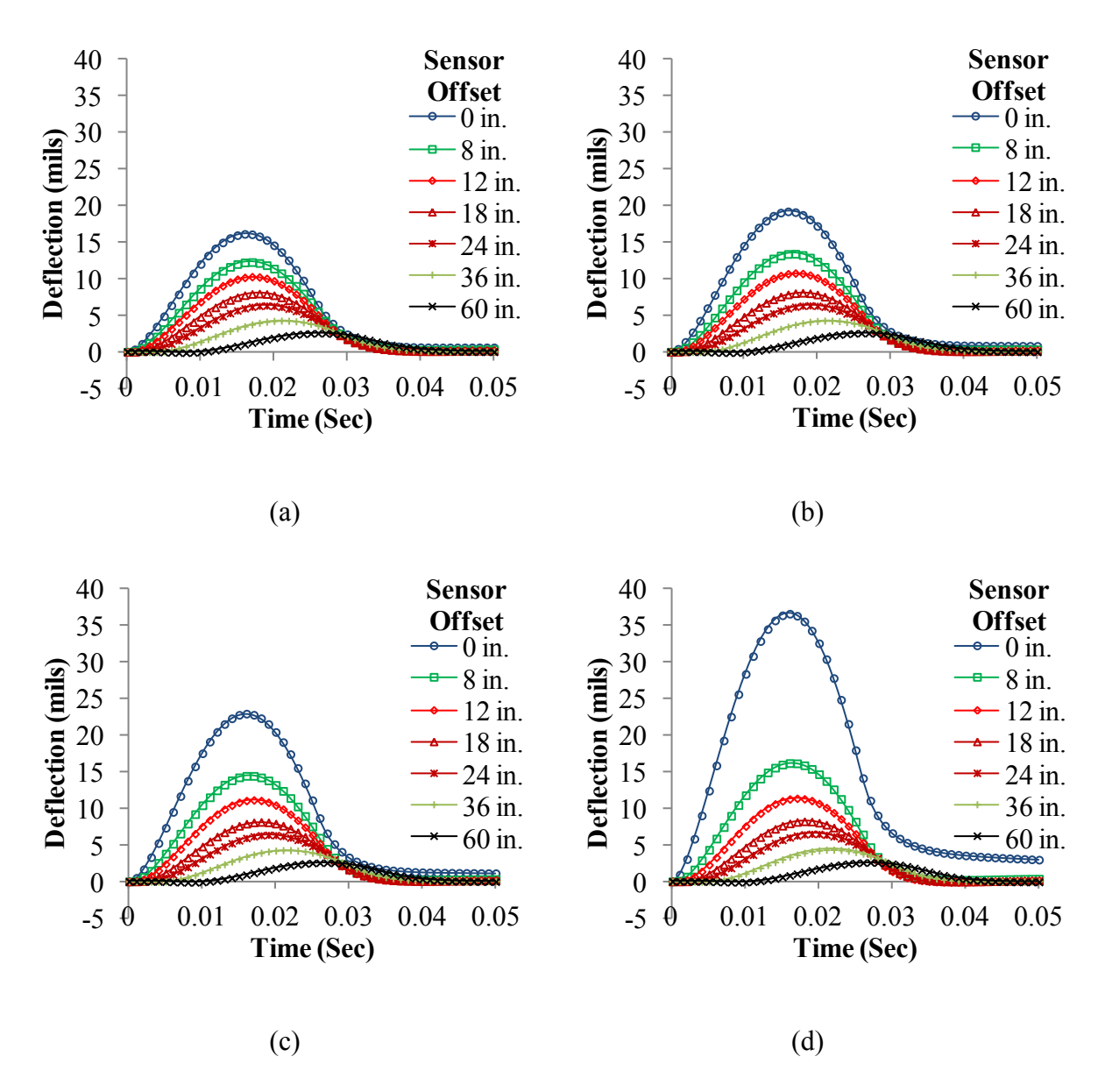


Figure 7-19 Simulated FWD Deflection Time Histories for (a) 0° C, (b) 10° C, (c) 20° C, and (d) 40° C

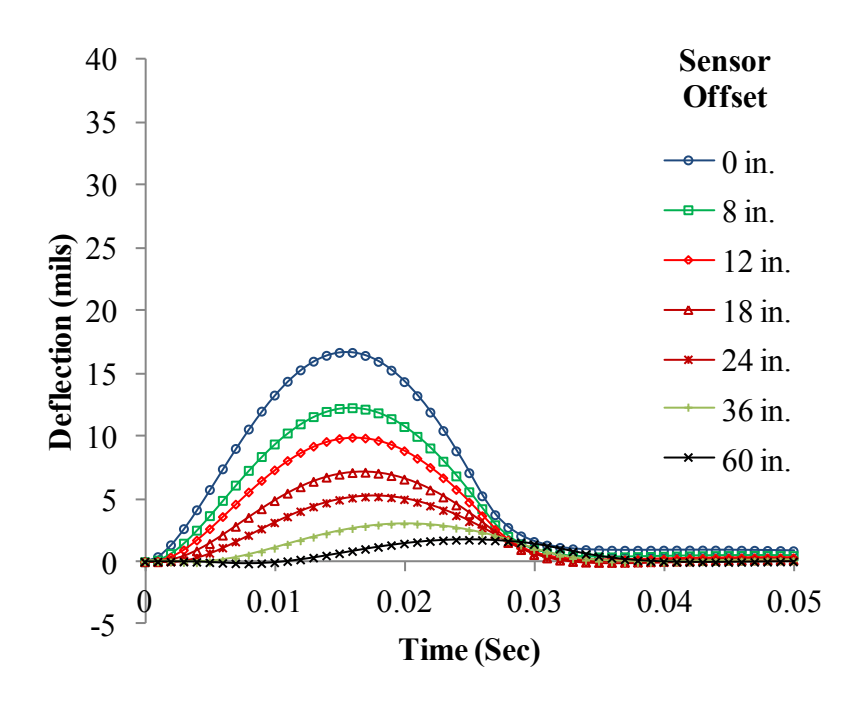


Figure 7-20 Seed FWD Deflection Time History for All Temperatures

The backcalculation was terminated after 18 iterations for which the Gauss-Newton method was used throughout. Figure 7-21 shows the history of RMSE and Table 7-8 summarizes the backcalculated values and their respective errors. The table shows that the backcalculation was successful, with the percent errors for all variables being less than 0.001 percent expect for the *m* value which showed an error of 1.1 percent.

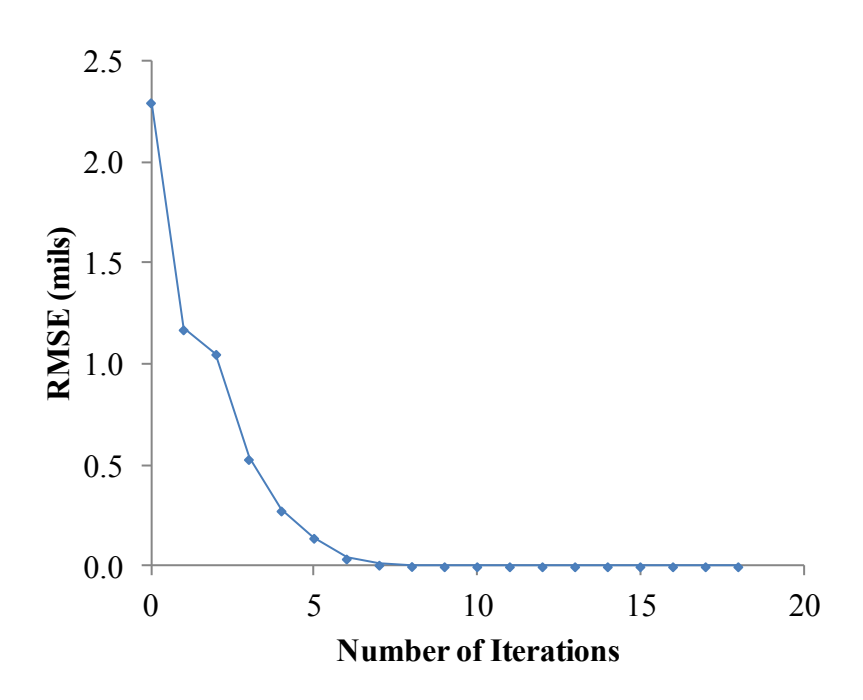


Figure 7-21 History of Root Mean Square Error

Table 7-8 Backcalculated Values and Percent Error – Pavement on a Halfspace

Variable	Temperature (°C)	True Value	Backcalculated Value	Absolute Percent Error
D ₀ (1/psi)	N/A	1.01E-07	1.01E-07	<0.001%
	0	7.52E-06	7.52E-06	<0.001%
D (1/ngi)	10	1.74E-05	1.74E-05	<0.001%
D_1 (1/psi)	20	3.82E-05	3.82E-05	<0.001%
	40	1.57E-04	1.57E-04	<0.001%
m	N/A	0.27	0.27	1.1%
E_{Base} (psi)	N/A	30,000	30,000	<0.001%
$E_{ m Subgrade}$ (psi)	N/A	15,000	15,000	<0.001%

The convergence history of the viscoelastic parameters are shown in Figure 7-22 while those for the base and subgrade layers are shown in Figure 7-23.

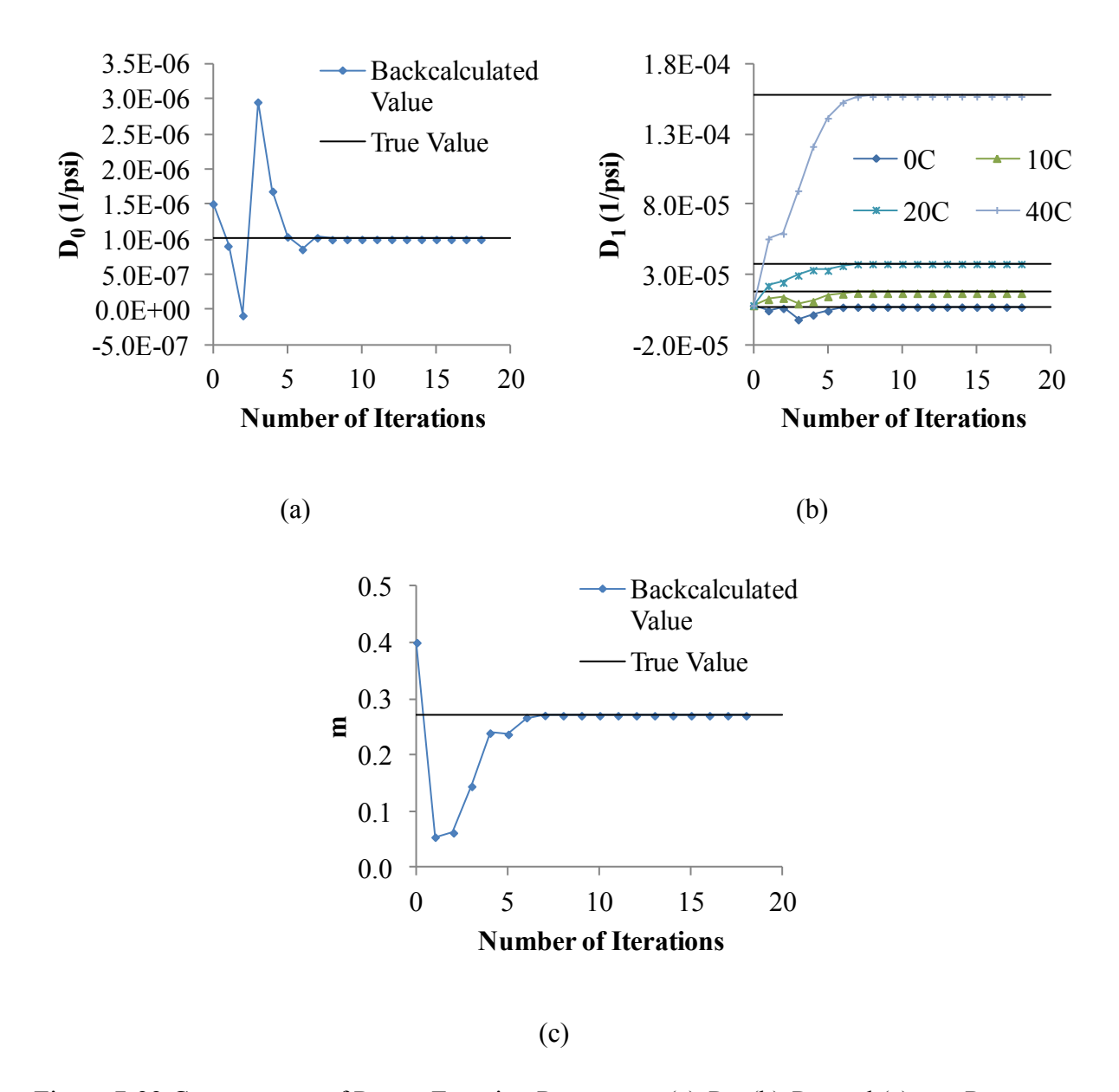


Figure 7-22 Convergence of Power Function Parameters (a) D_0 , (b) D_1 , and (c) m – Pavement Structure on a Halfspace

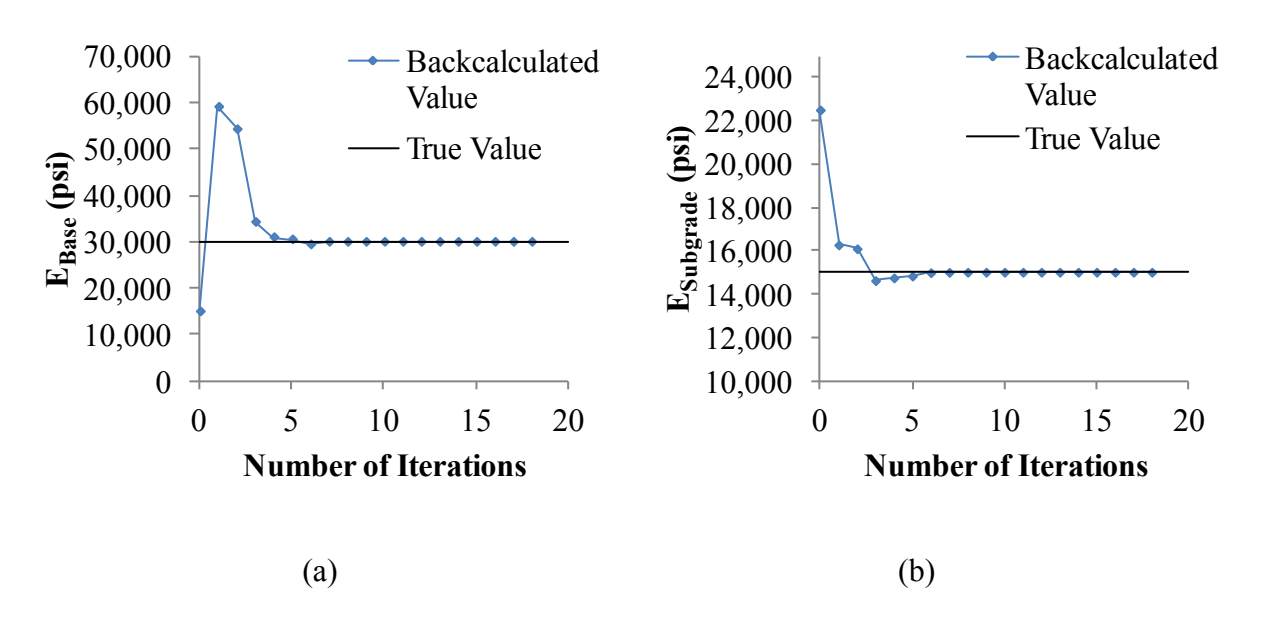


Figure 7-23 Convergence of (a) Base and (b) Subgrade Layer Moduli – Pavement Structure on a Halfspace

7.2.2.4. Backcalculation Results for Pavement Structure on a Bedrock

Figure 7-24 shows the deflection time histories using ViscoWave for all temperatures. The seed deflection history that was used regardless of temperature is shown in Figure 7-25. Note that the free vibration is present in all deflection time histories shown in Figure 7-24 including those generated for 40°C. However, the deflection histories generated with the seed values did not show any free vibration. Such discrepancies in the shape of the deflection time histories may cause the solution some additional iterations to converge.

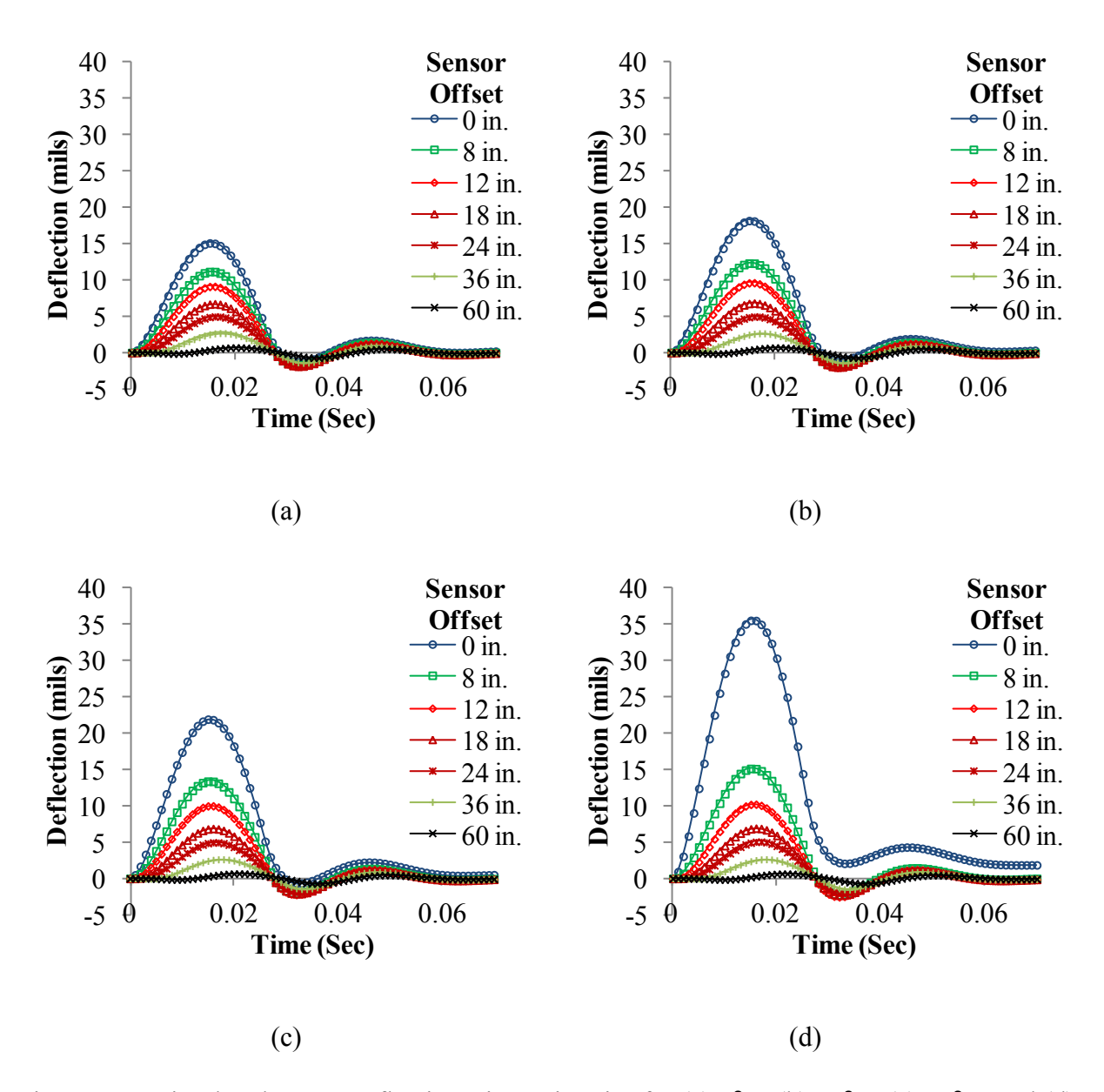


Figure 7-24 Simulated FWD Deflection Time Histories for (a) 0° C, (b) 10° C, (c) 20° C, and (d) 40° C

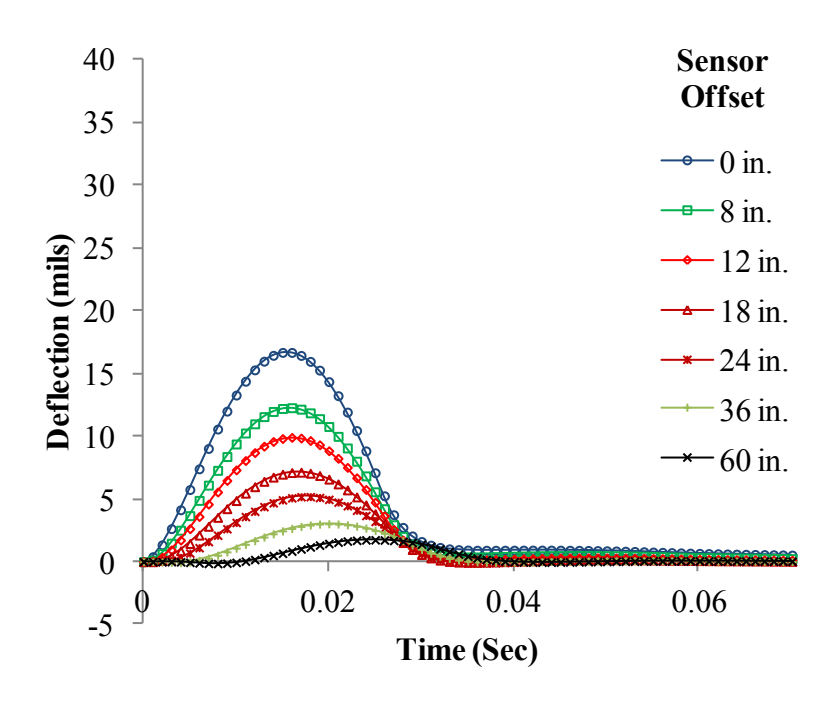


Figure 7-25 Seed FWD Deflection Time History for All Temperatures

The backcalculation converged and was terminated after 26 iterations. As expected, the 7 additional iterations when compared to the case with a halfspace, are believed to be due to the seed deflection time histories not showing any free vibration (i.e., the shape of the deflection time histories not resembling the true ones). As was the case with the pavement on a halfspace, the Gauss-Newton method was used throughout the backcalculation process, without switching over to the Levenberg-Marquardt method. Figure 7-26 shows the history of RMSE and Table 7-9 summarizes the backcalculated values and their respective errors Again, the percent errors for all variables were less than 0.001 percent except for the *m* value. The convergence histories for the asphalt and the unbound layers are shown in Figure 7-27 and Figure 7-28, respectively.

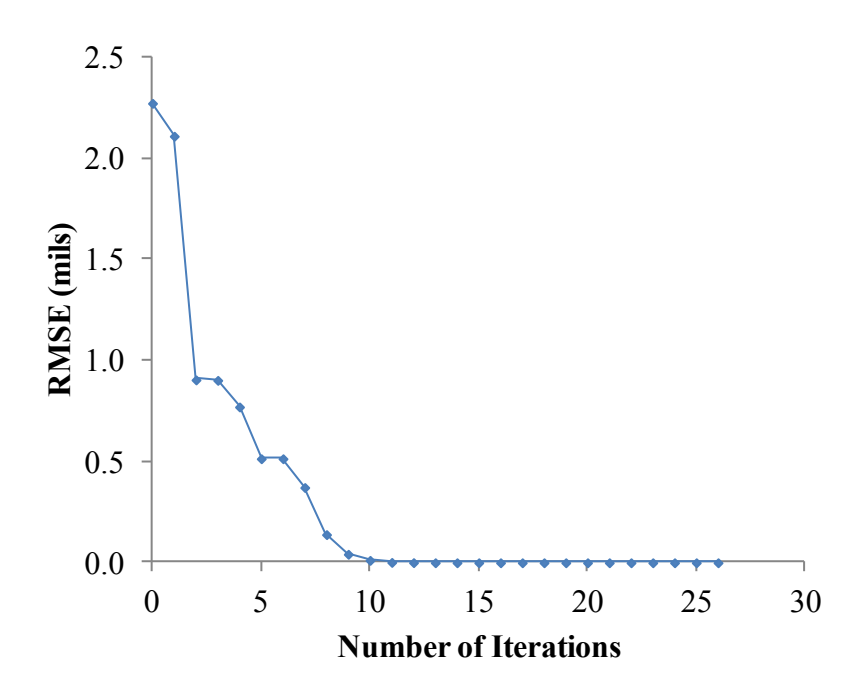


Figure 7-26 History of Root Mean Square Error

Table 7-9 Backcalculated Values and Percent Error – Pavement on a Halfspace

Variable	Temperature (°C)	True Value	Backcalculated Value	Absolute Percent Error
D ₀ (1/psi)	N/A	1.01E-07	1.01E-07	<0.001%
	0	7.52E-06	7.52E-06	<0.001%
D (1/n si)	10	1.74E-05	1.74E-05	<0.001%
D_1 (1/psi)	20	3.82E-05	3.82E-05	<0.001%
	40	1.57E-04	1.57E-04	<0.001%
m	N/A	0.27	0.27	1.1%
E_{Base} (psi)	N/A	30,000	30,000	<0.001%
$E_{ m Subgrade}$ (psi)	N/A	15,000	15,000	<0.001%

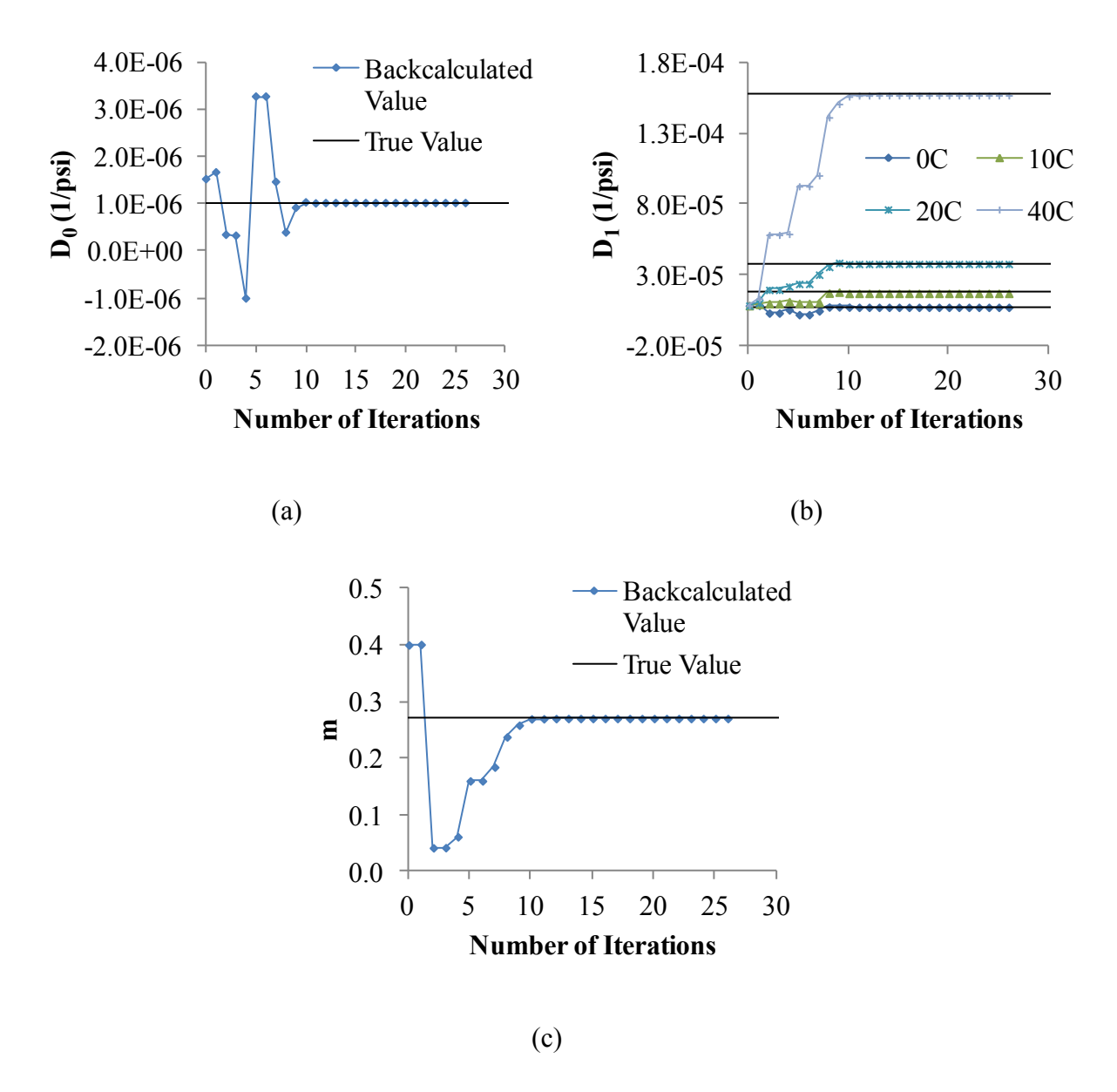


Figure 7-27 Convergence of Power Function Parameters (a) D_0 , (b) D_1 , and (c) m – Pavement Structure on a Bedrock

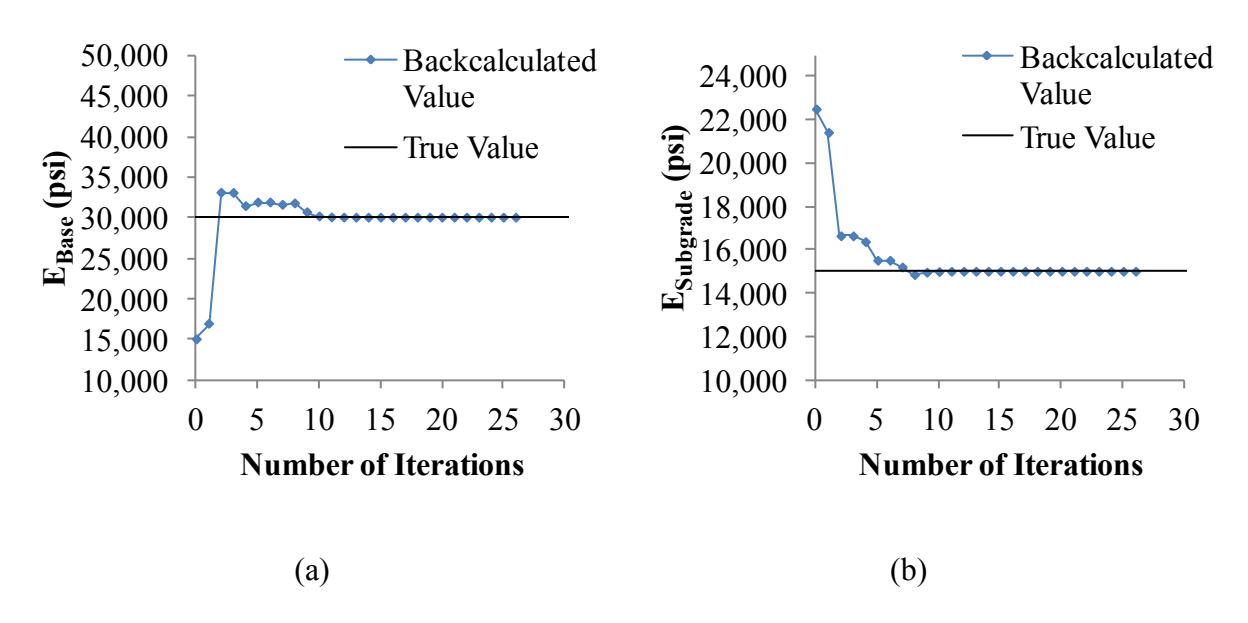


Figure 7-28 Convergence of (a) Base and (b) Subgrade Layer Moduli – Pavement Structure on a Bedrock

CHAPTER 8 - FIELD BACKCALCULATION USING VISCOWAVE

In this chapter, the ViscoWave algorithm and the optimization routines described in previous chapters will be used for backcalculating the pavement properties using the FWD data collected in the field and the results will be compared to those obtained in the laboratory.

8.1. Test Site and Protocol

The tested pavement was part of the Accelerated Pavement Test (APT) tracks in the State Materials Office (SMO) facility of the Florida Department of Transportation (FDOT). The pavement consisted of a 6.5 in. asphalt surface layer on top of a 10 in. limerock base. The asphalt mixture included a PG-76-22 polymer modified binder which is typically used in regular FDOT projects. The FWD testing was conducted in June of 2010 and the pavement cores were sampled immediately after the FWD tests. According to the measurements made at several monitoring wells installed around the APT facility, it was found that the ground water table at the time of FWD testing was located approximately 11.0 ft to 11.5 ft. below the surface.

8.2. Laboratory Dynamic Modulus Test

As was mentioned in Chapter 4 of the report, although the uniaxial tension or compression test is desirable for testing of the viscoelastic materials, the problem associated with size requirements (4 in. diameter and 6 in. thickness) frequently makes it impossible, especially on cored mixtures from thin asphalt layers. As an alternative to the uniaxial test, the dynamic modulus tests were

conducted in the IDT mode (as described in Chapter 4), with the adoption of the dynamic modulus testing procedure used in AASHTO TP 62.

A total of four field cores obtained from the test track and were delivered to the FDOT's asphalt laboratory. Each core was carefully cut to yield two IDT specimens (one of each from the top and the bottom lifts) with a diameter of 6.0 in. and a thickness of 1.5 in. To allow for generating the viscoelastic mastercurve, the dynamic modulus test was conducted at three distinct temperatures: 0°C, 10°C, and 20°C. For each temperature, the specimens were placed in the target temperature for at least 12 hours prior to the IDT tests. For each temperature, the dynamic modulus tests were then conducted at five frequencies: 0.1 Hz, 0.5 Hz, 1.0 Hz, 5.0 Hz, and 10.0 Hz. The resulting IDT dynamic modulus data was analyzed as described in Chapter 4 and the mastercurve was constructed according to the procedures shown in Chapter 3. Figure 8-1 shows the dynamic modulus mastercurve for both the top and the bottom lift at a reference temperature of 10°C while the corresponding shift factors are shown in Figure 8-2.

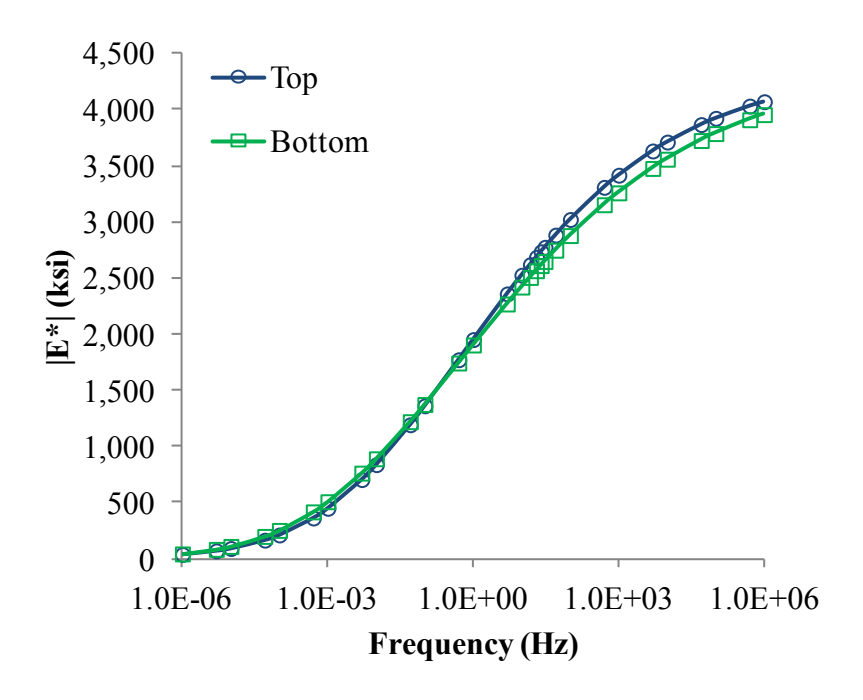


Figure 8-1 Laboratory Dynamic Modulus Mastercurves

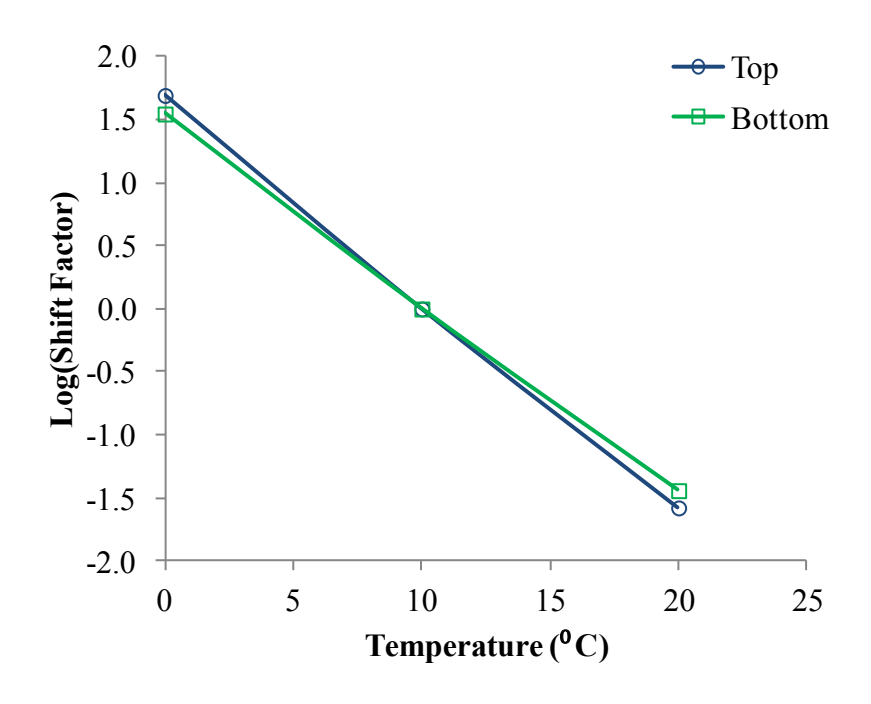


Figure 8-2 Laboratory Time-Temperature Shift Factors

8.3. FWD Backcalculation Using ViscoWave

The load and deflection time histories measured from the FWD is shown in Figure 8-3. Similar to the deflection time histories shown in Figure 7-19d, it is noted that due to the increased temperature of the asphalt at the time of FWD testing (58°C), the deflection measured at the center of the load plate did not return to zero.

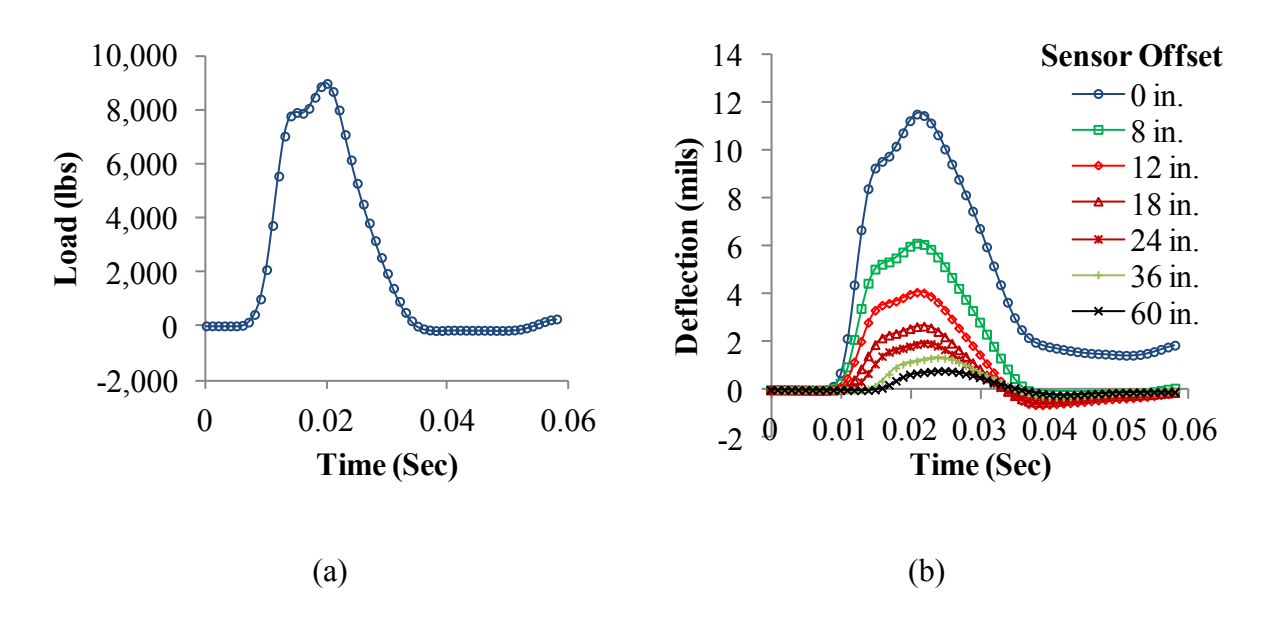


Figure 8-3 Measured FWD (a) Load and (b) Deflection Time Histories

The backcalculation was carried out in two folds: (1) with a 3 layer pavement system and (2) with a 5 layer pavement system to incorporate a ground water table at 11.3 ft. below the pavement surface. Table 8-1 shows the Poisson's ratio, material density and the thickness that was assumed for the backcalculation. The seed values for the generalized power function and the elastic moduli for the unbound layers are summarized in Table 8-2.

Table 8-1 Assumed Pavement Properties for Backcalculation

Lavar	Poisson's Ratio	Dangity (nof)	Thickness (in.)	
Layer	FOISSOII S Katio	Density (pcf)	3 Layer System	5 Layer System
Asphalt	0.35	145	6	.5
Base	0.35	125	1	0
Subgrade	0.40	115	∞	12
Emb. 1 ¹	0.45	110	N/A	108
Emb. 2 ¹	0.45	110	N/A	∞

Note 1: Only applicable to the 5 layer system.

Table 8-2 Seed Values Used for Backcalculation

Variable	Seed Value		
Variable	3 Layer System	5 Layer System	
D ₀ (1/psi)	5.00E-06		
D ₁ (1/psi)	2.0	0E-05	
m	0.60		
E_{Base} (psi)	80),000	
$E_{ m Subgrade}$ (psi)	32	2,000	
$E_{\text{Emb-1}} \left(\text{psi} \right)^1$	N/A	30,000	
$E_{\mathrm{Emb-2}}\left(\mathrm{psi}\right)^{1}$	N/A	30,000	

Note 1: Only applicable to the 5 layer system.

8.3.1. Backcalculation Results from the 3 Layer System

The backcalculation using the 3 layer system converged after 31 iterations with a terminal RMSE value of 0.23 mils. The history of the RMSE is shown in Figure 8-4 and the backcalculated values are summarized in Table 8-3.

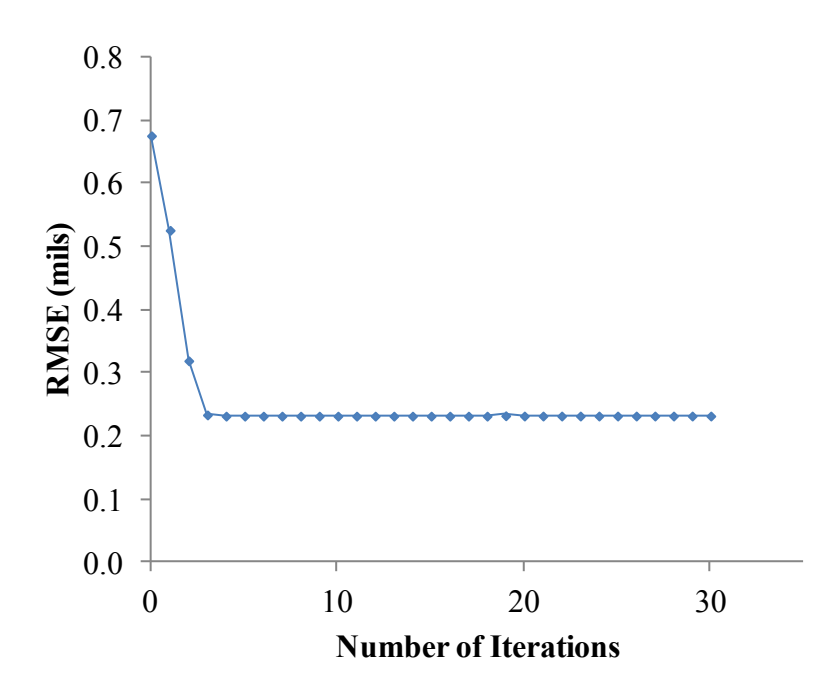
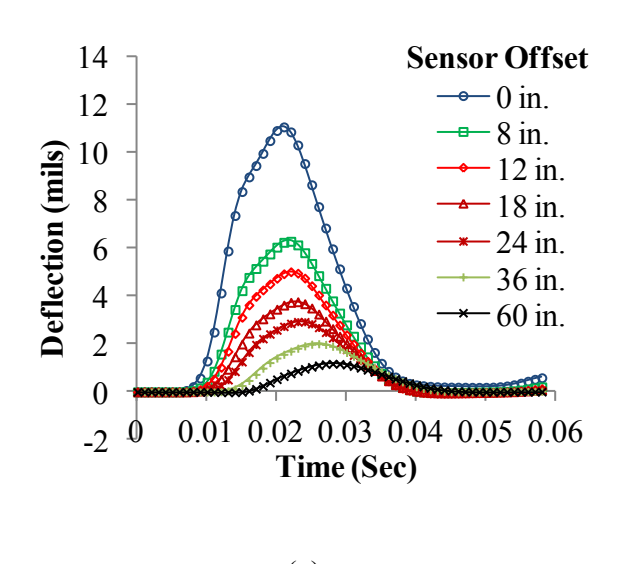


Figure 8-4 History of Root Mean Square Error for the 3 Layer System

Table 8-3 Backcalculated Values from 3 Layer System

Variable	Backcalculated Value
D ₀ (1/psi)	1.90E-06
D ₁ (1/psi)	1.02E-04
m	0.64
E_{Base} (psi)	32,732
$E_{ m Subgrade}$ (psi)	62,225

The time histories using the seed values as well as the backcalculated values are shown in Figure 8-5 which clearly shows that the backcalculated time histories are more comparable to the measured histories (Figure 8-3b) than the seed histories. Figure 8-6 and Figure 8-7 show the convergence histories for the viscoelastic parameters of the asphalt and the unbound layer moduli, respectively.



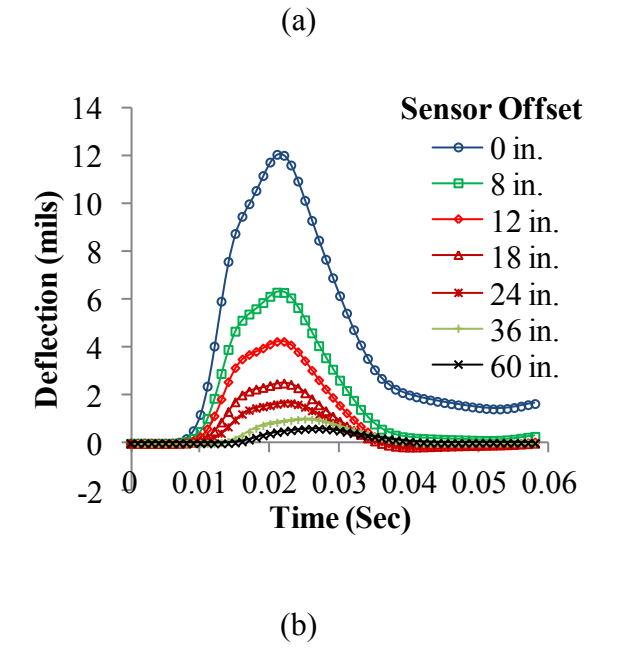


Figure 8-5 Simulated Time Histories for the 3 layer System with (a) Seed and (b) Backcalculated Values

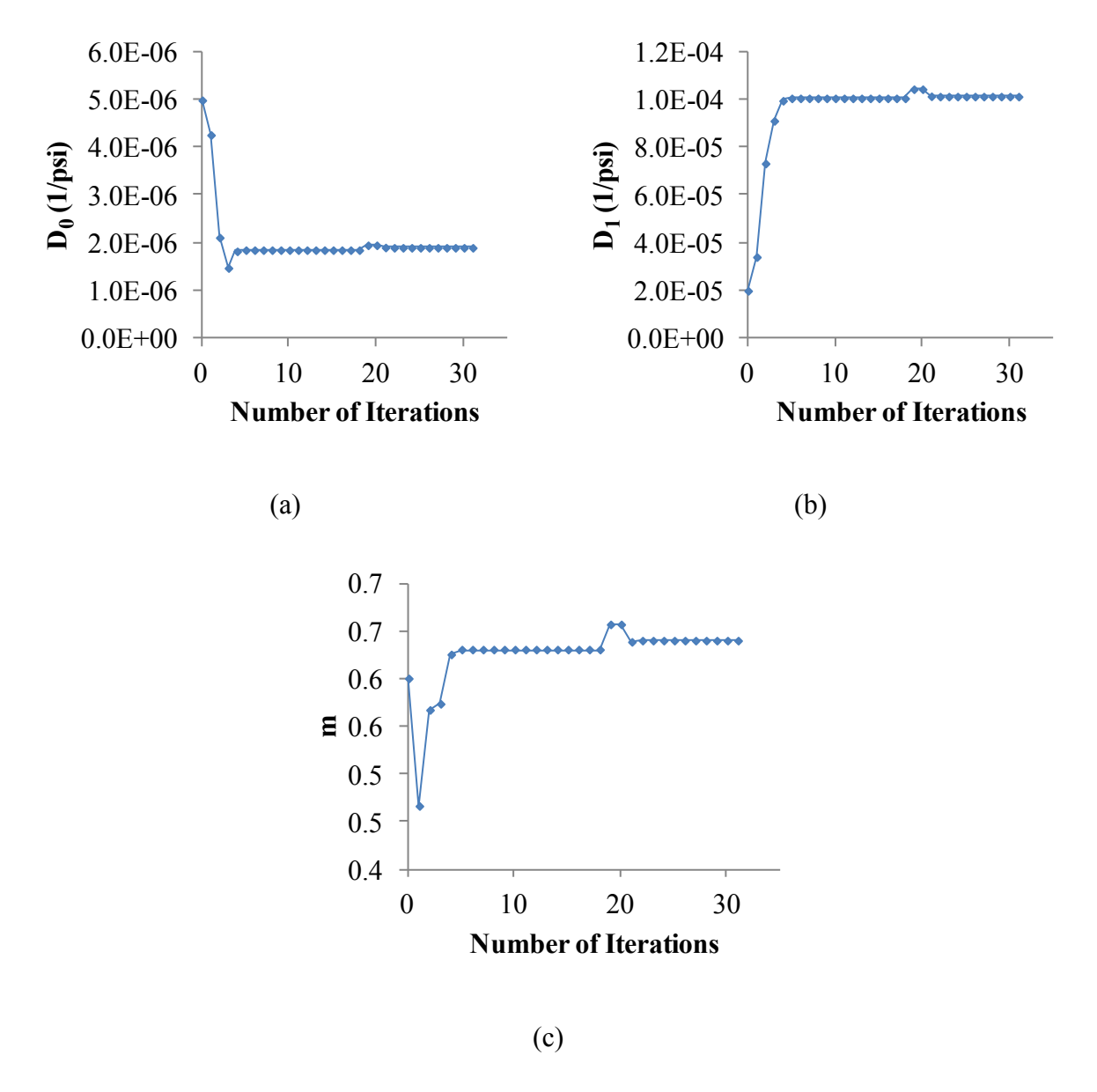


Figure 8-6 Convergence of Power Function Parameters (a) D_0 , (b) D_1 , and (c) m-3 Layer System

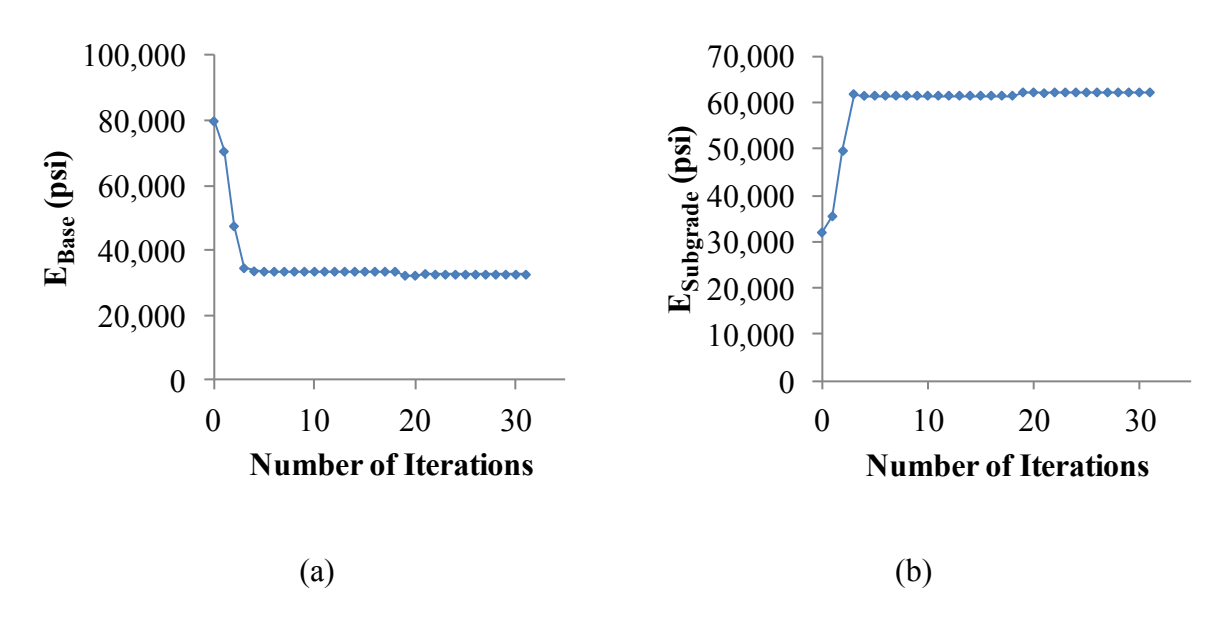


Figure 8-7 Convergence of Unbound Pavement Layer Moduli for the 3 Layer System (a) Base and (b) Subgrade

Figure 8-8 shows the seed and backcalculated creep compliance functions graphically. As can be seen from the figure, the backcalculated function shows the increased creep compliance which is most likely responsible for the viscoelastic response as shown by the delayed recovery of the deflection time histories in Figure 8-5b.

In order to compare the backcalculated viscoelastic parameters to those obtained from the laboratory, Prony series was fitted to the backcalculated creep compliance function and then converted to the dynamic modulus values following the procedures outlined in Chapter 3. Figure 8-9a shows the dynamic modulus mastercurve at 58°C with the laboratory mastercurve shifted to this temperature by extrapolating the shift factors shown in Figure 8-2. Figure 8-9b shows the same dynamic modulus mastercurve but at a reference temperature of 10°C with the backcalculated mastercurve shifted using the extrapolated laboratory shift factors. Both Figure

8-9a and Figure 8-9b show that the backcalculated dynamic modulus master curve is in good agreement with those obtained from the laboratory.

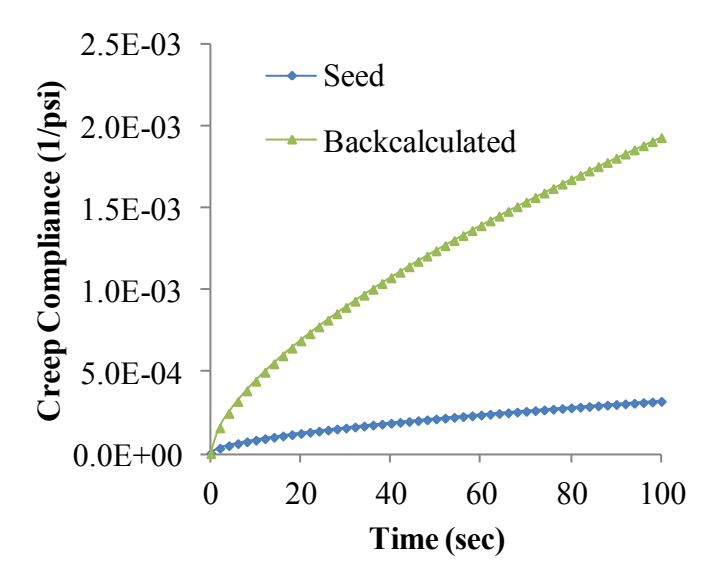


Figure 8-8 (a) Seed and (b) Backcalculated Creep Compliance Functions from 3 Layer System

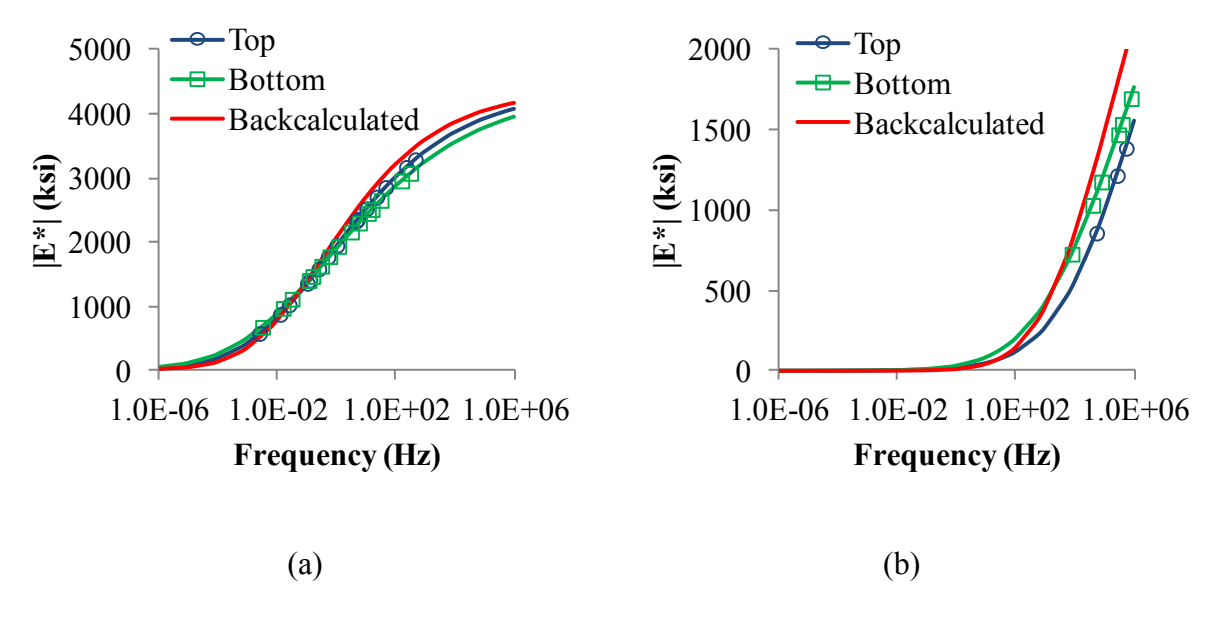


Figure 8-9 Backcalculated Dynamic Modulus Mastercurves at Reference Temperatures (a) 58°C and (b) 10°C – 3 Layer System

8.3.2. Backcalculation Results from the 5 Layer System

The backcalculation using the 5 layer system converged after 20 iterations with a terminal RMSE value of 0.18 mils. Compared to the 3 layer backcalculation results, this means that the 5 layer backcalculation resulted in a decrease of 0.05 mils in RMSE even with 11 less iterations. The history of the RMSE is shown in Figure 8-10 and the backcalculated values are summarized in Table 8-4.

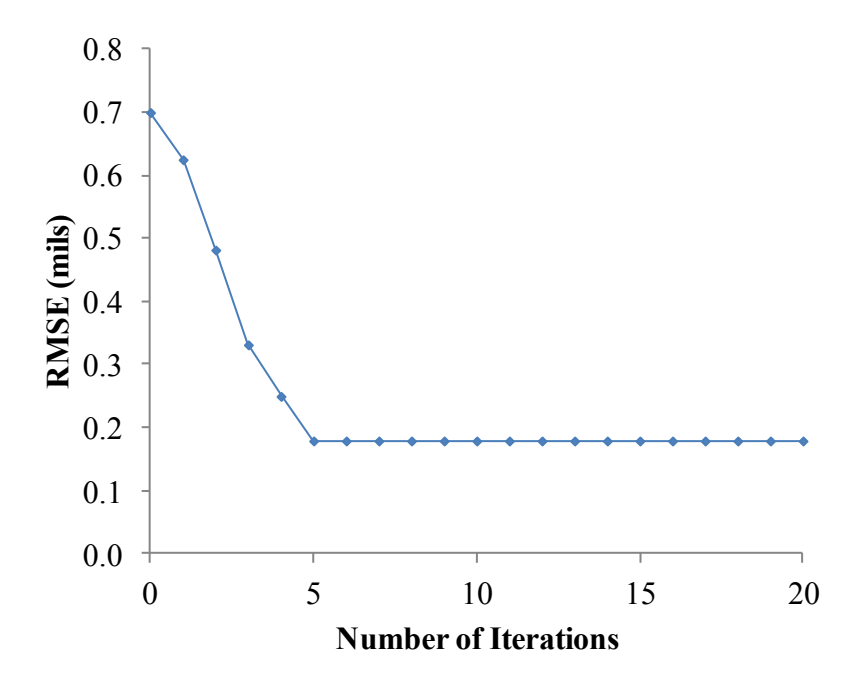


Figure 8-10 History of Root Mean Square Error for the 5 Layer System

Table 8-4 Backcalculated Values from 5 Layer System

Variable	Backcalculated Value
D ₀ (1/psi)	2.34E-06
D ₁ (1/psi)	1.20E-04
m	0.69
E_{Base} (psi)	29,199
$E_{ m Subgrade}$ (psi)	204,522
E _{Embankment 1} (psi)	44,390
E _{Embankment 2} (psi)	155,565

The time histories using the seed and the backcalculated values are shown in Figure 8-11. Again the backcalculated time histories clearly show the delayed recovery of the pavement system which is also seen in the measured time histories (Figure 8-3b). Figure 8-12 and Figure 8-13 show the convergence histories for the viscoelastic parameters of the asphalt and the unbound layer moduli, respectively.

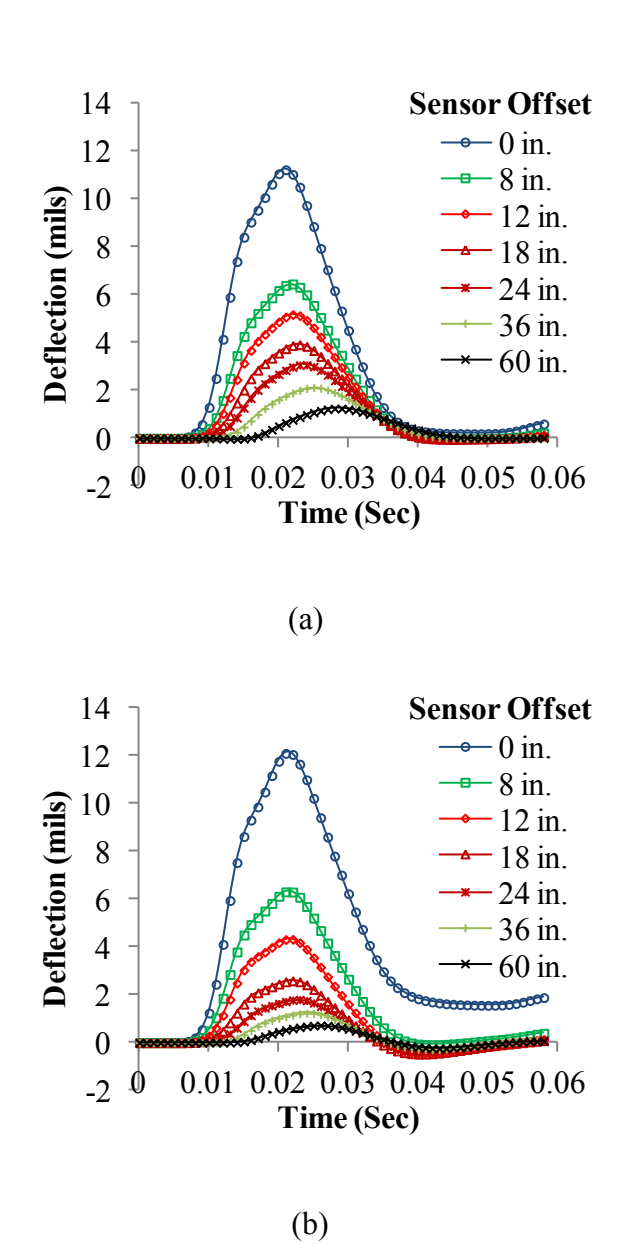


Figure 8-11 Simulated Time Histories for the 5 layer System with (a) Seed and (b)

Backcalculated Values

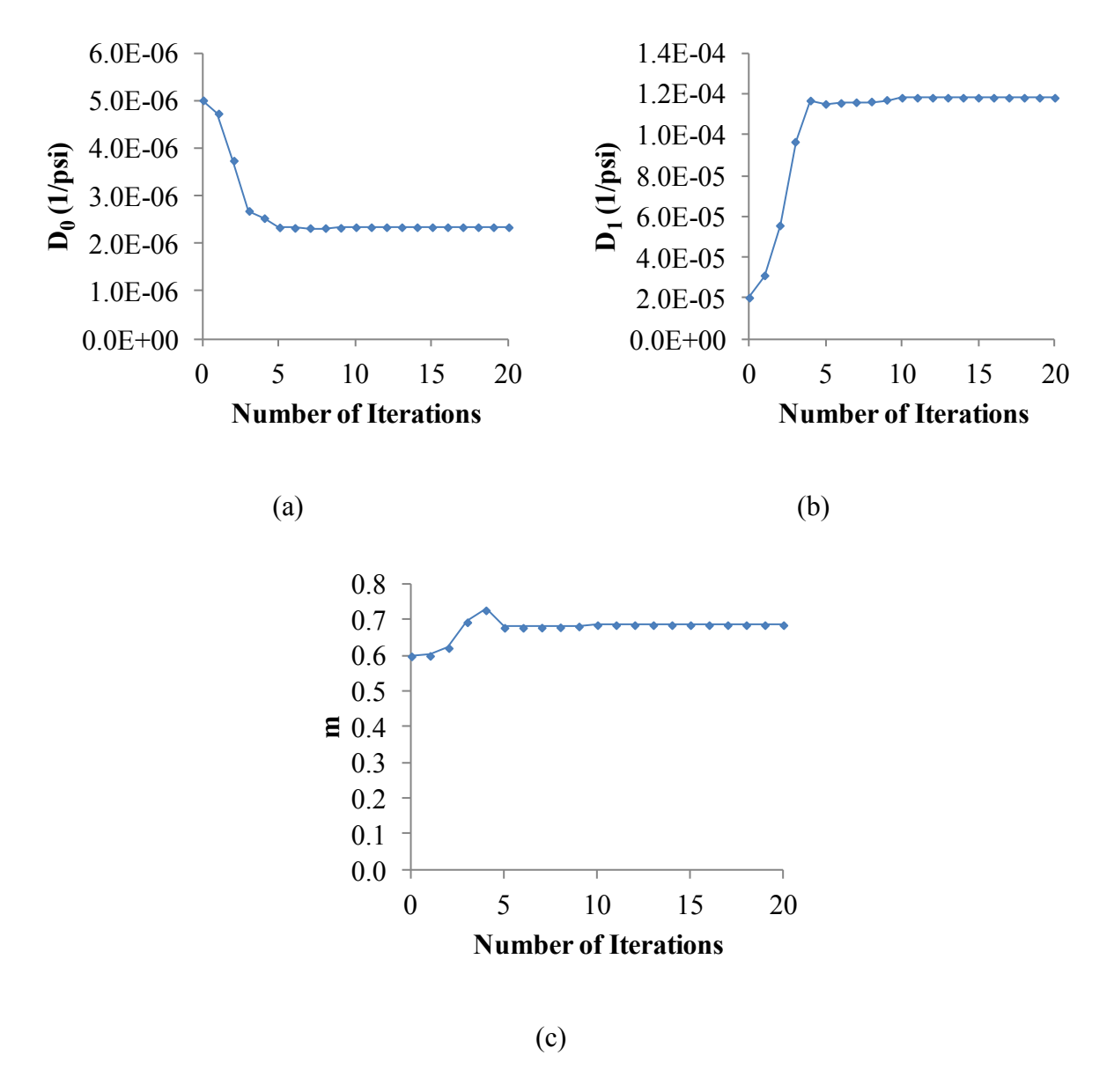


Figure 8-12 Convergence of Power Function Parameters (a) D_0 , (b) D_1 , and (c) m-5 Layer System

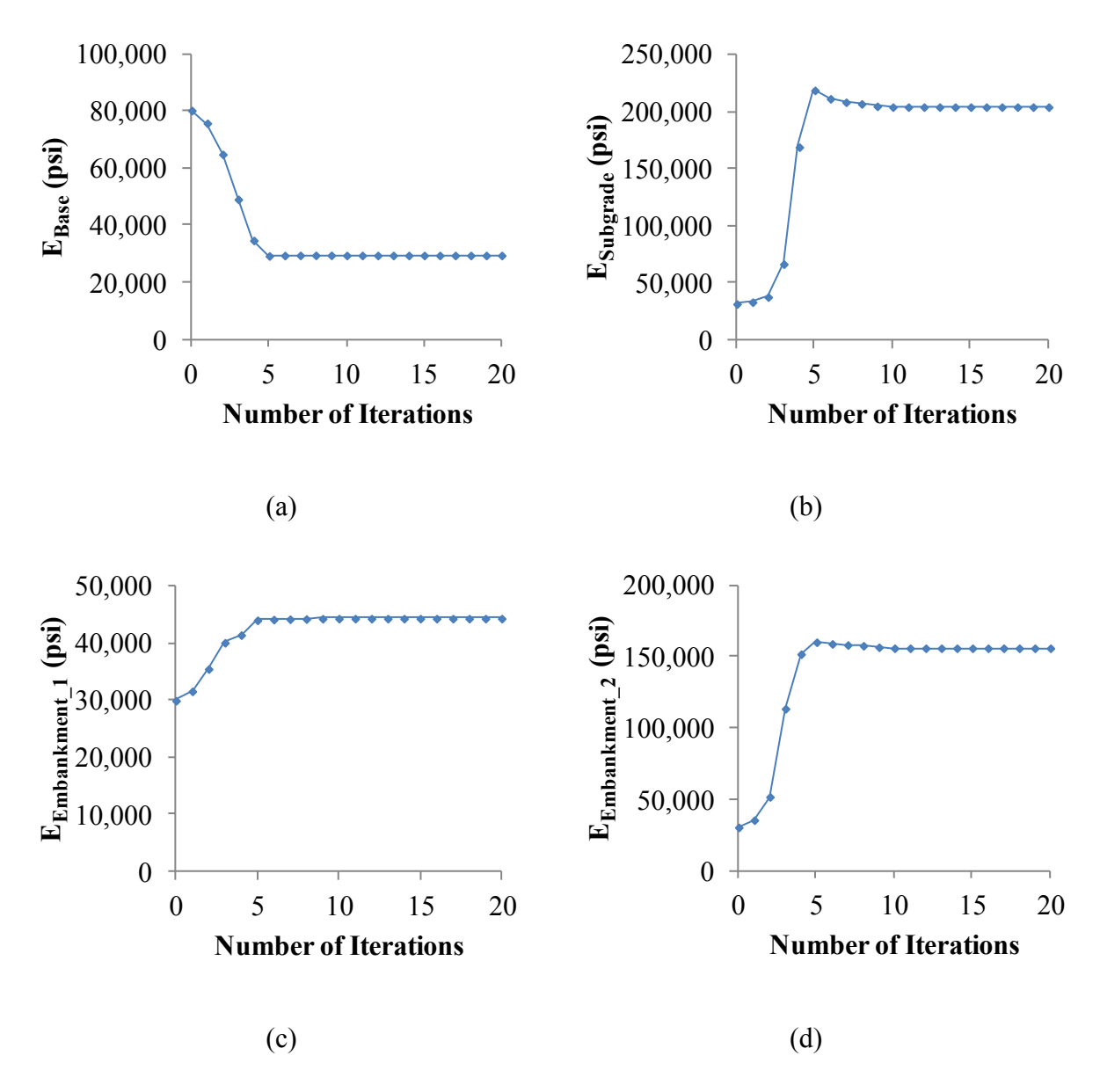


Figure 8-13 Convergence of Unbound Pavement Layer Moduli for the 3 Layer System (a) Base, (b) Subgrade, (c) Embankment 1, and (d) Embankment 2

Figure 8-14 shows the creep compliance functions plotted using the seed and the backcalculated parameters. It is noted that although the backcalculated creep compliance shows increased viscoelastic behaviour when compared to the seed creep compliance, the increased viscoelastic creep behaviour was slightly higher than the one backcalculated using the 3 layer system.

The backcalculated creep compliance was again converted to the dynamic modulus through the use of Prony series. The dynamic modulus mastercurves at 58°C and 10°C are shown in Figure 8-15. Although the mastercurve plotted for 58°C (Figure 8-15a) may seem fairly reasonable, the mastercurve at 10°C (Figure 8-15b) clearly shows that the backcalculated dynamic modulus underestimates the laboratory dynamic modulus.

Although the backcalculation with a 5 layer system resulted in a lower RMSE than the 3 layer system, the 3 layer backcalculation showed better agreement with the laboratory results for the asphalt modulus.

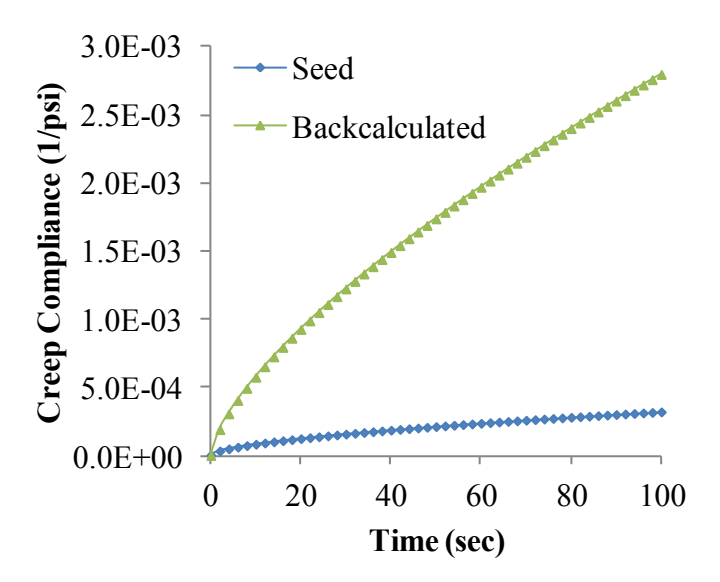


Figure 8-14 (a) Seed and (b) Backcalculated Creep Compliance Functions from 5 Layer System

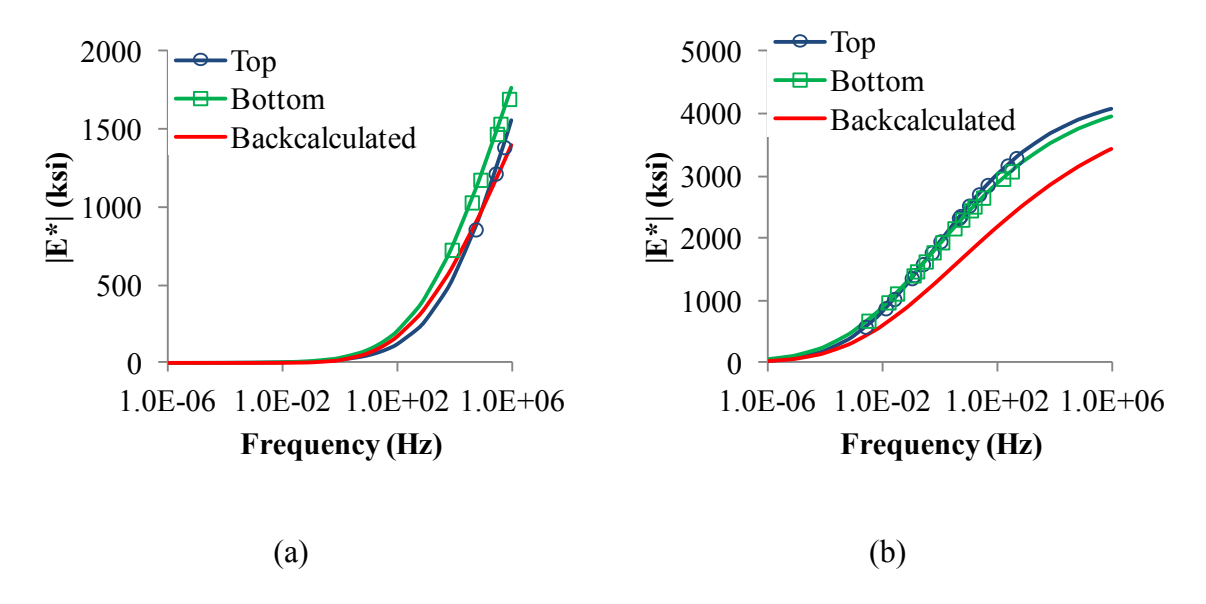


Figure 8-15 Backcalculated Dynamic Modulus Mastercurves at Reference Temperatures (a) 58°C and (b) 10°C – 5 Layer System

CHAPTER 9 - CONCLUSIONS AND RECOMMENDATIONS

Due to the viscoelastic nature of asphalt materials and the dynamic nature of pavement structures, it is important to consider both effects simultaneously in modeling of asphalt pavements. In this study, a new computational algorithm, namely ViscoWave, has been developed and implemented for modeling the pavement dynamics and viscoelasticity under an impact load generated by a Falling Weight Deflectometer (FWD). The primary advantage of the proposed solution over some of the existing solutions is that it uses continuous integral transforms (Laplace and Hankel transforms) that are more appropriate for the FWD time histories whose signal characteristics are transient, nonperiodic, and truncated.

The theoretical development of ViscoWave follows similar steps to those used for the development of the spectral element method but in place of the discrete transforms adopted in the spectral element method, ViscoWave utilizes the continuous integral transforms (namely Laplace and Hankel transforms) that are more appropriate for transient, nonperiodic signals. A comparison of the ViscoWave results with other existing solutions such as the Finite Element Analysis (FEA) and spectral element method indicated that ViscoWave is capable of simulating the viscoelastic and dynamic effects of asphalt pavements.

Preliminary backcalculation efforts were conducted by adopting the Gauss-Newton and the Levenberg-Marquardt methods as the optimization routines. Both the theoretical and field backcalculation indicate that the new solution (ViscoWave) has great potential for backcalculation, which has remained a major challenge in pavement engineering. Nonetheless, it

is recognized that the field data presented in this report only include the FWD data from a single temperature. Additional effort is needed to look into the FWD data collected at multiple temperatures.

It is also recommended that future work be conducted to improve the dynamic backcalculation using ViscoWave with different optimization routines that may show improved efficiency. It is also noted that the backcalculation routines used for this study fall into the category of unconfined optimization, meaning that the backcalculated variables were allowed to take on any value (even negative values). Future work should include looking into the use of confined optimization routines which may increase the efficiency and reliability of the backcalculation.

BIBLIOGRAPHY

BIBLIOGRAPHY

- 1. Abate, J., and Valko, P. P. 2004. Multi-Precision Laplace Transform Inversion. International Journal for Numerical Methods in Engineering. 60: 979-993.
- 2. Abramowitz, M., and Stegun, I. A. 1972. Handbook of Mathematical Functions with Formulas, Graphs, and Mathematical Tables. Dover Publications, Inc. NY.
- 3. Al-Khoury, R., Scarpas, A., Kasbergen, C., and Blaauwendraad, J. 2001a. Spectral Element Technique for Efficient Parameter Identification of Layered Media. I. Forward Calculation. International Journal of Solids and Structures. 38: 1605-1623.
- 4. Al-Khoury, Kasbergen, C., R., Scarpas, A., and Blaauwendraad, J. 2001b. Spectral Element Technique for Efficient Parameter Identification of Layered Media Part II. Inverse Calculation. International Journal of Solids and Structures. 38: 8753-8772.
- 5. Al-Khoury, R., Scarpas, A., Kasbergen, C., and Blaauwendraad, J. 2002. Spectral Element Technique for Efficient Parameter Identification of Layered Media Part III. Viscoelastic Aspects. International Journal of Solids and Structures. 39: 2189-2201.
- 6. ARA., ERES Division. 2004. Guide for Mechanistic-Empirical Design of New and Rehabilitated Pavement Structures. National Cooperative Highway Research Program1-37A, Transportation Research Board, National Research Council.
- 7. Bendat, J. S., and Piersol, A. G. 2010. Random Data Analysis and Measurement Procedures. 4th Ed. John Wiley & Sons, Inc., NJ.
- 8. Buttlar, W. G., and Roque, R. 1994. Development and evaluation of the strategic highway research program measurement and analysis system for indirect tensile testing at low temperatures. Transportation Research Record, 1454: 163-171.
- 9. Chatti, K., and Yun, K. K. 1996. SAPSI-M: Computer Program for Analyzing Asphalt Concrete Pavements Under Moving Arbitrary Loads. Transportation Research Record, 1539: 88-95.
- 10. Chatti, K., Ji, Y., and Harichandran, R. 2004. Dynamic Time Domain Backcalculation of Layer Moduli, Damping and Thicknesses in Flexible Pavements. Transportation Research Record, 1869: 106-116.
- 11. Christensen, R. M. 2003. Theory of Viscoelasticity. 2nd Ed. Dover Publications, Inc. NY.
- 12. Cook, R. D., Malkus, D. S., Plesha, M. E., and Witt, R. J. 2001. Concepts and Applications of Finite Element Analysis. 4th Ed. John Wiley & Sons, Inc. NY.
- 13. Cornille, P. 1972. Computation of Hankel Transforms. SIAM Review. 14(2): 278-285.

- 14. Ewing, W. M., Jardetzky, W. S., and Press, F. 1957. Elastic Waves in Layered Media. McGraw-Hill Book Company. NY.
- 15. Findley, W. N., Lai, J. S., and Onaran, K. 1976. Creep and Relaxation of Nonlinear Viscoelastic Materials. Dover Publications, Inc. NY.
- 16. Graff, K. 1991. Wave Motion in Elastic Solids. Dover Publications, Inc. NY.
- 17. Grenier, S., and Konrad, J. 2007. Backcalculation of Asphalt Concrete layer Thickness Using Static and Dynamic Interpretations of FWD Tests. Transportation Research Board Annual Meeting CD-ROM, 07-0573, Transportation Research Board, Washington D. C.
- 18. Hadidi, R., and Gucunski, N. 2007. A Probabilistic Approach to Falling Weight Deflectometer Backcalculation. Transportation Research Board Annual Meeting CD-ROM, 07-3187, Transportation Research Board, Washington D. C.
- 19. Hondros, G. 1959. The evaluation of Poisson's ratio and the modulus of materials of a low tensile resistance by the brazilian (indirect tensile) test with particular reference to concrete. Australian Journal of Applied Science, 10(3): 243-268.
- 20. Huang, Y. H. 2004. Pavement Analysis and Design, 2nd Ed. Pearson Education, Inc. NJ.
- 21. Irwin, L.H. 1977. Determination of pavement layer moduli from surface deflection data for pavement performance evaluation. Proc. Fourth Intl. Conf. on Structural Design of Asphalt Pavements. Ann Arbor, MI, University of Michigan, 831-840.
- 22. Ji, Y. 2005. Frequency and time domain backcalculation of flexible pavement layer parameters. Ph. D. Dissertation. Michigan State University.
- 23. Kang, Y. V. 1990. Effect of Finite Width on Dynamic Deflections of Pavement. Ph. D. Dissertation. University of Texas, Austin.
- 24. Kim, J., Roque, R., and Birgisson, B. 2005. Obtaining creep compliance parameters accurately from static or cyclic creep tests., ASTM International, ASTM STP 1469: 177-197.
- 25. Kim, J., Sholar, G., and Kim, S. 2008. 'Determination of accurate creep compliance and relaxation modulus at a single temperature for viscoelastic solids. Journal of Materials in Civil Engineering, ASCE, 20(2): 147-156.
- 26. Kim, J., Lee, H. S., and Kim, N. 2010. Determination of Shear and Bulk Moduli of Viscoelastic Solids from the Indirect Tension Creep Test. Journal of Engineering Mehcanics. ASCE. 136:1067-1076.
- 27. Kim, J. 2011. General Viscoelastic Solutions for the Multilayered Systems Subjected to Static and Moving Loads. Journal of Materials in Civil Engineering. ASCE. 23:1007-1016.

- 28. Kim, Y. R. 2009. Modeling of Asphalt Concrete. ASCE Press. McGraw Hill.
- 29. Kutay, E., Chatti, K., and Lei, L. 2011. Backcalculation of Dynamic Modulus (|E*|) Mastercurve from FWD Surface Deflections. Transportation Research Board Annual Meeting DVD, 11-3434, Transportation Research Board, Washington D. C.
- 30. Lee, H. S., and Kim, J. 2009, Determination of viscoelastic Poisson's ratio and creep compliance from the indirect tension test. Journal of Materials in Civil Engineering ASCE, 21(8): 416-425.
- 31. Lee, H. S. 2011, ViscoWave A New Forward Solution for Dynamic Backcalculation. A Presentation Made at the 20th Annual FWD Users Group Meeting. http://pms.nevadadot.com/2011.asp. Last Accessed January 2012.
- 32. Lee, H. S. 2013. Viscowave A New Solution for Viscoelastic Wave Propagation of Layered Structures Subjected to an Impact Load, International Journal of Pavement Engineering, DOI:10.1080/10298436.2013.782401.
- 33. Losa, M. 2002. The Influence of Asphalt Pavement Layer Properties on Vibration Transmission. International Journal of Pavements. 1(1): 67-76.
- 34. Magnuson, A. H., Lytton, R. L., and Briggs, R. 1991. Comparison of Computer Predictions and Field Data for Dynamic Analysis of Falling-Weight Deflectometer Data. Transportation Research Record, 1293: 61-71.
- 35. Malvern, L. E. 1969. Introduction to the Mechanics of a Continous Medium. Prentice-Hall, Inc. NJ.
- 36. Mathworks. 2008. Matlab Optimization Toolbox User's Guide. The Mathworks Inc., MA.
- 37. Matsui, K., Maina, J. W., Hachiya, Y., and Ozawa, Y. 2011. Wave Propagation Analysis for Flexible Pavements and Its Application to Backcalculation Analysis. Transportation Research Board Annual Meeting DVD, 11-2971, Transportation Research Board, Washington D. C.
- 38. Matsui, K., Nishizawa, T., and Kikuta, Y. 1998. Time Domain Backcalculation of Pavements. Structural Materials Technology III: An NDT Conference. Medlock, R. D., and Laffrey, D. C. Ed. San Antonio, TX, 3400: 410-419.
- 39. Ong, C. L., Newcomb, D. E., and Siddharthan, R. 1991. Comparison of Dynamic and Static Backcalculation Moduli for Three-Layer Pavements. Transportation Research Record, 1293: 86-92.
- 40. Rao, S. S. 1996. Engineering Optimization: Theory and Practice. 3rd Ed. John Wiley & Sons, Inc. NY.

- 41. Rizzi, S. 1989. A Spectral Analysis Approach to Wave Propagation in Layered Solids. Ph. D. Dissertation. Purdue University
- 42. Roque, R., Buttlar, W. G., Ruth, B. E., Tia, M., Dickison, S. W., and Reid, B. 1997. Evaluation of SHRP indirect tension tester to mitigate cracking in asphalt concrete pavements and overlays. Final Report, FDOT B-9885, University of Florida, Gainesville, FL.
- 43. Roque, R., Buttlar, W. G., Ruth, B. E., and Dickison, S. W. 1998. Short-Loading-Time Stiffness from Creep, Resilient Modulus, and Strength Tests Using Superpave Indirect Tension Test. Transportation Research Record, 1630: 10-20.
- 44. Santamarina, J. C., and Fratta, D. 1998. Introduction to Discrete Signals and Inverse Problems in Civil Engineering. ASCE Press. VA.
- 45. Scales, L. E. 1985. Introduction to Non-Linear Optimization. Springer-Verlag, Inc. NY.
- 46. Schapery, R. A. 1974. Viscoelastic Behavior and Analysis of Composite Materials, in Mechanics of Composite Materials. Sendeckyj, G. P. Ed. Academic Press. NY.
- 47. Sneddon, I. N. 1995. Fourier Transforms. Dover Publications, Inc. NY.
- 48. Tschoegl, N. W., Knauss, W. G., and Emri, I. 2002. Poisson's ratio in viscoelasticity: a critical review. Mechanics of Time-Dependent Materials, 6: 3-51.
- 49. Tschoegl, N. W. 1989. The Phenomenological Theory of Linear Viscoelastic Behavior: An Introduction. Springer-Verlag, NY.
- 50. Uzan, J. 1994. Dynamic Linear Backcalculation of Pavement Material Parameters. Journal of Transportation Engineering ASCE, 120(1): 109-126.
- 51. Uzan, J., Scullion, T., Parades, M., and Lytton, R. L. 1988. A Microcomputer Based Procedure for Backcalculating Layer Moduli from FWD Data. Research Report 1123-1, Texas Transportation Institute.
- 52. Venkataraman, P. 2002. Applied Optimization with MATLAB Programming. John Wiley & Sons, Inc. NY.
- 53. Wineman, A. S., and Rajagopal, K. R. 2000. Mechanical response of polymers: an introduction. Cambridge University Press, NY.
- 54. Zhang, W., Drescher, A., and Newcomb, D. E. 1997a. Viscoelastic analysis of diametral compression of asphalt concrete. Journal of Engineering Mechanics, ASCE, 123(6), 596-603.
- 55. Zhang, W., Drescher, A., and Newcomb, D. E. 1997b. Viscoelastic behavior of asphalt concrete in diametral compression. Journal of Transportation Engineering, ASCE, 123(6), 495-502.